

**SURFACE VELOCITIES OF THE EAST ANTARCTIC ICE
STREAMS FROM RADARSAT-1 INTERFEROMETRIC
SYNTHETIC APERTURE RADAR DATA**

DISSERTATION

Presented in Partial Fulfillment of the Requirements for
the Degree Doctor of Philosophy in the Graduate
School of The Ohio State University

By

Zhiyuan Zhao, B.S., M.S.

The Ohio State University

2001

Dissertation Committee:

Professor Alan Saalfeld, Adviser

Professor Kenneth C. Jezek

Professor Carolyn J. Merry

Approved by

Adviser

Geodetic Science Graduate Program



This photo was taken on February 28, 2001 after Zhiyuan Zhao's Ph.D. defense. From left to right: Professor Kenneth C. Jezek, Professor Carolyn J. Merry, Professor Alan Saalfeld, Zhiyuan Zhao, Professor Avraham Benatar (graduate school representative).

ABSTRACT

The newly discovered East Antarctic Ice Streams drain a significant portion of the Antarctic Ice Sheet. Therefore, changes in their flow behavior can significantly alter ice-sheet mass-balance and influence global sea level. This dissertation research created the most comprehensive measurements to date of surface velocity across the East Antarctic Ice Streams using RADARSAT-1 interferometric synthetic aperture radar (InSAR) data acquired in 1997. Two-dimensional surface velocity was derived by combined interferometric and speckle matching techniques. Improvements in both techniques mediated some of the unique problems and limitations associated with imaging the Antarctic Ice Sheet using RADARSAT-1. The improvements included Delaunay triangulation based co-registration of SAR images, phase reconciliation of disconnected phase patches, and two-dimensional velocity calibration using extended velocity control points. The research produced a highly dense, highly accurate, two-dimensional surface velocity map of the East Antarctic Ice Streams, and a by-product coherence map reflecting surface changes. The velocity uncertainty is better than 15 m/year and velocity direction error is within 5° on the ice shelf and ice streams. Ice-stream shear-margins were mapped based on the SAR mosaic, velocity map and coherence map. Comparison between ice stream margins and BEDMAP subglacial topography suggests that ice stream flow is controlled by bedrock topography. Mass balance calculations indicate that

the ice stream and Filchner Ice Shelf system is not significantly thinning or thickening. There is evidence to suggest that at least one of the individual ice streams (Bailey Glacier) is thickening at a rate of 0.25 ± 0.06 m per year. Ice stream surfaces are generally convex and Slessor Glacier and Bailey Ice Stream driving stresses are large compared to the concave shaped West Antarctic Ice Streams. The surface topography of Recovery Glacier varies the most from an equilibrium profile and stretches of the Recovery Glacier have low driving stress, suggestive of flow on a lubricated bed. The convexity of the surface profiles, high driving stress, evidence of streaming flow and the shape of the glacier bed suggest that a change in ice stream dynamics could potentially result in an imbalanced discharge of large amounts of ice into the sea.

Dedicated to my parents

献给我亲爱的父母

ACKNOWLEDGMENTS

First of all, I wish to express my sincere gratitude Dr. Alan Saalfeld and Dr. Kenneth C. Jezek for their unfailing advice and valuable instructions at all points along the way of my Ph.D study. Their expertise, insights and enlightening lectures have strongly influenced my research direction and stimulated my interests in GIS, satellite remote sensing and glaciology in general and synthetic aperture radar in particular. During the preparation of the dissertation, their critical and thoughtful comments and suggestions gave me great help in clarifying the concepts, sharpening the thinking, and broadening the vision, and also making the dissertation research more challenging and fruitful.

Special thanks also go to Dr. Carolyn Merry. While serving on my dissertation committee, she carefully reviewed my research proposal and the draft manuscript, and offered many constructive comments and suggestions. In addition, I benefited enormously from taking her remote sensing class, which gave me a solid education in and quick grasp of the principles, theories and techniques of remote sensing.

Similar gratitude should be extended to Dr. Laurence Gray for providing me with speckle matching codes and tidal data, to Rock Forster and Xiaoqing Wu for helpful discussions on the InSAR technique and glaciology, to my colleagues for making the

Remote Sensing Laboratory a friendly and interesting place to spend my years, and to Dr. Yong Lang for his critical reading of the first draft of this dissertation.

Finally, I want to record my deep gratitude to my wife, Ming Sun, for her emotional encouragement and support, and to my parents for whom I could not fail and to whom this dissertation is dedicated.

VITA

October 12, 1962... ..Born – Shandong, China

1983.....B.S. Mathematics, East China Normal University

1987..... M.S. Surveying Engineering
Shandong Institute of Mining and Technology

1997..... M.S. Geodetic Science
The Ohio State University

1983-1985..... Teaching Assistant
Shandong Institute of Mining and Technology

1987-1994.....Lecturer
Shandong Institute of Mining and Technology

1994-1995.....Research Associate, German National Research
Center for Information Technology

1995-2001.....Graduate Research Associate
The Ohio State University

PUBLICATIONS

1. Zhao, Z., K. Jezek, L. Gray, N. Short, R. Forster, 2000. East Antarctic Ice Streams, EOS, Transactions, AGU, 2000 Fall Meeting, Vol. 81, No. 48, p 438.
2. Jezek, K., H. Liu, Z. Zhao, B. Li, 1999, Improving digital elevation model of Antarctica using radar remote sensing data and GIS techniques, Polar Geography, 1999,23, No.3, pp. 185-200
3. Zhao, Zhiyuan, Alan Saalfeld, 1998, Morphology-Based Line Generalization for Raster and Vector Data. GIS/LIS '98 Proceedings. Bethesda: ASPRS.
4. Zhao, Zhiyuan, Alan Saalfeld, Sleeve-Fitting Polyline Simplification Algorithms, Proceedings of Auto-Carto 13, ACSM, 1997, pp 214-223
5. Zhao, Zhiyuan, Alan Saalfeld, Raul Ramirez, 1996, A General Line-Following Algorithm for Raster Maps. GIS/LIS '96 Proceedings. Bethesda: ASPRS, pp 85-93.
6. Zhou, J., Z. Zhao, An Algorithm on Integer Decomposition, Proceedings of the Fourth International Conference for Young Computer Scientists, Peking University Press, July 1995, pp. 674-675
7. Zhou, J., Zhao, S. Liu, A Chinese Character Coding Method, Journal of Chinese Information Processing, January 1995.
8. Zhou, J., Z. Zhao, Theory and Algorithms for Fast Sorting and Searching, Science Press, Beijing, June 1993, First Edition (book in Chinese)
9. Zhou, J., Z. Zhao, Bucketing Algorithm Combined with Probability Distribution of Data, Journal of Qufu Normal University, Vol.18,No.1, 1992, pp 26-28

10. Zhao, Z., M. Zhang, Raster-Vector Conversion of Chinese Characters, Journal of Chinese Information Processing, Vol. 4, No. 4, 1991, pp 59-65
11. Zhou, J., Z. Zhao, Random Block Search Algorithm, Chinese Science Bulletin, Vol. 36, No.19, 1991, pp 1905-1906
12. Zhao, Z., Decorative Chinese Characters Processing, Microcomputer Application, Vol. 12, No.3, 1991, pp 51-54
13. Zhao, Z., Research on Pocket Computer Chinese Processing System, 3rd National Conference on Pocket Computer, Chinese Science Press, Beijing, 1991, pp 150-153
14. Zhou, J., Z. Zhao, Quad-Cutting Method for Polygon Window, PC World, 10 (1990), pp 75-76
15. Zhao, Z. Smoothing of Chinese Characters, Journal of Shandong Institute of Mining and Technology, Vol.8, No.2, 6(1989), pp 75-78

FIELDS OF STUDY

Major Field: Geodetic Science

TABLE OF CONTENTS

	<u>Page</u>
Abstract	ii
Dedication	iv
Acknowledgments	v
Vita	vii
List of Tables	xiv
List of Figures.....	xv
Chapters	
1. Introduction	1
1.1 Background.....	1
1.2 Research copes and objectives.....	3
1.3 Summary of chapters.....	4
2. Interferometry Technique.....	6
2.1 Introduction.....	6
2.2 Basic principle of SAR interferometry.....	7
2.2.1 Geometry	7
2.2.2 Phase measurement	11
2.2.3 Phase separation	13

2.3 SAR interferometry processing.....	15
2.3.1 Processing overview.....	15
2.3.2 SLC image co-registration	15
2.3.3 Calculate interferogram	19
2.3.4 Phase reconciliation.	20
2.3.5 Baseline refinement.	21
2.3.6 Data geocoding	22
2.4 SAR interferometry applications.....	25
2.4.1 Elevation estimation	25
2.4.2 Surface motion estimation	27
2.4.3 Double difference interferometry	29
3. Speckle matching technique.....	32
3.1 Introduction.....	32
3.2 Review of matching methods.....	33
3.2.1 Cross-correlation	33
3.2.2 Sub-pixel accuracy calculation.....	35
3.2.3 Accuracy and complexity of matching	37
3.3 Velocity calibration.....	40
3.4 Velocity errors.....	44
3.5 Comparison with interferometry technique.....	45
4. Improving Interferometric SAR Coherence by Delaunay Triangulation based co-registration.....	47
4.1 Introduction.....	47

4.2	Co-registration decorrelation of interferometric SAR.....	49
4.3	Delaunay triangulation based co-registration.....	58
4.4	Example and Application.....	63
5.	Phase unwrapping and phase reconciliation.....	75
5.1	Introduction.....	75
5.2	Phase unwrapping.....	78
5.3	Phase reconciliation.....	80
5.4	Error analysis.....	84
5.5	Example.....	85
5.6	Implementation.....	92
6.	Two-dimensional surface velocities of the East Antarctic Ice Streams.....	93
6.1	Introduction.....	93
6.2	Two-dimensional surface velocity.....	94
6.2.1	Velocity control points and velocity calibration.....	94
6.2.2	Baseline refinement.....	100
6.2.3	Strip calibration.....	103
6.2.4	Examples.....	108
6.3	Velocity mosaic of the East Antarctic Ice Streams.....	115
6.3.1	Data.....	115
6.3.2	Data processing.....	117
6.3.3	Velocity mosaic.....	123
6.4	Error analysis and quality assessment.....	125
6.4.1	Error analysis.....	125

6.4.2 Quality assessment.....	127
7. The East Antarctic Ice Streams.....	138
7.1 Introduction.....	138
7.2 Ice flow dynamics of the East Antarctic Ice Streams.....	139
7.2.1 Ice stream margins.....	139
7.2.2 Ice flow patterns.....	146
7.2.3 Grounding lines and ice rise.....	155
7.2.4 RAMP glacier and Blackwall ice stream.....	160
7.3 Mass balance and mass distribution of East Antarctic Ice Streams.....	163
7.3.1 Data sets.....	163
7.3.2 Mass balance calculation	163
7.3.3 Mass distribution.....	167
8. Conclusion.....	171
References.....	175

LIST OF TABLES

<u>Table</u>	<u>Page</u>
2.1 Doppler centroids and their difference for InSAR orbits 9822/10165.....	18
3.1 Comparison between interferometry and speckle matching techniques.....	45
5.1 Statistics of phase reconciliation for frame 5556 of orbit 9822/10165.....	87
6.1 Velocity product requirements.....	95
6.2 Calibration parameters from different type of velocity control points.....	109
6.3 Refined baseline and baseline from satellite orbits.....	109
6.4 Calibration parameters from frame calibration and from strip calibration.....	110
6.5 Descriptions of InSAR data of the East Antarctic Ice Streams.....	116
6.6 Velocities on the Filchner Ice Shelf from different sources.....	130
6.7 Velocities from Vaughan and this research.....	131
7.1 Comparison between the RAMP Glacier and the Blackwall Ice Stream.....	160
7.2 Gate flux of the 12 gates.....	166
7.3 Thickening rate of the East Antarctic Ice Streams.....	166

LIST OF FIGURES

<u>Figure</u>	<u>Page</u>
2.1 Geometry of cross-track interferometric SAR.....	9
3.1 Cross-correlation matching.....	33
3.2 Maximum correlation and its 8 neighbors.....	35
3.3 Geometry configuration of InSAR pair under parallel ray assumption.....	41
4.1 Theoretical registration decorrelation coefficient curves.....	53
4.2 Swap test of empty circumcircle property.....	59
4.3 Interpolation inside a triangle.....	61
4.4 Location of example data.....	63
4.5 Comparison of coherence images of the two registration methods.....	66
4.6 Comparison of interferogram chips.....	69
4.7 Comparison of histograms of coherence images in Figure 4.5.....	71
4.8 Coherence mosaic of the East Antarctic Ice Streams.....	74
5.1 InSAR frame 5556 of orbit 9822/10165.....	77
5.2 Relationship between range difference and pixel offset.....	81
5.3 Wrapped phase after removal of baseline and topography.....	89
5.4 Unwrapped phase of five regions A-E using five reference points marked in Figure 5.3 and the merged phase	90
5.5 Phase profiles along a constant azimuth line before phase	

reconciliation (a) and after phase reconciliation (b).....	91
6.1 Flow direction control point.....	98
6.2 Frame configuration of strip calibration.....	105
6.3 Flow direction control points are selected in velocity calibration.....	112
6.4 Velocity vectors after calibration using flow directions shown in Figure 6.3...	113
6.5 Enlarged view of the left bottom corner of the Figure 6.4.....	114
6.6 Locations of RADARSAT InSAR data of the East Antarctic Ice Streams.....	118
6.7 Diagram of processing for two-dimension surface velocity estimation.....	119
6.8 Surface velocity mosaic of the East Antarctic Ice Streams.....	124
6.9 Velocity angle error distribution.....	132
6.10 Velocity vectors on slant range SAR image.....	133
6.11 Velocity vectors on upstream of Slessor Glacier.....	134
6.12 Velocity vectors before tidal correction (a) and after tidal correction (b).....	135
6.13 Velocity point locations on the Filchner Ice Shelf.....	136
6.14 Comparison of velocities on the Filchner Ice Shelf.....	137
7.1 Shear margins of the East Antarctic Ice Streams.....	143
7.2 Shear margins in SAR image and coherence.....	144
7.3 Ice stream margins and BEDMAP subglacial topography	145
7.4 Contours of the surface velocity of the East Antarctic Ice Streams.....	149
7.5 Locations of longitudinal and cross profile of the recovery glacier.....	150
7.6 Profiles of surface and bedrock elevation and surface velocity for Bailer, Slessor, and Recovery glaciers.....	151
7.7 Profiles of surface and bed rock elevation and velocity	

for cross profiles D, E, and F.....	152
7.8 Surface elevation reconstruction (a) and comparison between basal and driving stress.....	153
7.9 Comparison of surface and bed rock elevation and driving stress between WAIS and EAIS.....	154
7.10 Comparison of grounding lines from interferometry and from ADD database.....	157
7.11 Ice rise in the SAR image and coherence image.....	158
7.12 Fringes of the ice rise.....	159
7.13 Longitudinal profiles of RAMP and Blackwall Ice Stream.....	162
7.14 Locations of regions and gates for mass balance calculation and Thickening rate of the East Antarctic Ice Streams	169
7.15 Mass distribution of the East Antarctic Ice Streams.....	170

CHAPTER 1

INTRODUCTION

1.1 Background

The Antarctic Ice Sheet contains about 77% of the total fresh-water resources on the earth. It plays a very important role in global climate by modulating surface energy budgets, controlling atmospheric circulation and serving as a reservoir of vast amounts of water (Hughes, 1975; Mercer, 1978; Bindshadler, 1991; Rott and others, 1996). The latter is particularly important because changes in the reservoir are directly related to sea level change. If the Antarctic Ice Sheet melts completely, global sea level will rise some 68 m (IPCC, 1996). The East Antarctic Ice Streams, along with the West Antarctic Ice Streams and the Lambert Glacier, drain a significant portion of the Antarctic Ice Sheet (Drewry and others, 1982). Therefore, changes in their flow behavior can significantly alter the ice sheet's mass balance. In 1997, the Radarsat Antarctic Mapping Project (RAMP) produced the first ever continental-scale, high-resolution snapshot of the Antarctic Ice Streams (Jezek and others, 1998). The 30-day mission also generated interferometric data over portions of the continent, including the East Antarctic Ice Streams. These interferometric data provide an unparalleled opportunity to study the dynamics of the East Antarctic Ice Streams.

Synthetic Aperture Radar Interferometry (InSAR) is a well-demonstrated technique for measuring ice sheet surface velocity. It can provide a broad-scale, dense spatial coverage with excellent accuracy. Starting with the pioneering work of Goldstein and others (1993), several investigators have shown the utility of radar interferometry-derived velocities in glacier mass balance and dynamical studies (Joughin and others, 1996; Kwok and Fahnestock, 1996; Rignot and others, 1995; Forster and others, 1999). However, the differential InSAR technique only produces one component of surface motion in the radar look direction, and fails in fast moving glacier regions due to the low coherence. As a complement to the InSAR technique, a speckle matching technique (Gray and others, 1998) can produce two components of motion even for fast moving glaciers, but the measurement accuracy is limited by the size of the resolution cell.

There are unresolved complications in applying the InSAR technique to Antarctica. First, temporal decorrelation and co-registration decorrelation limit the use of phase information for range motion calculations. In this research, the coherence is improved by a new co-registration technique that can handle the large and irregular geometric distortion of the ice sheet between SAR observations due to surface motion. Also regions of unwrapped fringes separated by temporally decorrelated channels are merged into one large region with the same reference using the range offset from speckle matching. Second, velocity estimation requires ground control points with known velocity. In the East Antarctic, it is impossible to satisfy its requirements for every frame of InSAR data. In this research, in addition to traditional velocity control points, we explored flow directions as supplement to velocity control points.

1.2 Research Scope and Objectives

The three objectives of this dissertation research are: (1) to explore technical methods and algorithms that are suitable for two-dimensional surface-velocity estimation from RADARSAT interferometry data over the East Antarctic Ice Streams; (2) to process the data and produce the first ever surface velocity and coherence maps for the East Antarctic Ice Streams; and (3) to study East Antarctic Ice Streams ice dynamic and mass balance based on the surface velocity map, coherence map, as well as other existing data of the region. The first objective requires examining the interferometry and speckle matching techniques that are already used in ice motion estimation, and examining the limitations of those techniques for processing RADARSAT InSAR data over the East Antarctic Ice Streams. These limitations are partially due to the long repeat cycle of RADARSAT (24 days) and the fast movement of the East Antarctic Ice Streams. New methods and algorithms are explored that can overcome these limitations and produce two-dimensional surface velocity maps using RADARSAT InSAR data of the East Antarctic Ice Streams. Methods for co-registration, phase reconciliation, and velocity calibration will be developed. The second objective focuses more on data processing to produce velocity and coherence maps. The third objective targets the scientific analysis of the East Antarctic Ice Stream dynamics. The flow pattern of the East Antarctic Ice Streams is identified. The ice dynamics is investigated by comparing longitudinal and transect profiles of various glaciers and by comparing ice flow with subglacier topography. The mass distribution and mass balance of East Antarctic Ice Streams is calculated. In particular we answer the question: are the East Antarctic Ice Streams a potential mechanism for rapidly draining large amounts of ice from the interior ice sheet?

1.3 Summary of Chapters

Chapter 1 presents background materials, research scope and objectives.

Chapter 2 reviews the principle of the SAR interferometry technique. Interferometric processing and applications with emphasis on surface motion estimation are then discussed. Problems and limitations of the interferometry technique are identified for applications to the East Antarctic Ice Streams.

Chapter 3 describes the Speckle Matching technique that can generate surface motion in two dimensions. Matching methods, velocity calibration, and error analysis are discussed. A comparison is also made between interferometry and speckle matching techniques.

Chapter 4 focuses on co-registration decorrelation due to the long temporal baseline and fast moving glaciers. This chapter provides a theoretical analysis of co-registration decorrelation, then introduces the Delaunay-triangulation-based co-registration method. The technique is used to create a better coherence map of the East Antarctic Ice Streams and more accurate phase estimation.

Chapter 5 deals with phase unwrapping and establishing a reference phase for coherent sectors of image frames devoid of velocity control points. The well-established phase unwrapping algorithms are first reviewed. Then a phase reconciliation method is introduced that can align all independently unwrapped pieces (patches) to a uniform reference with the help of a range offset map from speckle matching. The error analysis and examples are presented in the chapter.

Chapter 6 explores methods to generate two-dimensional surface velocity by combining interferometry and speckle matching techniques. Extended velocity control points for velocity calibration are discussed. Models are developed for velocity registration and baseline refinement using the extended velocity control point types. Processing tools and processing procedures for producing a surface velocity map of the East Antarctic Ice Streams are described. Accuracy and quality assessment of the velocity map are also discussed.

Chapter 7 presents the scientific analysis of the East Antarctic Ice Streams. Based on the surface velocity map, the coherence map, and the SAR intensity map, the boundaries of the East Antarctic Ice Streams are identified. The margin map is compared with BEDMAP subglacial topography to understand the influence of subglacial topography on ice flow. Longitudinal profiles for the Bailey, Slessor, and Recovery glaciers are analyzed and compared. Recovery Glacier's twin RAMP Glacier and Blackwall Ice Stream are compared. Finally, the mass distribution and mass balance of the East Antarctic Ice Streams are calculated and analyzed.

Chapter 8 summarizes the research findings and draws conclusions from the research.

CHAPTER 2

INTERFEROMETRY TECHNIQUE

2.1 Introduction

The first interferometric measurement of earth surface elevation was made by Graham (1974) using airborne SAR. He estimated the surface elevation by coherent addition of two SAR images acquired by two antennas mounted one above the other on single-looking movable gimbals. Zebker and Goldstein (1986) first used the correlated phase of two complex images acquired by two separated antennas to generate surface topography. Since the launch of the European satellite ERS-1 in the early 1990s, more spaceborne and repeat orbit interferometric SAR data have been available, and the interferometric techniques and applications have been well developed. In addition to topography generation, Gabriel and others (1989) demonstrated that the interferometric technique could be used to detect surface motion in the range direction with known topography. Double difference interferometry, a generalized interferometric technique (Joughin and others, 1996b; Kwok and others, 1996; Fatland, 1998) can be used to separate topography and surface motion for ice streams where both topography and surface motion have an effect on the phase difference.

This chapter presents a brief review of the well-developed interferometric technique, which serves as the basis for the present research. First, the basic theory of the interferometric technique is reviewed. Then the processing methods of the technique are described. Last, the applications of the technique with emphasis on surface motion estimation are discussed. Concepts, notation, and equations established in this chapter will be used in later chapters.

2.2 Basic principle of SAR interferometry

2.2.1 Geometry

SAR interferometry is performed by imaging radar, an active illumination system. In the system, a radar signal is transmitted in a side look direction to the ground from an antenna on an aircraft or spacecraft, then scattered back and received by the antenna. The receiver records the amplitude A of the returned signal, as well as the phase shift ϕ . When two spatially-separated antennas view the same ground surface or the same antenna repeatedly views the same ground surface, two SAR images are acquired. The correlated phase difference reflects the combined effect of SAR geometry, surface elevation and surface motion.

The simple InSAR geometry is illustrated in Figure 2.1 in which the notations are the same as used in Joughin (1995). Assume that the earth model is flat, and point P does not move during the two observations. In the figure, S_1 and S_2 are two separate antennas, or a single antenna viewing the surface on two separate passes. The ground point P has elevation z . Ground distance to the satellite nadir in the range direction is y . The first observation has height H , and look angle θ , with range distance from the first antenna to

the surface point P being r_0 . The two antennas have baseline B and tilt angle ξ with respect to the horizontal. The range distance from the second satellite to the ground P is $r_0 + \Delta$. From the geometry, the ground position of P can be written as

$$y = r_0 \sin \mathbf{q} \quad (2.1)$$

$$z = H - r_0 \cos \mathbf{q} \quad (2.2)$$

Applying the law of cosines to triangle S_1S_2P , yields

$$\begin{aligned} (r_0 + \Delta)^2 &= r_0^2 + B^2 - 2r_0B \cos\left(\frac{\mathbf{p}}{2} - \mathbf{q} + \mathbf{x}\right) \\ &= r_0^2 + B^2 - 2r_0B \sin(\mathbf{q} - \mathbf{x}) \end{aligned} \quad (2.3)$$

Then we have

$$\sin(\mathbf{q} - \mathbf{x}) = \frac{r_0^2 + B^2 - (r_0 + \Delta)^2}{2r_0B} \quad (2.4)$$

Combining (2.1), (2.2) and (2.4), y and z are calculated as

$$\begin{aligned} z &= H - r_0 \cos(\mathbf{q} - \mathbf{x} + \mathbf{x}) \\ &= H - r_0 [\cos(\mathbf{q} - \mathbf{x}) \cos \mathbf{x} - \sin(\mathbf{q} - \mathbf{x}) \sin \mathbf{x}] \\ &= H - r_0 [\cos \mathbf{x} \sqrt{1 - \sin^2(\mathbf{q} - \mathbf{x})} - \sin(\mathbf{q} - \mathbf{x}) \sin \mathbf{x}] \end{aligned} \quad (2.5)$$

and

$$\begin{aligned} y &= r_0 \sin(\mathbf{q} - \mathbf{x} + \mathbf{x}) \\ &= r_0 [\sin(\mathbf{q} - \mathbf{x}) \cos \mathbf{x} + \cos(\mathbf{q} - \mathbf{x}) \sin \mathbf{x}] \\ &= r_0 [\sin(\mathbf{q} - \mathbf{x}) \cos \mathbf{x} + \sin \mathbf{x} \sqrt{1 - \sin^2(\mathbf{q} - \mathbf{x})}] \end{aligned} \quad (2.6)$$

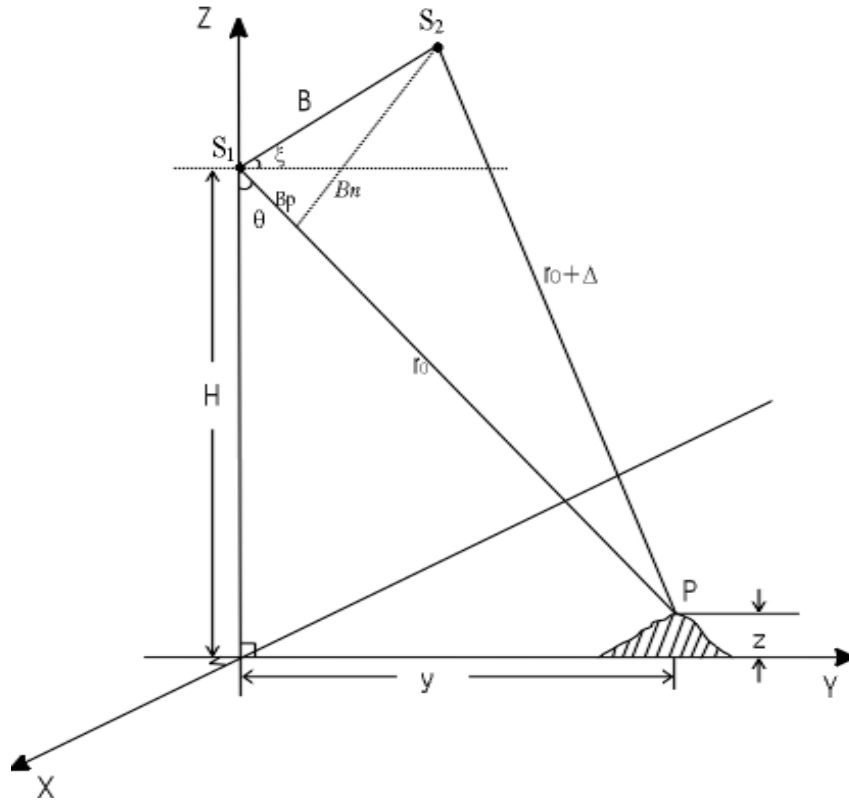


Fig. 2.1: Geometry of cross-track interferometric SAR. The SAR sensor is flying parallel to the X-axis (azimuth direction). The baseline B is determined by the sensor orbital positions S_1 and S_2 of two repeat passes. The baseline orientation is defined by the angle between the baseline and a horizontal line.

The above equations estimate the earth surface elevation z and ground range position y using the satellite parameters: satellite height (H), look angle (θ), baseline (B) and baseline angle (ξ), as well as measured range r_0 and $r_0 + \Delta$ from the first and second satellite positions to the ground point P , respectively. These parameters are known. So the ground positions y and z can be solved to the accuracy of these observations.

The range difference Δ is the difference of the two sides S_2P and S_1P in the triangle S_1S_2P . From the geometry, changing the elevation will change the shape of the triangle. Changing the baseline distance and/or the baseline angle will also change the triangle. So the baseline and the topography will affect the range difference.

When repeat-pass InSAR is used and surface motion occurs during the two passes, the range difference is also affected by the surface motion. The range difference due to the surface motion is

$$\Delta_{motion} = d \cdot \cos(90 - (\mathbf{q} + \mathbf{a})) = d \cdot \sin(\mathbf{q} + \mathbf{a}) \quad (2.7)$$

where d is surface displacement on the ground in the cross-track direction, α is the surface slope in the range direction, and θ is the incidence angle (same as look angle here).

Joughin (1995) expresses surface displacement using the changes in the y and z direction as

$$\Delta_{motion} = (y_2 - y_1) \sin \mathbf{q} - (z_2 - z_1) \cos \mathbf{q} \quad (2.8)$$

where y_1, z_1 are the target positions defined in Figure 2.1 at the first pass observation, and y_2, z_2 are the position of the same target at the second pass observation.

2.2.2 Phase measurement

The range difference, whether caused by topography, or surface displacement, or both, can be measured by the normal range resolution of SAR. The accuracy of this measurement is limited by the pixel resolution (several meters) and is far too inaccurate to detect topography or surface motion. The most interesting thing in interferometric SAR is using phase to measure the range difference. The accuracy of the phase measurement is a fraction of the wavelength, which is a few centimeters for C-band radar.

For a distributed target, pixel (i,j) in two complex SAR images can be represented as (Rodriguez and Martin, 1992):

$$s_1(i, j) = A_1(i, j)e^{jf_1} \quad (2.9)$$

$$f_1 = \text{mod}\left(\frac{4p}{\lambda} r_1, 2p\right) \quad (2.10)$$

$$s_2(i, j) = A_2(i, j)e^{jf_2} \quad (2.11)$$

$$f_2 = \text{mod}\left(\frac{4p}{\lambda} r_2, 2p\right) \quad (2.12)$$

where $s_1(i, j)$ and $s_2(i, j)$ are complex values of the SAR image pixels at (i,j); $A_1(i,j)$ and $A_2(i,j)$ are the terrain reflectivity (backscattering) of the two images; ρ_1 and ρ_2 are the ranges respectively from successive antenna positions S_1 and S_2 to the ground resolution element $P(x,y,z)$ associated with image pixel (i,j); λ is the radar wavelength; ϕ_1 and ϕ_2 are the phases of the returned radar signal in two images. Then, the two complex images s_1 and s_2 can be interfered with each other by conjugate multiplication to form a complex interferogram. A pixel in the interferogram can be expressed as

$$s_1(i, j) \cdot s_2^*(i, j) = A_1(i, j)A_2(i, j)e^{(f_1-f_2)} \quad (2.13)$$

The phase difference of the two complex images, $\phi_1 - \phi_2$, is related to the range shift $\rho_1 - \rho_2$. Although ϕ_1 and ϕ_2 are uniformly distributed, their difference is no longer uniformly distributed, if the two complex images are correlated. With good coherence, an interferogram pixel with phase ϕ can infer the range difference

$$\Delta = r_2 - r_1 = \frac{1}{4p}(2pn + f) \quad (2.14)$$

Because ϕ is modulo 2π , there is an integer uncertainty in the absolute phase. Phase unwrapping converts the wrapped phase to an unwrapped phase, with only one integer uncertainty for all pixels. This integer then is determined from a single ground control point. Absolute and unwrapped phase have a constant difference for all pixels. Assume Φ is the absolute phase and ϕ represents the wrapped phase before phase unwrapping. Then their relationship is

$$\Phi = 2pn + f \quad (2.15)$$

and the range shift is

$$\Delta = \frac{1}{4p}\Phi \quad (2.16)$$

The phase measurement has a relative accuracy as good as a fraction of wavelength (Rodriguez and Martin, 1992). The absolute accuracy of the phase depends on the control points. Errors in control points directly propagate to the phase measurement. We will discuss this later.

2.2.3 Phase separation

For repeat-pass interferometry, the unwrapped phase is related to baseline, DEM, and surface motion. So the absolute phase Φ can be expressed as the sum of the phases due to these individual contributions.

$$\Phi = \Phi_{baseline} + \Phi_{DEM} + \Phi_{motion} \quad (2.17)$$

These individual components can be approximated as (Fatland, 1998)

$$\Phi_{baseline} = \frac{2kB_n}{r \tan J} \quad (2.18)$$

$$\Phi_{DEM} = \frac{2kB_n H}{r \sin J} \quad (2.19)$$

$$\Phi_{motion} = 2kVT \sin J \quad (2.20)$$

where B_n is the perpendicular baseline, $k=2\pi/\lambda$, λ is the radar wavelength, r is the distance from satellite to the scene center, θ is the look angle, V is the surface velocity on the ground in the cross track direction, and T is the time interval between the two passes.

Both the baseline phase and the DEM phase are linearly proportional to the perpendicular baseline B_n . The DEM phase is also linearly proportional to elevation. The motion phase is related to the surface velocity and the look angle.

Among the three phase components, the baseline phase is always calculable when the baseline and satellite parameters are known. The DEM and motion phase remain as a sum and so the problem is how to separate these two components. If we know one component, then we can estimate the other component by subtracting the known component from the measured phase. Some example combinations follows:

1. No surface motion. $\Phi_{\text{motion}}=0$. Then the DEM phase $\Phi_{\text{DEM}}=\Phi-\Phi_{\text{baseline}}$. The topography can be estimated from the measured phase.
2. Known surface topography, DEM phase Φ_{DEM} can be simulated from the topography and the satellite orbit parameters. Then the motion phase $\Phi_{\text{motion}}=\Phi-\Phi_{\text{baseline}}-\Phi_{\text{DEM}}$. Surface motion can be estimated from the measured phase.
3. Baseline $B=0$. Then the DEM phase $\Phi_{\text{DEM}}=0$, and the baseline phase $\Phi_{\text{baseline}}=0$. The motion phase is the measured phase. $\Phi_{\text{motion}}=\Phi$. This case very rarely happens. But when the baseline is near zero, the effect of topography is negligible and can be ignored (Goldstein and others, 1993; Joughin and others, 1996b).
4. Given two interferograms with the same repeat interval and different baselines, the motion phase can be canceled and topography can be calculated from the difference of the two baselines. Then the topography phase can be removed to estimate the motion phase. This is called double difference interferometry. The assumption for this application is that the surface motion is constant for the two repeat intervals. This assumption is valid for most ice sheet applications, unless there is a glacier surge or some radical dynamic change.
5. Given two interferograms with the same baseline but different repeat intervals, then the topography phase can be canceled and the motion phase is the difference of the two measured phases. Once the motion phase is estimated, we can remove it from the measured phase to estimate topography. This is another kind of double difference interferometry.

2.3 SAR interferometry processing

2.3.1 Processing overview

SAR interferometric processing procedures vary with applications and available data. Applications could be elevation extraction or surface motion estimation. Data may be two-cycle data or three-cycle data. Nevertheless, there are some standard procedures for all cases. They are single complex image (SLC) co-registration, interferogram formation, phase unwrapping, baseline refinement, and image geocoding. In this section, the basic procedures that apply to all applications will be discussed. Application-dependent procedures will be discussed in the next section. A detailed discussion of interferometric processing methods can also be found in Joughin (1995).

2.3.2 SLC images co-registration

SLC co-registration is the first step in InSAR processing. To generate an interferogram, two SLC images taken from the two passes must be co-registered so that the same pixel position in the two images reflects the same ground patch. If two images are not properly registered, co-registration decorrelation occurs. SLC co-registration is the process of resampling the second SLC image into the same geometry as the first SLC image. The process involves geometry mapping and radiometric interpolation. Geometry mapping creates a pixel relationship between the two SLC images with sub-pixel accuracy. Radiometric interpolation creates a resampled SLC image of the second image based on the geometry mapping.

Geometry mapping starts with tie point matching between points regularly defined in the first image and their conjugate points in the second image. The matching results are

range offsets and azimuth offsets of the tie points. There are magnitude-based matching methods and phase-based methods (Gabriel and others, 1988). Sub-pixel accuracy is achieved by a peak interpolation of the correlation function. Since the speckle matching technique to be discussed in Chapter 3 uses the same tie-point matching idea, we will discuss the tie point matching methods, peak interpolation methods, and matching accuracy in detail in Chapter 3.

Once the tie points are found, we need to create relationships between the first image position (x,y) and the second image position (x',y') written as

$$x' = f_x(x, y) \quad (2.21)$$

$$y' = f_y(x, y) \quad (2.22)$$

where f_x and f_y are the geometric transformations for the range and azimuth directions from the first image to the second image. A commonly used geometric transformation is an affine transformation, which is a linear mapping from the first image to the second image. The affine transformation models are described as

$$x' = a_0 + a_1x + a_2y \quad (2.23)$$

$$y' = b_0 + b_1x + b_2y \quad (2.24)$$

For most applications, the affine transformation is adequate to achieve high quality interferograms. However, for application of RADARSAT InSAR over the East Antarctic, a long repeat cycle (24 days) and fast-moving glaciers make it impossible for an affine transformation to fit the range offset and azimuth offset in a linear model with acceptable error. For this research, a Delaunay triangulation based mapping method is used to establish a position relationship between images based on local tie points rather than

global tie points. The method improves the coherence and interferogram quality for fast moving areas. Delaunay triangulation based co-registration will be discussed in Chapter 4 in detail.

Radiometric interpolation calculates complex pixel values at a non-integer positions (x', y') of the second image. According to sampling theory, if the SAR data are sampled at a frequency larger than the Nyquist frequency, the SAR data can be completely reconstructed from the values at discrete integer positions. Then the value at a non-integer position can be calculated.

Assume $x(t)$ is a continuous function, $x(nT)$ are discrete samples at a sampling rate equal to or larger than the Nyquist rate, and T is the sampling interval, then the reconstructed function $x_r(x)$ can be expressed as the convolution of the sampling data with a sinc function of infinite extent (Curlander and McDonough, 1991).

$$x_r(t) = \sum_{n=-\infty}^{\infty} x(nT) \operatorname{sinc} \left(\frac{\mathbf{p}(t - nT)}{T} \right) \quad (2.25)$$

Then the function value at a position $t' = nT + \delta T$, shifted away δT from an integer position nT , can be calculated as

$$\begin{aligned} x_r(t') &= x_r(mT + \mathbf{dT}) = \sum_{n=-\infty}^{\infty} x(nT) \operatorname{sinc} \left(\frac{\mathbf{p}(mT + \mathbf{dT} - nT)}{T} \right) \\ &= \sum_{n=-\infty}^{\infty} x(nT) \operatorname{sinc} (\mathbf{p}(m + \mathbf{d} - n)) \end{aligned} \quad (2.26)$$

The interpolation is a convolution of the SAR image with a sinc function of infinite extent. In practice a truncated sinc function with finite size is used in data processing and errors are introduced. A larger size sinc function will decrease the error, but increase the computational complexity.

Convolution can also be implemented in the frequency domain. First, the Fast Fourier Transform (FFT) of the data is computed. Then the result is multiplied by a complex exponential. The inverse transformation of the product yields the shifted result. The advantages of frequency implementation are the speed and the ability to filter data. In Vexcel's software, the range and azimuth directions are processed separately. Since there are phase ramps in the range direction due to the baseline effect and a phase ramp in the azimuth direction due to the Doppler frequency, the phases must be shifted to zero center before interpolation and shifted back after interpolation.

Low pass filtering is also applied to the resampled image and to the master image to reduce decorrelation due to mismatch of Doppler centroids of the two orbits (Joughin, 1995). The filter is designed to keep the common frequency and remove non-overlapping frequencies where there is no coherence (Bamler and others, 1993). Assume two orbits have Doppler centroid difference of 300 HZ, the SAR processor bandwidth is 900 for both orbits. The overlap bandwidth will then be 600HZ. For AMM-1 InSAR data over the East Antarctic Ice Streams, the overlap bandwidth is larger than half bandwidth of the processor. Table 2.1 lists Doppler centroids of two orbits and their difference.

Frame	Orbit 9822 Dopp (Hz)	Orbit 10165 Dopp (Hz)	Difference (Hz)
5556	2853	3194	341
5572	3015	3351	336
5589	3191	3523	332
5605	3317	3642	325
5622	3490	3806	316

Table 2.1 Doppler centroids and their difference for InSAR orbits 9822/10165

2.3.3 Calculate interferogram

Measured phase and coherence

After the two complex images are co-registered, the complex interferogram I , a conjugate multiplication between the first complex image s_1 and the second complex image s_2 , can be calculated as

$$I(i, j) = s_1(i, j) \cdot s_2^*(i, j) = A_1(i, j)A_2(i, j)e^{(f_1-f_2)} \quad (2.27)$$

Here s_1 filtered image and the s_2 is filtered and resampled image. To reduce phase noise, the interferogram is multilook averaged. In this research, we use a 2 by 8 averaging. That means we average complex values of all pixels in a window of 2 pixels in the range direction and 8 pixels in the azimuth direction. The averaged interferogram has reduced resolution by 2 in range direction and by 8 in azimuth direction. The interferogram is expressed as complex data rather than phase data, since complex data have a better averaging performance than phase. It is also easier to subtract phase from complex data (Joughin, 1995).

Coherence, a quality indicator of the interferogram, is a normalized magnitude of the interferogram. If we assume a multilook averaging window is N by M , then the coherence γ can be calculated as

$$g = \frac{\left| \sum_{i=1}^N \sum_{j=1}^M s_1(i, j) s_2^*(i, j) \right|}{\sqrt{\left(\sum_{i=1}^N \sum_{j=1}^M s_1(i, j) s_1^*(i, j) \right) \left(\sum_{i=1}^N \sum_{j=1}^M s_2(i, j) s_2^*(i, j) \right)}} \quad (2.28)$$

Baseline phase and topography phase

Baseline and topography contribute to a phase change in the interferogram. Their combined effect on the phase can be approximated as (Joughin and others, 1996b)

$$\Phi = 2k \left(-B_n \sin \mathbf{q}_d - B_p \cos \mathbf{q}_d + \frac{B^2}{2r_0} \right) \quad (2.29)$$

where θ_d is the difference between the look angle θ and the image center look angle θ_c , $\theta_d = \theta - \theta_c$. B_n and B_p are the perpendicular baseline and parallel baseline respectively, the look angle of a point with elevation z can be expressed as (Olmsted, 1993)

$$\mathbf{q} = a \cos \left(\frac{r_0^2 + 2R_e(H - z) + H^2 - z^2}{2(R_e + H)r_0} \right) \quad (2.30)$$

If we assume the elevation, then the look angle (eq. 2.30) becomes

$$\mathbf{q}_{flat} = a \cos \left(\frac{r_0^2 + 2R_e H + H^2}{2(R_e + H)r_0} \right) \quad (2.31)$$

The phase calculated from Equations 2.29 and 2.31 is called the baseline phase. Since it is a special case of topography with elevation $z=0$, the topography phase also refers to the phase including both the baseline and topography effect. We will use this convention in this dissertation unless indicated.

2.3.4 Phase reconciliation

The measured interferometric phase from SAR images is wrapped into the interval $(-\pi, \pi)$. There is a modulo- 2π ambiguity in the phase. To calculate surface motion or to estimate surface elevation, we have to remove the modulo- 2π ambiguity and convert the wrapped value into an unwrapped value.

Many phase unwrapping algorithms have been developed (Goldstein and others , 1988; Ghiglia and Romero, 1994; Xu and Cumming, 1999; Ghiglia and Pritt, 1998). These algorithms have limitations associated with data on fast moving glaciers. In this research, a phase reconciliation algorithm is developed to overcome such limitations after phase unwrapping. Detailed discussions of the new method with review of existing methods are presented in Chapter 5.

2.3.5 Baseline refinement

The baseline can be calculated from the ephemeris data, but this information may be inaccurate. To refine a baseline, we need tie points of known elevations. These tie points are used in a least squares adjustment to estimate baseline parameters. The least squares equation for baseline refinement is given by Joughin (1995) as

$$\Phi_{unwrap} - \frac{kB^2}{r^0} + \frac{k\Delta^2}{r^0} = -2k \left(\left(B_n^c + dB_n \left(\frac{x-x_c}{L_x} \right) \right) \sin \mathbf{q}_d + B_p^c \cos \mathbf{q}_d \right) - \Omega_x (x - x_c) \cos \mathbf{q}_d \quad (2.32)$$

where four unknown parameters are:

B_n^c : Perpendicular baseline at frame center

B_p^c : Parallel baseline at frame center

δB_n : Gradient of perpendicular baseline change along flight track

Ω_x : Azimuth phase ramp

Other symbols are known values. Φ_{unwrap} is the unwrapped phase. B is the baseline from orbit information. Δ is the range difference. x is azimuth position and x_c is the azimuth position of the frame center. L_x is the azimuth length of the frame. θ_d is the look angle difference between the tie point and frame center.

Equation (2.32) assumes stationary tie points. In Chapter 6, we will extend it to velocity control points that have a known velocity. Also, we will consider the azimuth direction offset in baseline refinement.

2.3.6 Data geocoding

Image geocoding is a process of converting data in slant range coordinates into ground range coordinates with terrain correction. The data include SAR data, coherence data, interferogram data, velocity data, and so on. SAR interferometric processing is performed on slant range data. The final result should be mapped into a GIS environment in ground coordinates. In this research, we use an inverse process to do data geocoding. For example, we have velocity measured on a regular point grid in slant range coordinates. We then define a regular grid in ground coordinates. We use a SAR geometry model (Olmsted, 1993; Wivell and others, 1992) to find corresponding positions in the slant range coordinates. Then we assign data values (such as velocity or coherence) in slant range coordinates to points in ground coordinates. Interpolation is needed to pick a value from the slant range coordinates. We use this approach for creating the coherence and velocity mosaics.

SAR geocoding is the inverse of the SAR satellite model. It uses accurate satellite orbit information, sensor information, and a DEM to simulate slant range SAR image coordinates. For any given point on the ground with latitude, longitude and elevation, we will use the SAR model to calculate its position (i,j) on the slant range SAR image

To find SAR image position (i,j) for DEM point (X,Y,Z) , we use a variation of the inverse model developed by the USGS EROS Data Center (EDC) (Wivell and others,

1992). We simplify the problem by reducing the search root to one dimension, namely time t . For DEM point (X,Y,Z) , we have a position on the earth's surface in the form of (latitude, longitude, elevation), and its ECI (Earth Centered Interial) coordinates $R_T(t)$ at time t according to sidereal rotation. For the moving satellite, we can calculate the satellite position $R_S(t)$ at time t according to orbit ephemeris data. We can use a harmonic model to describe the satellite position vector $R_S(t)$, velocity vector $V_S(t)$, and velocity acceleration vector $A_S(t)$. Similarly, we can use a harmonic model to describe the target position vector $R_T(t)$ and velocity vector $V_T(t)$. Given a time t , we can calculate the range $R(t)=|R_S(t)-R_T(t)|$. Then using range and azimuth sampling rates we can get an image position $(i(t), j(y))$. For the SAR model, we need to satisfy the Doppler frequency condition

$$f_D(i(t), j(y)) - f_D(t) = 0 \quad (2.33)$$

where $f_D(i(t), j(y))$ is the calculated Doppler frequency at image position $(i(t), j(t))$ from SAR metadata, and

$$f_D(t) = -\frac{2}{R(t)}(R_S - R_T) \bullet (V_S - V_T) \quad (2.34)$$

is the modeled Doppler frequency.

We use the Newton-Raphson iteration to interactively find a solution for time t

$$\Delta t = (f_D(i(t), j(t)) - f_D(t)) \Big/ \frac{df_D(t)}{dt} \quad (2.35)$$

where

$$\frac{df_D(t)}{dt} = -\frac{2}{R(t)} \left((R_S(t) - R_T(t)) \bullet (A_S(t) - A_T(t)) + |V_S(t) - V_T(t)|^2 - ((R_S(t) - R_T(t)) \bullet (V_S(t) - V_T(t)) / R(t))^2 \right) \quad (2.36)$$

We can directly calculate ground position (X,Y,Z) from slant range image position (i,j) if we have a DEM model. For the slant range image position (i,j) , the range position j defines a sphere whose center is at the satellite and the radius is the range of the pixel. Azimuth position i defines a Doppler cone whose axis is the line from the satellite to the target. The intersection curve of the cone and the sphere is the solution of ground positions whose image point is (i,j) . If we have a DEM model, the intersection of the curve with the DEM surface will be a ground point (X,Y,Z) for slant range image position (i,j) . Because the DEM is a discrete model, we use an iterative approach to find a solution.

Based on the four corner point coordinates of a slant range image frame, we can estimate the approximate ground position (X,Y) of a slant range image pixel (i,j) . Then from the DEM we can find elevation Z for position (X,Y) . We use the SAR simulation discussed above to find image position (i',j') for a ground position (X,Y,Z) . The difference between the new image position (i',j') and target pixel position (i,j) yield the adjustment $(\Delta X, \Delta Y)$ on a ground position. The new ground position is $X'=X+\Delta X$, $Y'=Y+\Delta Y$, and Z' . The SAR simulation process is repeated until the new image position (i', j') is close to (i,j) within a threshold. In this case, the new ground (X',Y',Z') is the ground position of image pixel (i,j) . In our process, it takes less than 5 cycles to converge to the target pixel. This approach will be used to find an initial value for the tie point matching discussed in Chapter 3.

2.4 SAR interferometry applications

2.4.1 Elevation estimation

The interferometric SAR (InSAR) technique has emerged as a precise approach to the extraction of high-resolution elevation data (Zebker and Goldstein, 1986; Rodriguez and Martin, 1992; Zebker and others 1994). For areas where there is no motion, the interferometric phase is caused only by topography and satellite geometry. From Figure 2.1 geometry, the height of ground point (x,y,z) is expressed as

$$z(x, y) = H - r_0 \cos(\mathbf{q}) = H - r_0 [\cos \mathbf{x} \sqrt{1 - \sin^2(\mathbf{q} - \mathbf{x})} - \sin(\mathbf{q} - \mathbf{x}) \sin \mathbf{x}] \quad (2.37)$$

where H is the satellite height, r_0 is the range of the first pass, ξ is the baseline angle, and θ is the look angle. The term $\sin(\theta - \xi)$ can be determined by the range difference Δ , the range of the first pass r_0 and baseline B in the following equation

$$\sin(\mathbf{q} - \mathbf{x}) = \frac{r_0^2 + B^2 - (r_0 + \Delta)^2}{2r_0B} \quad (2.38)$$

The range difference Δ can be calculated from an unwrapped phase Φ as

$$\Delta = \frac{l}{4p} \Phi \quad (2.39)$$

The elevation accuracy estimated from interferometric SAR depends on errors in the baseline B , range difference Δ , satellite height H , and the interferometric phase Φ . Elevation error related to the error of individual parameters is given by Rodriguez and Martin (1992) as

$$dz_B = -r_0 \tan(\mathbf{q} - \mathbf{x}) \sin(\mathbf{q}) \frac{dB}{B} \quad (2.40)$$

$$dz_x = -r_0 \sin(\mathbf{q}) d\mathbf{x} \quad (2.41)$$

$$dz_H = dH \quad (2.42)$$

$$dz_{r_0} = -\cos(\mathbf{q})dr_0 \quad (2.43)$$

$$dz_\Phi = \frac{r_0 \sin(\mathbf{q})}{2kB \cos(\mathbf{q} - \mathbf{x})} d\Phi \quad (2.44)$$

Among the errors, the phase error ($d\Phi$) is a random error caused by thermal noise in SAR acquisition and other processing steps. The noise is independent from pixel to pixel and can be reduced by averaging. The standard deviation of phase noise σ_Φ is determined by the image coherence γ as (Hagberg and others 1995)

$$\mathbf{s}_\Phi = \frac{1}{\sqrt{2N}} \frac{\sqrt{1-\mathbf{g}^2}}{\mathbf{g}} \quad (2.45)$$

where N is the number of averaging pixels. Expanding (2.45) around $1-\gamma$ becomes

$$\mathbf{s}_\Phi \approx \sqrt{\frac{1-\mathbf{g}}{N}} \quad (2.46)$$

Baseline, satellite height, and range distance introduce systematic errors. These errors introduce long wavelength errors in elevation. They may be removed by using more control points (Rodriguez and Martin, 1992).

It should be noted that the elevation error due to the baseline (Equation 2.40) and elevation error due to phase (Equation 2.44) are inversely proportional to baseline. It suggests that longer baseline reduces the sensitivity to the baseline error and phase error. However, as the baseline becomes longer, the baseline decorrelation increases the phase error. As a result, elevation error increases. So an optimal baseline must be chosen to balance all these factors.

When repeat-pass interferometry is used to extract ice sheet elevation estimation, we have to consider ice motion. Ignoring ice motion in the process will cause a significant elevation error, because the elevation is so sensitive to phase. Assume that ice motion is 1 m/year, the perpendicular baseline is 200 m, the look angle is 35°, and the range distance is 900 km, then the elevation error will be as large as 97 m. If we know the surface velocity, we can remove the phase due to surface motion.

When more than two passes of SAR data are available, differential interferometry can be used to separate the topography component and surface motion component of phase by a double difference technique (Kwok and Fahnestock, 1996; Joughin and others, 1996b).

2.4.2 Surface motion estimation

With repeat-pass interferometry, the phase change due to surface motion can be extracted by subtracting the topographic related phase from the measured phase as in Equation (2.17)

$$\Phi_{motion} = \Phi - \Phi_{topography} \quad (2.47)$$

where $\Phi_{topography}$ is used to represent the combined DEM and baseline effects. If we assume the surface velocity is constant between two observations of period T, the surface velocity in the cross-track direction on the ground can be estimated as

$$V = \frac{\Phi_{motion}}{2kT \sin\gamma} \quad (2.48)$$

where Ψ is the incidence angle. Now we can estimate error budgets for surface velocity due to phase noise, elevation error, and baseline error. From (2.48), the velocity uncertainty σ_v due to random phase noise σ_Φ is

$$\mathbf{s}_v = \frac{1}{2kT \sin \mathbf{y}} \mathbf{s}_\Phi \quad (2.49)$$

The phase error σ_Φ due to DEM error σ_z is (Joughin and others 1996a)

$$\mathbf{s}_\Phi = \frac{2kB_n}{r \sin \mathbf{q}_c} \mathbf{s}_z \quad (2.50)$$

where θ_c is the look angle of the image center. Combining Equations (2.49) and (2.50), the velocity error σ_v due to elevation error σ_z is

$$\mathbf{s}_v = \frac{B_n}{rT \sin \mathbf{q}_c \sin \mathbf{y}} \mathbf{s}_z \quad (2.51)$$

and ψ is the incidence angle. The baseline effect on phase has an elevation-independent phase ramp. The phase error σ_Φ due to baseline error σ_{B_n} is

$$\mathbf{s}_\Phi = \frac{2k}{r \sin \mathbf{q}_c} (r - r_c) \mathbf{s}_{B_n} \quad (2.52)$$

Then velocity error σ_v due to baseline error σ_{B_n} is

$$\mathbf{s}_v = \frac{1}{rT \sin \mathbf{q}_c \sin \mathbf{y}} (r - r_c) \mathbf{s}_{B_n} \quad (2.53)$$

Most InSAR applications on ice motion use the assumption of surface-parallel flow (Joughin and others, 1998; Mohr and others, 1998, Fatland and others, 1998, Gray and others, 2001). This assumption neglects the contribution to the vertical change of the

local balance such as snow accumulation. Reeh and others (1999), applying the principle of mass conservation, derived equation relating the vertical surface velocity to the horizontal velocity vector as well as surface balance. In this research, vertical change due to snow accumulation is 0.004 m for the research region during 24 days. It is negligible.

Random error for surface velocity is from phase noise. For typical data of this research, coherence value γ is around $\gamma=0.4$. Using multi look 2 by 8 averaging, phase noise is $\sigma_\phi=0.2$ rad according to Equation 2.46. Using 27° for incidence angle, the error in the cross track velocity is calculated from Equation 2.49 as $\sigma_\phi=0.03$ m/year.

The systematic errors are from baseline error. Baseline error can be mediated with ground control points (GCPs). So GCP errors propagate into the velocity errors. Jezek (1999b) analyze the systematic error for RADARSAT InSAR data. The systematic error is 3.5 m/year. Combining systematic error and random error, the cross track velocity error is better than 4 m/year. In the later discussion, we use 4 m/year as the velocity error from the interferometry technique.

2.4.3 Double difference interferometry

Estimate topography

We assume the surface velocity is consistent. Then the two interferograms contain the same surface motion phase. The motion phase can be canceled by differencing two interferograms. Assume Φ_1 is the first interferogram after the baseline phase ramp has been removed. Φ_1 can be expressed as an elevation-dependent term and motion term

$$\Phi_1 = \frac{-2kB_1}{r \sin \mathbf{q}} z + 2k\Delta \quad (2.54)$$

Similarly, we have an equation for the second interferogram

$$\Phi_2 = \frac{-2kB_2}{r \sin \mathbf{q}} z + 2k\Delta \quad (2.55)$$

Differencing Equations (2.54) and (2.55) yields

$$\Phi_1 - \Phi_2 = \frac{-2k(B_1 - B_2)}{r \sin \mathbf{q}} z \quad (2.56)$$

Equation (2.56) suggests that the new interferogram $\Phi_1 - \Phi_2$ is a formation of topography-only with baseline $B_1 - B_2$. Once the topography is determined, it can be substituted into (2.54) or (2.55), and surface motion can be estimated.

As discussed before, in a single interferogram, a larger baseline is better for elevation extraction and a smaller baseline is better for motion estimation. In the double difference case, two larger baselines B_1 and B_2 can't guarantee larger baseline $B_1 - B_2$ in the equation. So the optimal baseline selection in the double difference technique is that one baseline is larger, while the other one is small. Then the difference phase will be sensitive to the elevation, and the elevation accuracy will increase. The surface motion calculation uses Equation (2.54) or Equation (2.55), whichever has a smaller baseline.

Estimate motion

Assume two interferograms have the same baseline. Then the topography phases in both interferograms are the same, and they can be canceled. Assume V is surface velocity and is constant during the observations, and T_1 and T_2 are time intervals of the two interferograms, the measured phase in both interferograms can be expressed as

$$\Phi_1 = \frac{-2kB}{r \sin \mathbf{q}} z + 2kT_1V \sin \mathbf{q} \quad (2.57)$$

$$\Phi_2 = \frac{-2kB}{r \sin \mathbf{q}} z + 2kT_2V \sin \mathbf{q} \quad (2.58)$$

Differencing Equations (2.57) and (2.58) yields

$$\Phi_1 - \Phi_2 = 2kV \sin \mathbf{q} (T_1 - T_2) \quad (2.59)$$

Since T_1 and T_2 are different, the surface velocity can be calculated as

$$V = \frac{\Phi_1 - \Phi_2}{2k \sin \mathbf{q} (T_1 - T_2)} \quad (2.60)$$

Once motion has been estimated, we can substitute the motion phase into Equations (2.57) or (2.58), and the topography can be estimated.

CHAPTER 3

SPECKLE MATCHING TECHNIQUE

3.1 Introduction

Speckle matching (also called speckle tracking, or speckle correlation) uses a cross-correlation matching technique to track surface motion from repeat-orbit InSAR image pairs (Gray and others, 1998). Speckle matching measures range offsets and azimuth offsets for a grid of points. The range offsets and azimuth offsets are then calibrated to calculate surface motion in the range and azimuth directions. The calibration (or registration) of these offsets needs to remove topography and baseline effects. Control points are also needed in the calibration.

Cross-correlation has been successfully used in optical satellite imagery to track surface features for use in estimating motion on ice streams (Bindschadler and Scambos, 1991). But the matching relies only on visible features like crevasses. On SAR images, speckle patterns are correlated. Speckle matching can track motion for almost any position on a SAR image. Procedures to estimate ice motion from speckle matching include two steps. First, we generate tie points by matching the speckle patterns between images. Second, tie points, or offsets, are calibrated to calculate surface motion. The first procedure is similar to that used in image co-registration. In this chapter, we review the

speckle matching methods. Velocity calibration is then discussed. Last, we compare the two methods of interferometry and speckle matching.

3.2 Review of matching methods

3.2.1 Cross-correlation

Cross-correlation is a magnitude based matching method. Figure 3.1 illustrates the matching scheme. For a point P in Image 1, we seek its conjugate point in Image 2. A template window of $M \times N$ pixels, in which point P is the center, is created in Image 1. A matching window of the same size in Image 2 is used to calculate the cross-correlation between the two windows. We move the matching window inside the searching window and calculate every cross-correlation factor between the template window and the matching window.

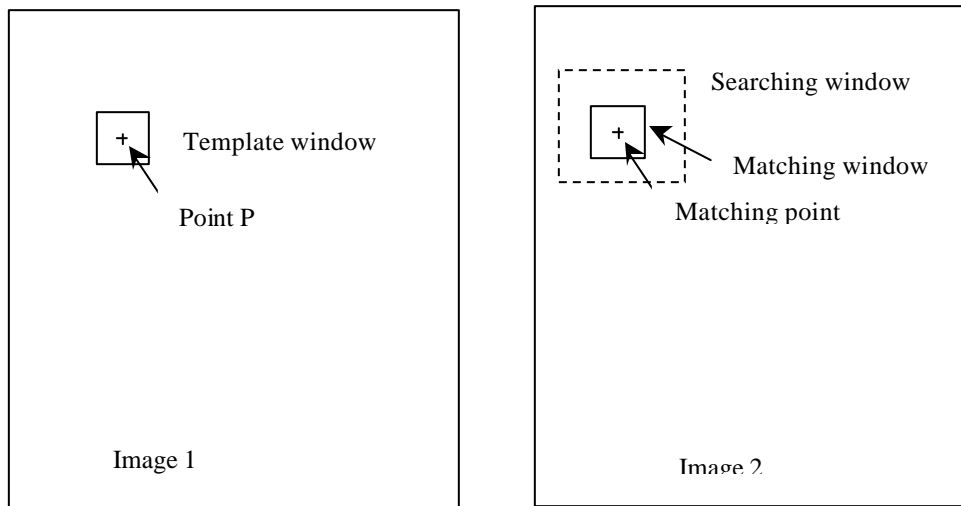


Figure 3.1: Cross-correlation matching

The cross-correlation factor ρ of two windows is defined as (Schenk, 1999)

$$\mathbf{r} = \frac{\mathbf{S}_{12}}{\mathbf{S}_1 \mathbf{S}_2} \quad (3.1)$$

Assume $s_1(i,j)$ is the magnitude value of the pixel (i,j) in the template window, $s_2(i,j)$ is magnitude value of the pixel (i,j) in the matching window in Image 2, i and j are the relative pixel positions inside the windows, then σ_{12}, σ_1 , and σ_2 have the following definition

$$\bar{s}_1 = \frac{\sum_{i=1}^M \sum_{j=1}^N s_1(i, j)}{M \cdot N} \quad (3.2)$$

$$\bar{s}_2 = \frac{\sum_{i=1}^M \sum_{j=1}^N s_2(i, j)}{M \cdot N} \quad (3.3)$$

$$\mathbf{s}_1 = \sqrt{\frac{\sum_{i=1}^M \sum_{j=1}^N (s_1(i, j) - \bar{s}_1)^2}{M \cdot N - 1}} \quad (3.4)$$

$$\mathbf{s}_2 = \sqrt{\frac{\sum_{i=1}^M \sum_{j=1}^N (s_2(i, j) - \bar{s}_2)^2}{M \cdot N - 1}} \quad (3.5)$$

$$\mathbf{s}_{12} = \frac{\sum_{i=1}^M \sum_{j=1}^N ((s_1(i, j) - \bar{s}_1) \cdot (s_2(i, j) - \bar{s}_2))}{M \cdot N - 1} \quad (3.6)$$

The correlation value ρ is between -1 and 1 . $\rho=1$ indicates that the two windows are identical. If there is no similarity at all between them, then $\rho=0$.

3.2.2 Sub-pixel accuracy calculation

Cross-correlation matching finds a maximum correlation at an integer position. We need a sub-pixel interpolation method to find the sub-pixel offset in the range and azimuth direction. Assume (i, j) is the position in Image 2 that has the largest correlation $\rho(i, j)$, then nine correlation factors shown in Figure 3.2 will be used to calculate the sub-pixel position.

$\rho(i-1, j-1)$	$\rho(i, j-1)$	$\rho(i+1, j-1)$
$\rho(i-1, j)$	$\rho(i, j)$	$\rho(i+1, j)$
$\rho(i-1, j+1)$	$\rho(i, j+1)$	$\rho(i+1, j+1)$

Figure 3.2: Maximum correlation and its 8 neighbors

Based on the 3x3 matrix, the real maximum position can be calculated using methods such as surface fitting, parabolic fitting, and the barycenter method.

Surface fitting

Define a second order polynomial surface as

$$F(x, y) = ax^2 + by^2 + cxy + dx + ey + f \quad (3.7)$$

where a,b,c,d,e, and f are surface parameters. These six parameters can be solved using least squares by creating nine equations from the known correlation factors. Then the maximum F is reached at position (x, y) which satisfies

$$\frac{\partial F}{\partial x} = 2ax + cy + d = 0 \quad (3.8)$$

$$\frac{\partial F}{\partial y} = 2by + cx + e = 0 \quad (3.9)$$

(3.8) and (3.9) yield solutions

$$x = \frac{2bd - ec}{c^2 - 4ab} \quad (3.10)$$

$$y = \frac{2ae - dc}{c^2 - 4ab} \quad (3.11)$$

Parabolic fitting

In parabolic fitting, we calculate the sub-pixel peak in the range and azimuth directions separately. Three points $\rho(i-1,j)$, $\rho(i,j)$, and $\rho(i+1,j)$ are used to calculate the range direction offset x as

$$x = i + \frac{\mathbf{r}(i-1, j) - \mathbf{r}(i+1, j)}{4 \left(\frac{\mathbf{r}(i-1, j) - \mathbf{r}(i+1, j)}{2} - \mathbf{r}(i, j) \right)} \quad (3.12)$$

Similarly, azimuth direction offset is calculated using three points $\rho(i,j-1)$, $\rho(i,j)$, and $\rho(i,j+1)$ as

$$y = j + \frac{\mathbf{r}(i, j-1) - \mathbf{r}(i, j+1)}{4 \left(\frac{\mathbf{r}(i, j-1) - \mathbf{r}(i, j+1)}{2} - \mathbf{r}(i, j) \right)} \quad (3.13)$$

Barycenter method

Consider the sub-pixel position as the barycenter of correlation. The range offset, x and azimuth offset, y can be expressed as a weighted averages (Michel and others, 1999)

$$x = \frac{\sum_{k=i-1}^{i+1} \sum_{l=j-1}^{j+1} k \mathbf{r}^2(k, l)}{\sum_{k=i-1}^{i+1} \sum_{l=j-1}^{j+1} \mathbf{r}^2(k, l)} \quad (3.14)$$

$$y = \frac{\sum_{k=i-1}^{i+1} \sum_{l=j-1}^{j+1} l \mathbf{r}^2(k, l)}{\sum_{k=i-1}^{i+1} \sum_{l=j-1}^{j+1} \mathbf{r}^2(k, l)} \quad (3.15)$$

We tested the three methods and found that they agree to within 0.05 pixels. The surface fitting method, which calculates in a two-dimensional space is slower than the other two methods, which processes in a one-dimension space. Since the correlation is separable in the range and azimuth direction (Joughin, 1995), two one-dimensional calculations can result in a peak of two-dimensional and the calculation is fast.

3.2.3 Accuracy and complexity of matching

Random error in cross-correlation speckle matching is derived by Bamler (1999) as

$$\sigma_{x,y} = \sqrt{\frac{3}{2N}} \frac{\sqrt{1-\mathbf{g}^2}}{\mathbf{p}\mathbf{g}} \text{osf}^{3/2} \quad (3.16)$$

where $\sigma_{x,y}$ is the standard deviation of the range or azimuth offset estimate (unit: pixel), N is the number of pixels in the matching window, \mathbf{g} is the coherence of the interferometric data pair, and osf is the oversampling factor of the data. For typical data sets, assume N is 4096, coherence \mathbf{g} is 0.3, and the oversampling factor is 1 (no oversampling), then the uncertainty of the cross-correlation matching is 0.02 pixel. Such

0.02 pixel uncertainty corresponds to a velocity error of about 2 m/year in the azimuth direction and about 6 m/year in the cross track direction for RADARSAT standard radar beams. We will use these numbers in later error budget discussion.

Systematic error is observed when using the sub-pixel interpolation methods described above. The sub-pixel estimation seems closer to an integer value than to its true value. For example, if the histogram of the true offset is a uniform distribution between values a and b , then there are more estimated values around integers than around the midpoint between integers. This systematic error is believed to be caused by two factors. First, only 3×3 correlation values are used in the calculation. Such low sampling frequency of the correlation surface introduces systemic error. Second, the fitting function does not properly reflect the property of the correlation function. For example, the correlation function should be a symmetric function at the peak position. But the fitting functions we used do not have a symmetric property. Although the systematic error is very small, it is necessary to investigate this further and improve it.

To calculate each cross-correlation value, the number of computations is $3MN$. Assume the searching window size is K by L , then there will be $(K-M+1)(L-N+1)$ matching windows and the total calculation will be $3MN(K-M+1)(L-N+1)$. If the initial position of matched point is well estimated, search window will be only 2 or 3 pixels larger than template window. In our data processing, we use state vector and surface elevation to estimate the initial position of matched points. Since the RADARSAT-1 InSAR orbit data and elevation are relatively good, the search window size of $(7+M) \times (10+N)$ is used. The search window size does not affect the accuracy of matching, as long as the search window contains the true matched position. To increase speed, we

can reduce the searching window size to a confident range using position estimation from state vectors.

The template window size is determined by radar sensor parameters, such as pixel spacing in the range and azimuth directions. For standard beams, we use a window of size 60 pixels in the range direction and 200 pixels in the azimuth direction. Larger template size results in high correlation, but the correlation surface may become less sharp and large error in sub-pixel interpolation may be introduced. Smaller template window size causes large variations in the correlation surface. Noise effects may lead to a wrong matching position.

Magnitude based matching methods are easy to implement, and can be fast if implemented in the frequency domain. The disadvantage is that we do not use the phase information, which is very helpful for images with low contrast. Gabriel and Goldstein (1988) described a more accurate method based on the notion that the quality of interferogram fringes is highest when two images are correctly aligned. We first create an interferogram using two small patches from two images by conjugate multiplication of the two complex image grids. To evaluate the quality of the interferogram, we generate the fast Fourier Transform (FFT) of the interferogram, yielding a two-dimensional fringe spectrum. The power peak position of the spectrum represents the two spatial frequencies in the range and azimuth directions at which the brightest fringes appear. The relative quality of these brightest fringes is evaluated by computing the signal-to-noise ratio (SNR) of the spectrum by dividing the maximum power by the sum of all other powers. We store the quality associated with the window in the second image. Like cross-correlation, we move the window to a new position and calculate the quality again.

Among all these windows, we find one that has the highest quality. Along with eight quality values of its neighbor windows, sub-pixel offsets are calculated using the methods described above. This method has the same computational complexity as cross-correlation. However, since it uses phase information, it is more reliable and accurate than cross-correlation in areas where the image has low contrast.

3.3 Velocity calibration

The measured range and azimuth offsets must be calibrated to calculate the surface velocity. The measured range offsets, like measured phases from the interferogram, are related to baseline, topography, and surface motion. We have to remove the baseline and topography effects. Azimuth offsets are also affected by baseline and topography. We will discuss next the models used to calculate surface velocity (Gray and others, 1998; Michel and others, 1999).

Gray and others (1998) use a parallel ray method to derive the surface velocity. Assume the radar ray of the first pass is parallel to the ray of the second pass, then the geometry of the observation is shown in Figure 3.3. Based on the geometry, the range offset δr has two components: parallel baseline component B_p at the satellite end and the motion component δ_{motion} at the ground end given by

$$B_p = B \cos(\mathbf{c} - \mathbf{a}) \quad (3.17)$$

$$\mathbf{d}_{motion} = D_r \sin(\mathbf{q} + S_r) \quad (3.18)$$

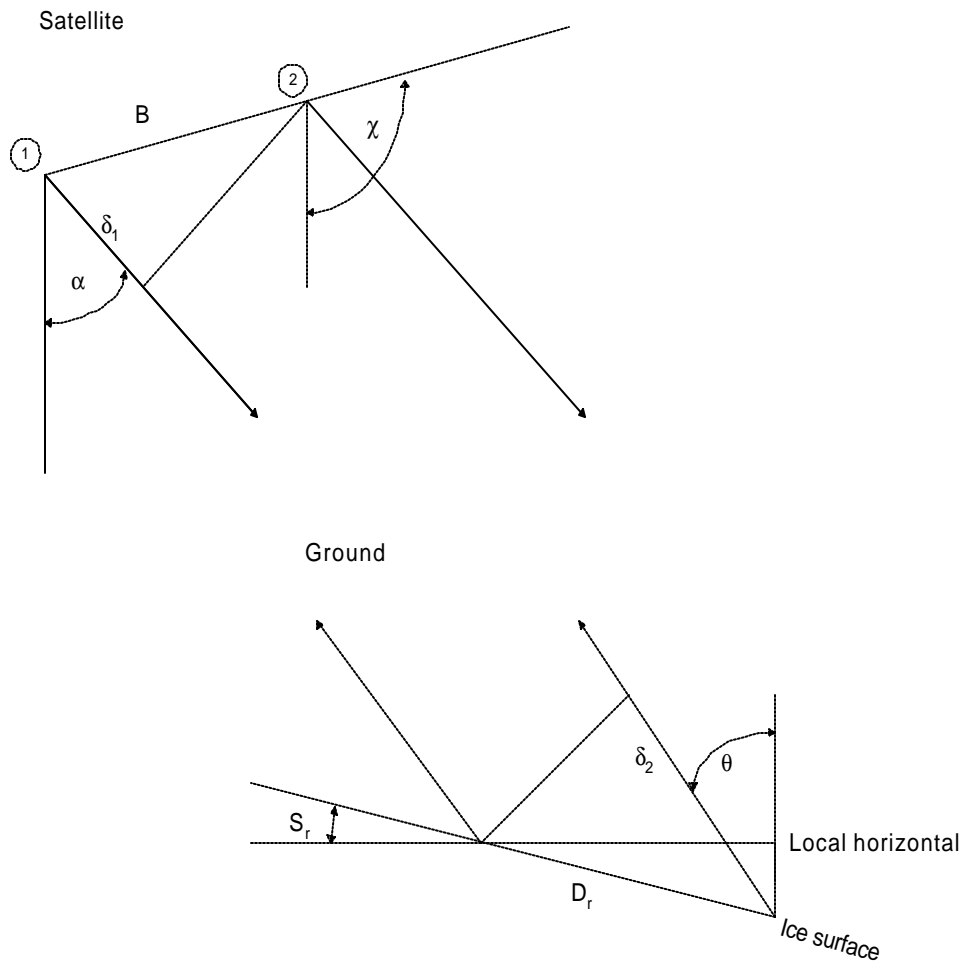


Figure 3.3: Geometry configuration of InSAR pair under parallel ray assumption. D_r is ground range displacement. B is the baseline, χ is the baseline angle, α is the radar look angle at the satellite, S_r and S_a are the terrain slopes in range and azimuth, respectively (to the local horizontal), θ is the local incidence angle and $\delta_r = \delta_1 + \delta_2$. (From Gray and others, 1998)

Azimuth offset is considered as the effect of the motion of the surface under the assumption that images are deskewed to zero Doppler and the two orbits are parallel. By combining all of the above, the range and azimuth offsets can be expressed as (Gray and others, 1998)

$$\mathbf{d}_r = B \cos(\mathbf{c} - \mathbf{a}) + D_r \sin(\mathbf{q} + S_r) \quad (3.19)$$

$$\mathbf{d}_a = D_a \cos(S_a) \quad (3.20)$$

Whence

$$D_r = \frac{\mathbf{d}_r - B \cos(\mathbf{c} - \mathbf{a})}{\sin(\mathbf{q} + S_r)} \quad (3.21)$$

$$D_a = \frac{\mathbf{d}_a}{\cos(S_a)} \quad (3.22)$$

Here \mathbf{d}_r is the slant range pixel shift in meters, \mathbf{d}_a is the azimuth direction pixel shift in meters, D_r is the surface ground range displacement, D_a is the surface displacement in the azimuth direction, S_r is the terrain slope in the range direction to the local horizontal, S_a is the terrain slope in the azimuth direction to the local horizontal, \mathbf{c} is the baseline angle, \mathbf{a} is the radar look angle, \mathbf{q} is the local incidence angle, and B is the baseline.

Errors in D_r and D_a are estimated as (Jezek 1999b)

$$\begin{aligned} dD_r^2 = & \left(\frac{1}{\sin(\mathbf{q} + S_r)} d\mathbf{d}_r \right)^2 + \left(\frac{B \sin(\mathbf{c} - \mathbf{a})}{\sin(\mathbf{q} + S_r)} d\mathbf{c} \right)^2 + \left(\frac{B \sin(\mathbf{c} - \mathbf{a})}{\sin(\mathbf{q} + S_r)} d\mathbf{a} \right)^2 \\ & + \left(\frac{[B \cos(\mathbf{c} - \mathbf{a}) - \mathbf{d}_r] \cos(\mathbf{q} + S_r)}{\sin^2(\mathbf{q} + S_r)} d\mathbf{q} \right)^2 \\ & + \left(\frac{[B \cos(\mathbf{c} - \mathbf{a}) - \mathbf{d}_r] \cos(\mathbf{q} + S_r)}{\sin^2(\mathbf{q} + S_r)} dS_r \right)^2 + \left(\frac{\cos(\mathbf{c} - \mathbf{a})}{\sin(\mathbf{q} + S_r)} dB \right)^2 \quad (3.23) \end{aligned}$$

$$dD_a^2 = \left(\frac{1}{\cos(S_a)} d\mathbf{d}_a \right)^2 + \left(\frac{\mathbf{d}_a \sin(S_a)}{\cos^2(S_a)} d S_a \right)^2 \quad (3.24)$$

In Equation 3.23, the baseline effect on D_r is through B and angle χ . The topography effect is through the look angle α and incidence angle θ . According to the cosine law, a ground point (X, Y, Z) in Earth Centered Inertial (ECI) coordinates will have a look angle α and incidence angle θ defined as

$$\alpha = \cos^{-1} \left(\frac{r_x^2 + h^2 - r_e^2}{2r_x h} \right) \quad (3.25)$$

$$\theta = \cos^{-1} \left(\frac{h^2 - r_x^2 - r_e^2}{2r_x r_e} \right) \quad (3.26)$$

where h is the satellite height (from satellite to the earth center), r_x is the range distance from satellite to the ground point, and r_e is the distance from the earth center to the ground point. That is

$$r_e = \sqrt{X^2 + Y^2 + Z^2} \quad (3.27)$$

Gray's model (Gray and others, 1998) ignores the effect of the topography on the azimuth offset. Since the satellite velocity vectors of two of the passes are not parallel, the angle, $\delta\alpha$, between the two vectors in the plane of the incidence yields a topography dependent azimuth offset δv that is expressed in pixel units as (Michel and others 1999)

$$\delta v = \frac{z \sin(\delta\alpha)}{R_z} [1 - \cos(\delta\alpha)] l + \delta v_0 + \mathbf{d}_{motion} \quad (3.28)$$

where z is surface elevation, R_z is azimuth pixel spacing, l is the line number with reference to the first line of the image, δv_0 is the constant azimuth offset, and δ_{motion} is the azimuth offset due to the surface motion. In the equation, the first term of the right side is the topography dependent azimuth offset. The second term produces an azimuth ramp in the offset field.

3.4 Velocity errors

The random error of velocity is from random error in speckle matching. Equation (3.16) gives the random error of the pixel offset as a function of coherence, matching window size, and an oversampling factor. As discussed in 3.2.3, the random error of speckle matching is about 2 m/year in the azimuth direction and about 6 m/year in the range direction for this research.

Systematic biases on velocity are from baseline error, calibration model error, and velocity control point error. The baseline error causes a constant term plus a small variation across the range in velocity error. The constant term can be removed by control points. The largest error in velocity is from velocity control points. The accuracy of the velocity control points, as well as their distribution, determines the velocity error. So the systematic bias could reach up to 8 m/year. As a result, the total error for azimuth direction is about 10 m/year and range direction about 20 m/year. This is consistent with other researchers (Gray and others, 1998; Michel and others, 1999; Jezek, 1999b).

3.5 Comparison between interferometry and speckle matching

We have discussed two techniques for surface motion estimation using InSAR data in Chapters 2 and 3. Each technique has its advantages and disadvantages. The interferometry technique provides only the range direction motion. Its accuracy is on the order of a wavelength. For high decorrelation areas, the phase may be destroyed and the interferometry technique may fail. The speckle matching technique estimates the range offset and azimuth offset and can produce two-dimensional surface velocity information. The accuracy for speckle matching is limited by the pixel size of the image and is larger than interferometry as shown in Table 3.1. Since range pixel size is larger than azimuth pixel size (for standard beams), and range offset is affected by baseline and topography, the range velocity is less accurate than azimuth velocity. Table 3.1 summarizes the comparison between interferometry and speckle matching techniques. The errors are taken from Section 2.4.2 for interferometry and from Section 3.5 for speckle matching.

	Interferometry	Speckle Matching
Motion direction	Range (one pair)	Range & azimuth
Velocity accuracy	4 m/year	Range: 20 m/year Azimuth: 10 m/year
Best apply areas	Slow motion	Fast motion

Table 3.1: Comparison between interferometry and speckle matching techniques

Based on the comparison, it is desirable to combine both techniques in surface velocity estimation from a single InSAR pair. We use the range motion from interferometry and the azimuth motion from speckle matching to produce two-dimensional surface velocity with the best possible accuracy.

CHAPTER 4

IMPROVING INTERFEROMETRIC SAR COHERENCE BY DELAUNAY TRIANGULATION BASED CO-REGISTRATION

4.1 Introduction

A complex interferogram is formed by conjugate multiplication of two SAR images from two separate SAR observations over the same ground area. Coherence or correlation of two SAR images is the normalized, local average of the interferogram magnitude. Unlike radar reflectivity measurements, which are mainly determined by the statistics of the surface height and slope distribution, coherence measurements are related to the total change in the distribution of affected scatters (Zebker and others, 1995). So coherence provides an effective measure of surface change (Rignot and others, 1993), as well as more quantitative measures including penetration depths on the Greenland Ice Sheet (Hoen and others, 2001) and forested area classification (Hagberg and others, 1995).

Decorrelation is the product of spatial decorrelation, temporal decorrelation, and thermal decorrelation (Zebker and Villasenor, 1992). Joughin (1995) further analyzed six sources of decorrelation: thermal, registration, baseline, volume, mismatch, and temporal decorrelations. Some of these terms are related to physical properties of the surface and

some are related to instrument distortion, viewing geometry, and analysis techniques. We seek to minimize decorrelation so as to emphasize science information. Among the sources of decorrelation, co-registration decorrelation can be a problem when there are strong spatial variations in surface displacement. This situation is common across the polar ice sheets where surface speeds may change 10 fold or more over distances of 100 km. The co-registration of two SAR images is achieved by two steps: first, calculate the pixel offset for discrete tie points using a matching method; and second, calculate pixel offset for every pixel using an interpolation model based on the matched tie points. The first step can achieve excellent subpixel accuracy (Gabriel and Goldstein, 1988; Gray and others, 1998; Joughin, 1995; Michel and others, 1999; Small and others, 1993). Techniques include magnitude-based cross-correlation matching, phase or fringe-based matching, oversampling, and sub-pixel interpolation. Tie point accuracy varies from 1/10 pixel to 1/40 pixel. Such matching accuracy is not critical for co-registration decorrelation because correlation is not sensitive to pixel offset error within 1/10 pixel (Hagberg and others, 1995; Joughin, 1995). The critical part, which influences co-registration decorrelation, is the second step: tie point interpolation. In this chapter, we present a new approach that deals with the less studied problem.

The traditional co-registration method uses interpolation based on affine transformation to interpolate range and azimuth offsets for every pixel of the SAR image based on matched tie points. Affine transformation accounts only for translation, rotation, scaling, and shearing of the image, but not for non-linear image changes associated with spatial variations in the surface displacement field. To solve this problem, Fatland and others (1998) used a local bilinear interpolation resampling method to co-register two

SAR images. Bilinear interpolation requires that the data are distributed on a regular grid. For RADARSAT-1 InSAR data over the fast moving East Antarctic Ice Streams, severe temporal decorrelation on some areas such as shear margins results in removal of tie points. Consequently the data are no longer regularly gridded and the bilinear interpolation method is not applicable directly. In this case, Delaunay triangulation based interpolation is used to interpolate the irregular data set. The purpose of this chapter is first, to review theoretical background on how co-registration errors affect decorrelation, and how interpolation methods affect decorrelation for different applications. We then introduce a Delaunay triangulation based local co-registration method. Results from affine transformation co-registration and Delaunay triangulation co-registration are compared and discussed in details. Last, we present a coherence mosaic of the East Antarctic Ice Streams generated using the new co-registration method.

4.2 Co-registration decorrelation of interferometric SAR

Theoretical background

We are interested in co-registration decorrelation caused by co-registration errors between two SAR images. In this section, derivation of co-registration decorrelation is provided. Unlike similar derivations in Hagberg and others (1995) and Joughin (1995), the work in this section is restricted to co-registration decorrelation in the range and azimuth directions.

We define a ground coordinate system (x,y,z) , where x is the along track direction, z is the surface normal direction and y is the direction of a cross product of z

and x . The slant range image coordinate is (r,x) , where r is a function of y and z . The complex signal amplitude is expressed as

$$s_1(r_0, x_0) = \iiint f(x,y,z)e^{-j2k\eta}Wr(r_1 - r_0)Wx(x - x_0)dxdydz \quad (4.1)$$

where $f(x,y,z)$ is terrain reflectivity. Wr and Wx are system impulse response functions in the range and azimuth directions. We assume that the system impulse response function is separable in range and azimuth directions. $r_0=r_0(y,z)$, $r_1=r_1(y,z)$ are ranges from the satellite to the target in the first and second passes.

Assume there is no temporal change in reflectivity for the second observation, and system impulse responses for the second observation are the same as for the first observation. So the radar scatter from the registered image position of the second image with registration error δr in the range direction and δx in the azimuth direction is

$$s_2(r_0 + \Delta + \mathbf{d}_r, x_0 + \mathbf{d}_x) = \iiint f(x,y,z)e^{-j2kr_2}Wr(r - (r_0 + \Delta \mathbf{d}_r))Wx(x - (x_0 + \mathbf{d}_x))dxdydz \quad (4.2)$$

To calculate the correlation of (4.1) and (4.2), we assume that scatters in a resolution cell volume are uniformly distributed and uncorrelated. Under the spatial white noise assumption, the correlation of (4.1) and (4.2) is expressed as (Joughin, 1995)

$$\left\langle s_1(r_0, x_0)s_2^*(r_0 + \Delta + \mathbf{d}_r, x_0 + \mathbf{d}_x) \right\rangle = \iiint \sigma(x,y,z)e^{j2k(r_2 - r_1)} W(r - r_0, x - x_0)W^*(r - (r_0 + \Delta \mathbf{d}_r), x - (x_0 + \mathbf{d}_x))dxdydz \quad (4.3)$$

where $\sigma(x,y,z)$ is a normalized cross section coefficient defined in

$$\langle f(x, y, z) f^*(x', y', z') \rangle = \mathbf{s}(x, y, z) \cdot \mathbf{d}(x - x', y - y', z - z') \quad (4.4)$$

To simplify Equation (4.3), we assume the cross section coefficient $\sigma(x,y,z)$ is only a function of variable z . We also replace r_2-r_1 with its approximation (Hagberg and others, 1995)

$$r_2 - r_1 = r_2(y', z') - r_1(y, z) = Bp + \frac{Bn}{r} [(y' - y) \cos \mathbf{q} + (z - z') \sin \mathbf{q}] \quad (4.5)$$

where r is the average of range r_1 and r_2 , and θ is the average of look angles for two observations. Through variable substitution, Equation (4.3) becomes

$$\begin{aligned} \left\langle s_1(r, x) s_2^*(r + \Delta + \mathbf{dr}, x + \mathbf{dx}) \right\rangle &= \frac{e^{j2k\Delta}}{\sin \mathbf{q}} \cdot \int \mathbf{s}(z) e^{\frac{-j2kBn}{r \sin \mathbf{q}} z} dz \cdot \\ &\int W_r(\mathbf{b}) W_r^*(\mathbf{b} - \mathbf{dr}) e^{\frac{-j2kBn}{r \tan \mathbf{q}} \mathbf{b} \cdot \mathbf{dr}} d\mathbf{b} \cdot \int W_x(\mathbf{g}) W_x^*(\mathbf{g} - \mathbf{dx}) d\mathbf{g} \end{aligned} \quad (4.6)$$

The correlation in Equation (4.6) is a product of four terms. The first term is a constant. The second term is an integral with depth. The third term is the integral of the range impulse response function and related to the range offset error δr . The fourth term is an integral of the azimuth impulse response function and is related to the azimuth offset error δx . The effect of the range offset error and the azimuth offset are separated.

So the normalized co-registration decorrelation in range direction \mathbf{R}_r and co-registration decorrelation in azimuth direction \mathbf{R}_x are written as

$$\mathbf{R}_r(\mathbf{dr}) = \frac{\left\langle s_1(r,x)s_2^*(r+\Delta+\mathbf{dr},x) \right\rangle}{\left\langle s_1(r,x)s_2^*(r+\Delta,x) \right\rangle} = \frac{\int W_r(\mathbf{b}) \cdot W_r^*(\mathbf{b}-\mathbf{dr}) e^{-j \frac{2kBn}{r \tan \mathbf{q}} \mathbf{b}} d\mathbf{b}}{\int W_r(\mathbf{b}) \cdot W_r^*(\mathbf{b}) e^{-j \frac{2kBn}{r \tan \mathbf{q}} \mathbf{b}} d\mathbf{b}} \quad (4.7)$$

$$\mathbf{R}_x(\mathbf{dx}) = \frac{\left\langle s_1(r,x)s_2^*(r+\Delta,x+\mathbf{dx}) \right\rangle}{\left\langle s_1(r,x)s_2^*(r+\Delta,x) \right\rangle} = \frac{\int W_x(\mathbf{g}) W_x^*(\mathbf{g}-\mathbf{dx}) d\mathbf{g}}{\int W_x(\mathbf{g}) W_x^*(\mathbf{g}) d\mathbf{g}} \quad (4.8)$$

Both co-registration decorrelations are related to the SAR system's imaging response function W_r and W_x . In Vexcel's SAR processor system, a Kaiser window with Kaiser parameter $\beta=2.4$ is used. Using typical RADARSAT InSAR data parameters, the range co-registration decorrelation (Equation 4.7) and azimuth co-registration decorrelation (Equation 4.8), as a function of co-registration error in pixels in the range and azimuth directions are plotted in Figure 4.1.

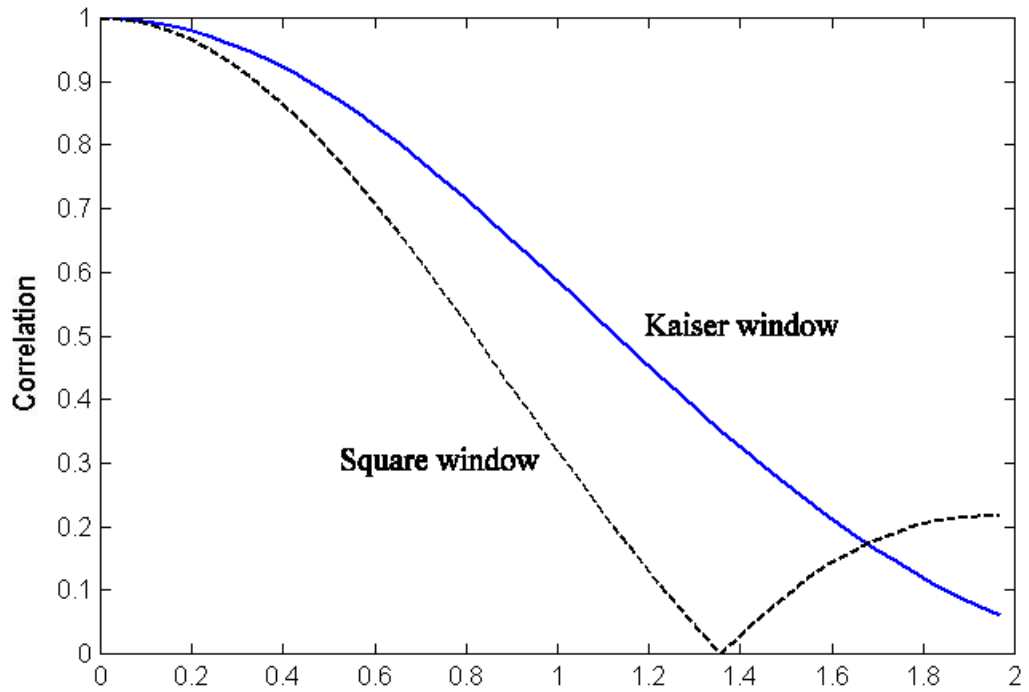
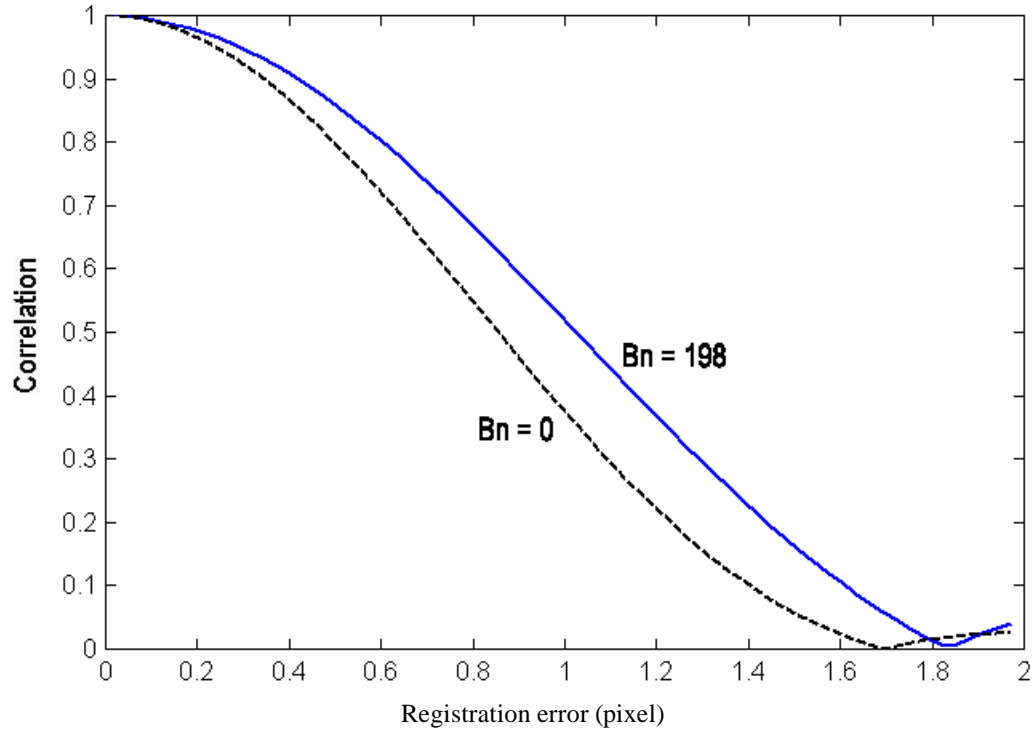


Figure 4.1. Theoretical registration decorrelation coefficient curves. (a) in range direction, (b) in azimuth direction. We use typical RADARSAT parameters. Range bandwidth is 11.6 MHz. Doppler bandwidth is 900 Hz. Range spacing is 7.5 m and azimuth spacing is 8.117 m. $R=914$ km, $\theta=27.5^\circ$, $\lambda=5.66$ cm, $B_n=200$ m. Weight function is Kaiser window with $\beta=2.4$ and Square window.

Figure 4.1(a) uses a Kaiser window with $\beta=2.4$. The dashed line is for baseline $B_n=0$ and the solid line is for baseline $B_n=198\text{m}$. From Equation (4.7) it is known that the co-registration decorrelation in the range direction is also a function of the baseline B_n . Figure 4.1(a) shows that decorrelation for co-registration errors is less sensitive and drops slowly for larger baselines than for smaller baselines. This does not mean that the total correlation is larger for large baselines.

Figure 4.1(b) shows co-registration decorrelation in the azimuth direction. The dashed line is for a square window and the solid line for a Kaiser window. For the Kaiser window, the decorrelation is less sensitive to the co-registration error. The curves indicate that the co-registration decorrelation in both direction drops slowly when the co-registration error is within a half pixel. For instance, if the co-registration error is $1/20$ pixel in both directions, the registration coefficient will be $0.9985*0.9987=0.9972$. When the co-registration error is larger than a half pixel, both coefficients drop significantly. For co-registration error in both directions larger than 1 pixel, the total co-registration coefficient will be below 0.30.

Affine transformation based co-registration

We have discussed the InSAR decorrelation due to co-registration errors. Now we investigate errors introduced by co-registration algorithms. The affine transformation is the most commonly used method to co-register two SAR images. First, the tie point pairs are generated using a phase or magnitude based matching method with sub-pixel accuracy. Then linear transformations are used to fit the range and azimuth offsets. The range offset dx and azimuth offset dy are expressed as

$$dx=a_0+a_1x+a_2y \quad (4.9)$$

$$dy=b_0+b_1x+b_2y \quad (4.10)$$

where a_0 , a_1 , a_2 , b_0 , b_1 , and b_2 are affine transformation coefficients, x and y are image positions. Equation (4.9) represents a plane for range offset over the reference SAR image coordinates (x, y) . Equation (4.10) represents a plane for azimuth offset over the reference SAR image coordinates (x, y) . The six parameters can be solved using a least-squares adjustment method, based on the N tie points. The overall accuracy of affine transformation depends on the tie point accuracy, the number of tie points, distribution of tie points, and the suitability of a linear transformation model. The suitability of a linear transformation model will be discussed in the following section.

Stationary surface

In the range direction, the range offset results from baseline and elevation (assume no motion). The baseline effect on the range offset over a flat surface is nearly linear (Joughin, 1995). Topography introduces non-linear range offsets. The topography effect on the range offset in pixels can be approximated by (Joughin, 1995)

$$\Delta X_z \approx \Delta_{x_0} + \frac{1}{Rx} \frac{-Bn}{R \sin \theta_0} z \quad (4.11)$$

where Δ_{x_0} is the constant offset. Rx is the range pixel spacing, Bn is the perpendicular baseline, R is the distance from the satellite to the target, θ_0 is the incidence angle at the scene center, z is the elevation. In the azimuth direction, the azimuth offset shift Δy between two image pixels of the same stationary target is due to non-parallel orbits

(crossed orbit) (Gabriel and Goldstein, 1988). Michel and others (1999) derived the azimuth offset related to the satellite flight height change, which includes an elevation dependent term and a linear term with respect to azimuth position. We consider more general cases where there is a parallel baseline change along the flight track. Assume that the two SAR images are deskewed to zero Doppler. So the azimuth offset can be written as

$$\Delta y = \Delta y_0 + \frac{\sin \beta}{R_y} r + [1 - \cos \alpha] x + \frac{\sin \alpha}{R_y} z \quad (4.12)$$

where R_y is the azimuth pixel spacing, r and x are image coordinates in range and azimuth directions, Δy_0 is constant azimuth offset, α is the angle between two satellite velocity vectors in the vertical plane, β is the angle between two satellite velocity vectors in the plane of the look direction and the velocity vector of the first satellite, and z is elevation. Since angles α and β are almost constant for a frame of 100/km, Equation (4.12) is considered a constant term plus two linear terms with respect to image coordinates and an elevation dependent term. The last term is non-linear with respect to image position.

Based on the above analysis, we conclude that for areas where there is no motion occurring, the affine transformation model can approximate the range offset with an error better than 0.1 pixel and an azimuth offset with an error better than 0.01 pixel. Using Figure 4.1, the total co-registration decorrelation is 0.99 for such an error bound. Thus, there is no significant co-registration decorrelation for an affine transformation where there is no motion.

With surface motion

The Antarctic ice sheet surface is in motion and the motion may be spatially complex. For example, differential motion across the ice streams shear margins reaches a kilometer per year, corresponding to offset differences of tens of pixels in SAR images. Therefore, affine transformation mapping between the two images may result in misregistration. The coherence will vary depending on the distribution of control points. If the control points are across all areas, the transformation attempts to fit everywhere and eventually has a larger error and low coherence. If control points reside on only a portion of the image where local relative motion is small, then the area will be well fit by the affine transformation, resulting in good coherence. But other than this area in the image, the decorrelation will be high. This piece-by-piece procedure has been used to calculate velocity in specific regions.

Researchers have employed affine transformation based co-registration in glacier applications. However, these applications have either a shorter temporal baseline or lower surface motion so the co-registration decorrelation problem is not so serious. In some applications, one portion of an image area, such as the glacier interior, is of particular interest, so the tie points are selected in this area to guarantee good coherence in this area and ignore the decorrelation of other areas. Considering applications with longer temporal baseline and fast moving surfaces (e.g., RADARSAT InSAR over the Antarctic), we intend to achieve good coherence across the whole image. A Delaunay triangulation based local transformation can accomplish this goal.

4.3 Delaunay triangulation based co-registration

Delaunay triangulation based co-registration of two SAR images uses a standard technique of surface interpolation (Kao and others, 1991; Saalfeld, 1985). In SAR image co-registration, matched tie points are processed to eliminate noise or low quality tie points. This results in an irregular tie point distribution. For example, on the shear margin zone or low correlation area, removal of high noise points leaves larger holes in these areas. To interpolate any points, we need to determine (1) which points are nearby, and (2) how those nearby points should be weighted to produce the desired value. These are two issues to be discussed: Delaunay triangulation and interpolation in the triangle.

Delaunay triangulation

For a finite point set $\{ p_i=(x_i, y_i) \ i=1,\dots,N\}$ in the reference image, triangulation subdivides the image space into triangles. Among all triangulation types, Delaunay triangulation is a special type of triangulation and particularly suitable for interpolation (Kao and others, 1991, Barber and others, 1996). This is because Delaunay triangulation maximizes the minimum angle of all the angles that are present in the triangulation. Very small angles cause distortion problems because the interpolation is based on the distant vertex values. Delaunay triangulation avoids triangles with extremely small angles. This angle relationship keeps each angle vertex reasonably distant from the triangle side opposite that vertex. Slight perturbations of vertices of Delaunay triangulation rarely result in a vertex moving across the opposite edge, an operation called “triangle folding.”

Delaunay triangulation is unique for a point set, if there are no four points co-circular (four points on the same circle). For any triangle in Delaunay triangulation, there are no points inside its circumcircle (a circle that passes the three vertices of the triangle). This is called the empty circumcircle property. It is a Delaunay triangulation's necessary and sufficient condition. So Delaunay triangulation can be built by locally verifying the empty circumcircle property. If there is a violation of this property, for example, point p_4 is inside the triangle of vertices p_1, p_2, p_3 as shown in Figure 4.2(a), then the edge is switched from p_2p_3 to p_1p_4 . The new triangles as shown in Figure 4.2(b) obey the empty circumcircle property. If there is not any violation of the circumcircle property for any triangle, a Delaunay triangulation is generated.

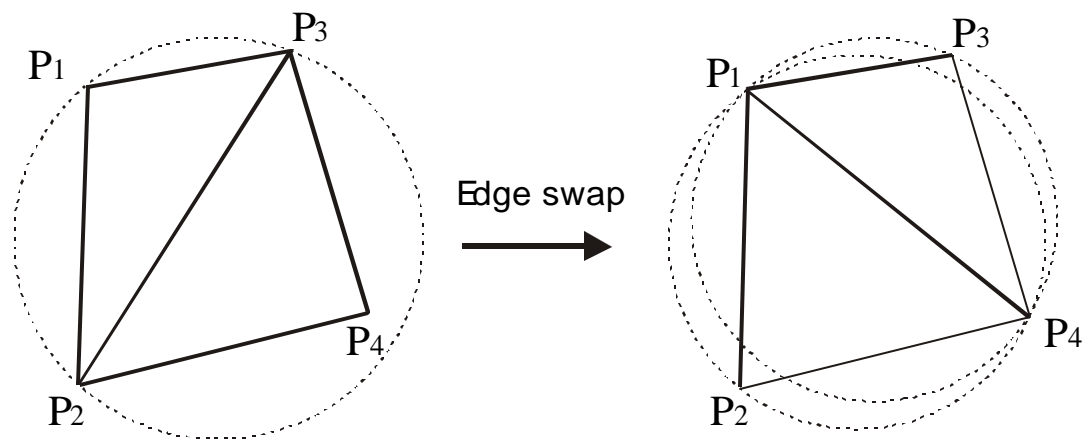


Figure 4.2. Swap test of empty circumcircle property. Left: P_4 is inside the circumcircle.

Right: after edge swap, no points are in circumcircle.

A simple implementation for Delaunay triangulation is an incremental algorithm, which builds Delaunay triangulation by inserting points, one point at a time (Kao and others, 1993). At any stage of insertion, assume the current inserted points are already triangulated as a Delaunay triangulation. When a new point is inserted, first find a triangle inside which the point is located. The newly inserted point, with the three points of the triangle, can form three new triangles. Use the swap test locally to update triangles to satisfy the empty circumcircle property. If the newly inserted point is outside the convex hull of the current point set, then new triangles are formed between the newly inserted points and all visible points on the convex hull of the current point set. The swap test is also applied to update triangles to satisfy the empty circumcircle property. The insertion of points is in random order. The order of insertion does not affect the final result.

Local interpolation

Once a point set $\{ p_i=(x_i, y_i) \ i=1,\dots,N\}$ in the reference image is Delaunay triangulated, we want to interpolate the range offset and azimuth offset for any points inside the triangle using the offsets of the three vertices. This is similar to the process of converting a digital elevation model from Triangle Irregular Network (TIN) to regular grid. The interpolation methods could be nearest point, cubic, or linear interpolation. Nearest point interpolation does not produce a smooth and accurate estimation, especially when the triangle is large. Cubic interpolation involves complicated computations and the interpolation does not honor tie points. Linear interpolation is used inside a triangle for SAR image co-registration.

Assume a triangle has three vertices $p_1=(x_1,y_1)$, $p_2=(x_2,y_2)$, and $p_3=(x_3,y_3)$. A point $p=(x,y)$ is inside the triangle. Then p can be expressed uniquely as a linear combination of the three points:

$$p = \alpha_1 \cdot p_1 + \alpha_2 \cdot p_2 + \alpha_3 \cdot p_3 \quad (4.13)$$

where $\alpha_1+\alpha_2+\alpha_3=1$; and α_1 , α_2 , and α_3 are non-negative. α_1 , α_2 , and α_3 are called convex coordinates or barycentric coordinates of p . They are defined by the area ratio shown in Figure 4.3 (Saalfeld, 1985):

$$\alpha_i = \text{Area}(\Delta p p_k p_m) / \text{Area}(\Delta p_1 p_2 p_3) \quad k, m \neq i \quad (4.14)$$

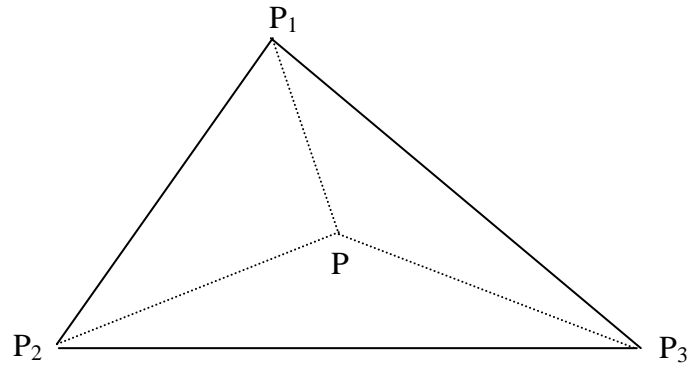


Figure 4.3. Interpolation inside a triangle

Assume the range offsets at the three vertices p_1 , p_2 , p_3 of a triangle are dx_1 , dx_2 , dx_3 respectively. Azimuth offsets are dy_1 , dy_2 , dy_3 , respectively. Then the range offset dx and azimuth offset dy at the point p can be written as

$$dx = \alpha_1 dx_1 + \alpha_2 dx_2 + \alpha_3 dx_3 \quad (4.15)$$

$$dy = \alpha_1 dy_1 + \alpha_2 dy_2 + \alpha_3 dy_3 \quad (4.16)$$

The three coefficients α_1 , α_2 , and α_3 are dependent on the point $p=(x,y)$. So we have to calculate them for every point. Saalfeld (1985) proposed a fast way to calculate the three coefficients.

The triangle based local linear fitting of range and azimuth offsets provides smooth and continuous offsets (the first derivative is not continuous). Every point is determined by only local points, which are the three points of a triangle. If a point is on the edge of the triangle, one coefficient will be 0. If a point is on the tie point, then one coefficient is 1 and other two are 0. In implementation, an algorithm that quickly locates triangles is required.

Analysis of registration error

Assume the tie point matching has an error σ_x in range direction and σ_y in azimuth direction. Then the error of the range offset at a point inside a triangle can be estimated as

$$\sigma_{dx}^2 = \alpha_1^2 \sigma_x^2 + \alpha_2^2 \sigma_x^2 + \alpha_3^2 \sigma_x^2 \quad (4.17)$$

Since $0 \leq \alpha_i \leq 1$ and $\alpha_1 + \alpha_2 + \alpha_3 = 1$, (4.17) becomes

$$\sigma_{dx}^2 \leq 3\sigma_x^2 \quad (4.18)$$

Similarly, the error of azimuth offset at point p is

$$\sigma_{dy}^2 \leq 3\sigma_y^2 \quad (4.19)$$

It makes sense that the error at point p is the same as the error of the vertices. The position of point p is bounded by the three vertices of a triangle. So the errors of range and azimuth offsets for this point are also bounded by the errors of range and azimuth offsets for the three vertices. This is based on the assumption that control points are well

distributed, such that every triangle has almost linear variation. If a triangle is too large and there is a large variation of surface motion in side a triangle, then we must densify the control points. In this research, tie points are selected in about 1 km spacing.

4.4 Example and Application

Study area

An InSAR pair over Recovery Glacier was selected for testing the co-registration methods. The InSAR pair 5527 from orbit 9851 and orbit 10194 was acquired on September/October 1997 during the Antarctic Mapping Mission I (AMM-1). Figure 4.4 shows the location of the frame and its slant range intensity image. In this frame, the ice funnels into Recovery Glacier. The ice velocity along the center line starts from 110 m/year at the upper left corner that increases to 180 m/year at the right lower corner. The shear margin aligns vertically in the right portion of the frame. Across the shear margin, the azimuth offset varies significantly.

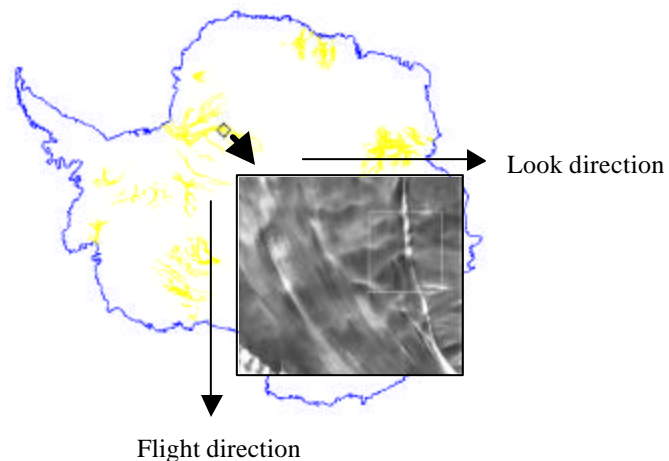


Figure 4.4. Location of example data

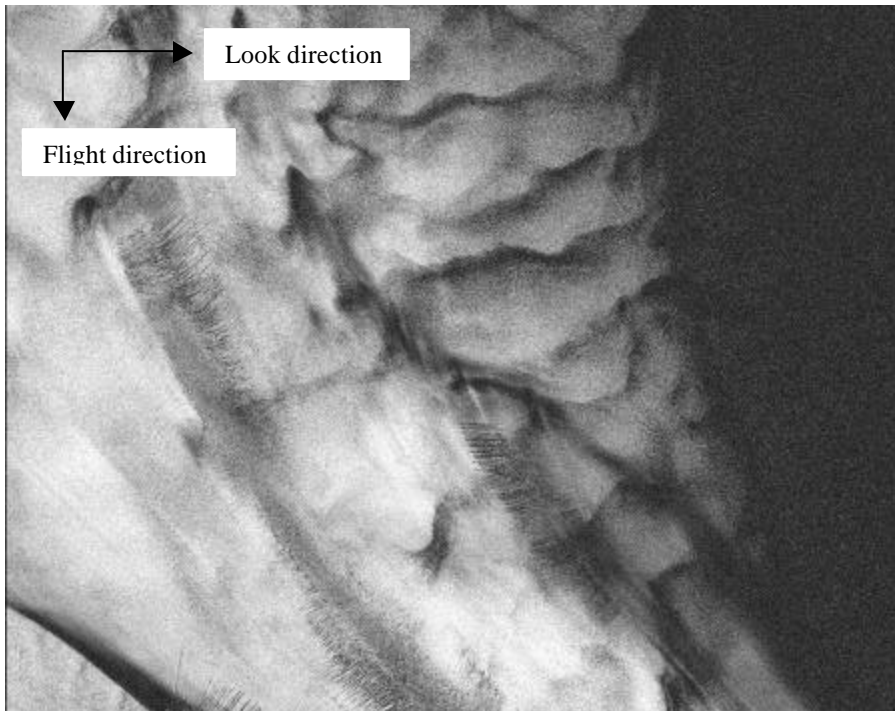
Data processing

For the above InSAR frame, we created interferograms using two co-registration methods. One is the traditional affine transformation based co-registration method and the other is the Delaunay triangulation based co-registration method. We compare the results produced by the different methods.

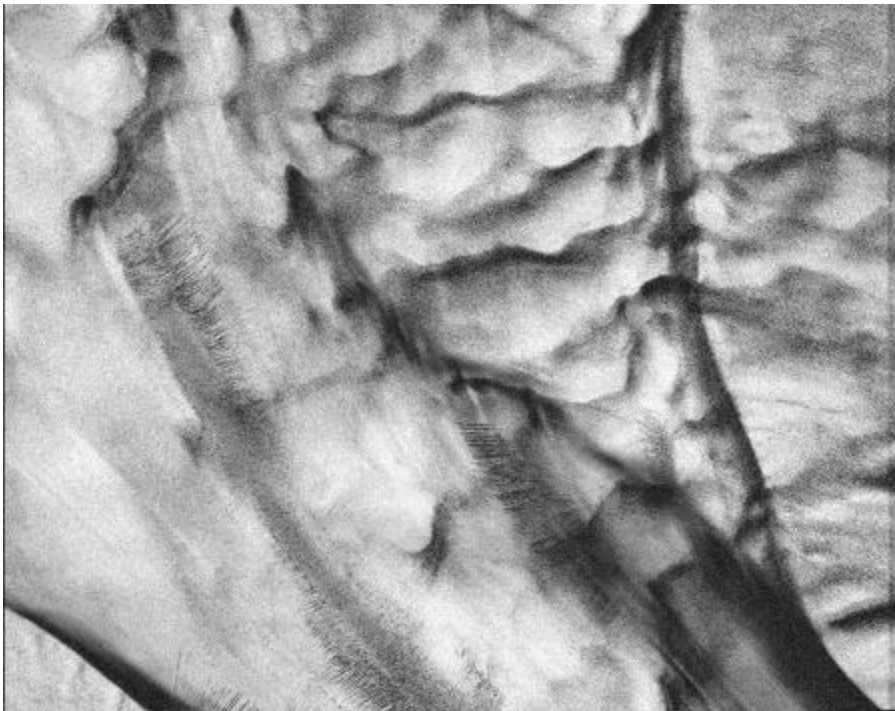
Affine transformation based co-registration is performed by first matching tie points, then using a least squares adjustment to calculate the parameters of Equation (4.9) and (4.10), which represent two surfaces of offsets in the range and azimuth directions. The affine transformation parameters are used to resample the secondary SLC image into the same geometry as the reference SLC image. Then the interferogram is created by conjugate multiplication of the reference SLC with the resampled SLC. The coherence image result is shown in Figure 4.5 (a).

The Delaunay triangulation based co-registration involves more steps. First, we match tie points between the reference SLC image and the secondary SLC image. The tie points in the reference SLC are selected as regular grid points with a range spacing of 60 pixels and an azimuth spacing of 200 pixels. Speckle matching (Gray and others, 1998) is used to find the sub-pixel offset in the range and azimuth direction in the secondary SLC image. Second, we preprocess the tie points based on the matching quality and spatial distribution. An interactive process is used to eliminate bad points based on the histogram and values of neighbors. A low-pass filter is also applied to smooth the offset shift for tie points. After this process, the tie points may no longer be regular grids because some bad tie points are deleted. Third, we use MATLAB function (GRIDDATA) based on

Delaunay triangulation to create range offset and azimuth offset maps in an evenly spaced grid. Fourth, the resampled SLC of the second image is created based on the range and azimuth offset maps. Last, the interferogram is created by conjugate multiplication of the reference SLC and resampled SLC. The coherence image result is shown in Figure 4.5 (b).



(a)



(b)

Figure 4.5. Comparison of coherence images of the two registration methods

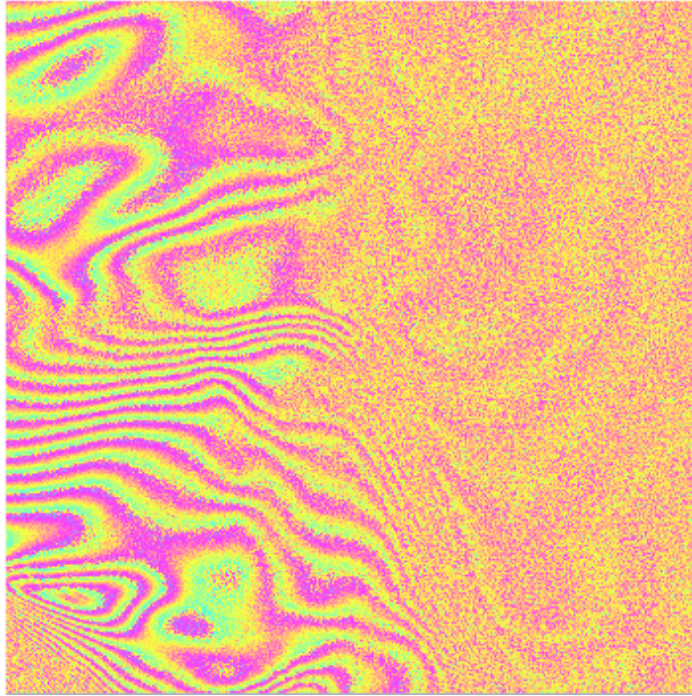
Coherence and interferogram comparison

Figure 4.5 is a comparison of the coherence images generated using (a) affine transformation registration and (b) using Delaunay triangulation registration. The main portion of the image shows the glacier moving from the top to the bottom and turning slightly right when close to the bottom right. A shear margin running up and down on the left side of the image divides the image into a fast-moving and a slow-moving portions in the azimuth direction. In this case, the affine transformation fails to accurately fit the surface offset in the azimuth direction across the entire image. As a result, the affine transformation fits well in the left lower portion of the image, but yields large co-registration error in the upper right portion. The co-registration error in the azimuth direction is more than 1 pixel in some areas. Due to the high co-registration decorrelation, there are problems with this coherence image: the right side of the shear margin, the unwrapped phase is lost when calculating velocity; physical properties are obscured by the co-registration decorrelation. Shear margin and fine structures related to subglacial topography are not shown in the coherence image.

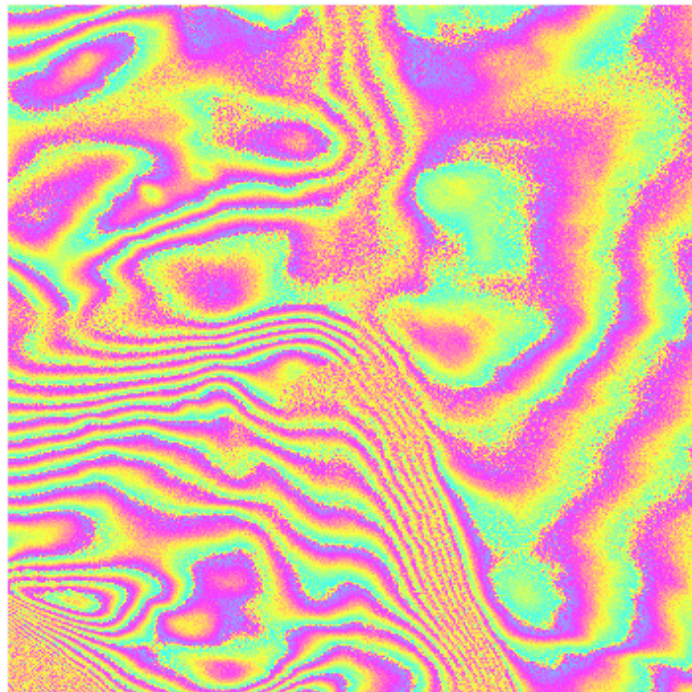
Figure 4.5(b) is the coherence generated from the Delaunay triangulation based co-registration. Local variations of surface offsets are well captured. Because the co-registration decorrelation is minimized, the entire coherence image has good coherence quality and is imprinted by features related to surface properties. All problems mentioned above are solved. The shear margins with intense ice crevassing in the left bottom corner and the right side of the image are clearly depicted, with high contrast to other regions. There is differential motion in the interior of the glacier from the center of the image to

the right lower corner of the image. Long wavelength linear features ($>30/\text{km}$) with left right orientation in the upper left portion of the image are related to the bed topography. Some of them extend across the shear margin to the slow-moving ice sheet. Several crevasse belts along the flow direction are clearly visible in the coherence image. Individual crevasses perpendicular to the flow direction are clearly visible. This image demonstrates that the new method significantly improves coherence and is very helpful in the analysis of surface physical properties.

Figure 4.6 shows two interferogram clips of the same region in the right upper corner of the frame marked in Figure 4.4. Figure 4.6(a) is generated by affine transformation co-registration, and Figure 4.6(b) is generated by Delaunay triangulation based co-registration. Both interferograms are multi look 2×8 averaged, spherical phase removed. Fringes in Figure 4.6(a) have a lot of noise. In the right half of Figure 4.6(a), fringes are completely invisible. In Figure 4.6(b), fringes are clearly visible, even in the shear margin zone. Such improvements to the interferogram are important for calculation of velocity from the phase.



(a)



(b)

Figure 4.6. Comparison of interferogram chips

Comparison of coherence histograms

Histograms of the two coherence images shown in Figure 4.7 are calculated to understand how the correlation values differ. Figure 4.7 illustrates the comparison of histograms of coherence images generated from the two co-registration methods. The dashed line is for the affine transformation method and the solid line is for the Delaunay triangulation based method. The dashed line histogram has two peaks, one around 0.1 representing the pixels (in Figure 4.5 (a)) with high decorrelation in the far range due to poor co-registration, and another peak is around 0.52 representing pixels with good correlation in the left lower portion of Figure 4.5(a). Nearly half of the pixels in the image have correlation values less than 0.3. The histogram of Figure 4.5(b) with the solid line dramatically shifts the histogram curve (solid line) to the right side. The peak around 0.1 is eliminated and the peak at 0.5 is enlarged. The change from 2 peaks to 1 peak suggests that the coherence for points whose original coherence around 0.1, the low peak, has been improved. Average correlation also increases from 0.336 to 0.4336. It should be understood that coherence will always be smaller than 1 even when co-registration is perfect, because there are other decorrelation sources. Figure 4.7 shows that the total decorrelation other than co-registration for the frame is about 0.52.

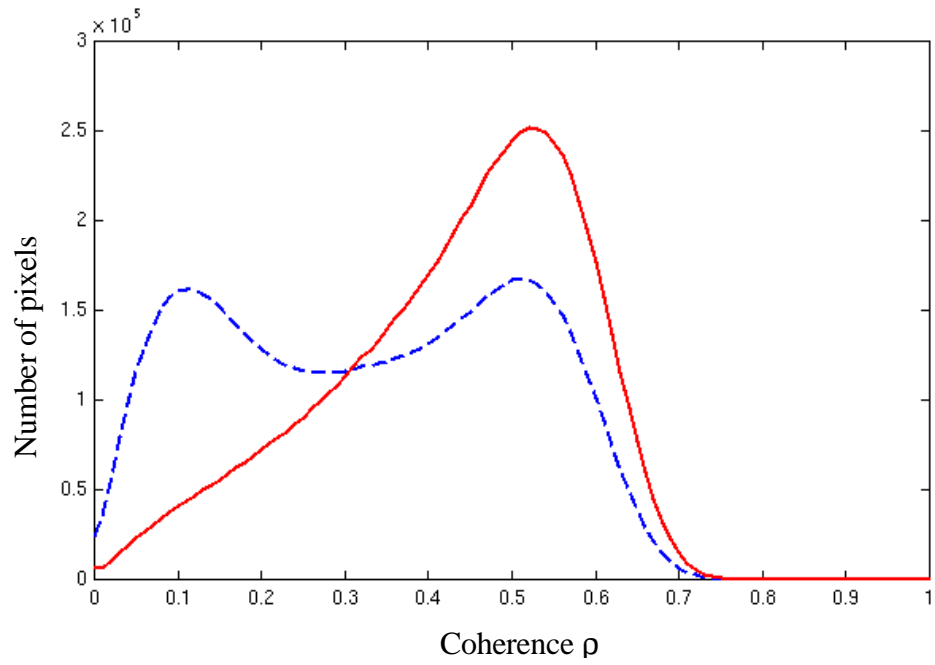


Figure 4.7. Comparison of histograms of coherence images in Figure 4.5. Dash line is for Figure 4.5(a), solid line is for Figure 4.5(b). The bin size used to count pixels is 0.01

Coherence mosaic of the East Antarctic Ice Streams

Using the new co-registration technique, a coherence mosaic of the East Antarctic Ice Streams is created by processing six InSAR swaths data acquired during the Antarctic Mapping Mission 1 (AMM-1) in 1997 covering the East Antarctic Ice Streams, including Filchner-Rone Ice Shelf, Bailey Glacier, Slessor Glacier, Recovery Glacier, RAMP Glacier, and Blackwall Ice Stream. For each frame, two InSAR images are co-registered using the Delaunay triangulation based co-registration, then the coherence image and the interferogram are calculated. The coherence images are rectified with terrain correction to ground space with a resolution of 200 m by 200 m. The coherence map is created by mosaicking all frames in the region. Figure 4.8 is the coherence mosaic of the East Antarctic Ice Streams created using the HSV color model. The hue is encoded according to a coherence value ranging from 0 to 1. The blue color represents low coherence and the red color represents high coherence. The SAR image is encoded as intensity.

During the mosaicking process, no radiometric balance or stretching is applied because correlation values are absolute representations of geophysical properties and should be preserved. As discussed above, coherence is influenced by many factors, including surface properties, data acquisition (baseline, signal bandwidth, and signal strength), SAR processing, and co-registration. Between two adjacent frames of the same swath, data acquisition and SAR processing effects are similar or vary continuously. Co-registration problems can cause an inconsistency of coherence in the overlap region, resulting in seam lines between adjacent frames of the same swath. The new co-registration method minimizes (nearly eliminates) the co-registration effect on coherence.

As a result, the overlapping region of any two adjacent frames on a swath has a consistent and continuous coherence across frames. There are seam lines between overlap swaths. This is caused by an acquisition effect, for instance, due to different baselines for different swaths. These effects on coherence are almost constant across a frame.

Figure 4.8 remarkably depicts the Ice Streams over the East Antarctic and reveals surficial geophysical properties. The coherence map will be used in scientific analysis of the East Antarctic Ice Streams. In Chapter 7, we will discuss the use of the coherence map in determining shear margins, grounding lines, and ice rises in the East Antarctic Ice Streams.

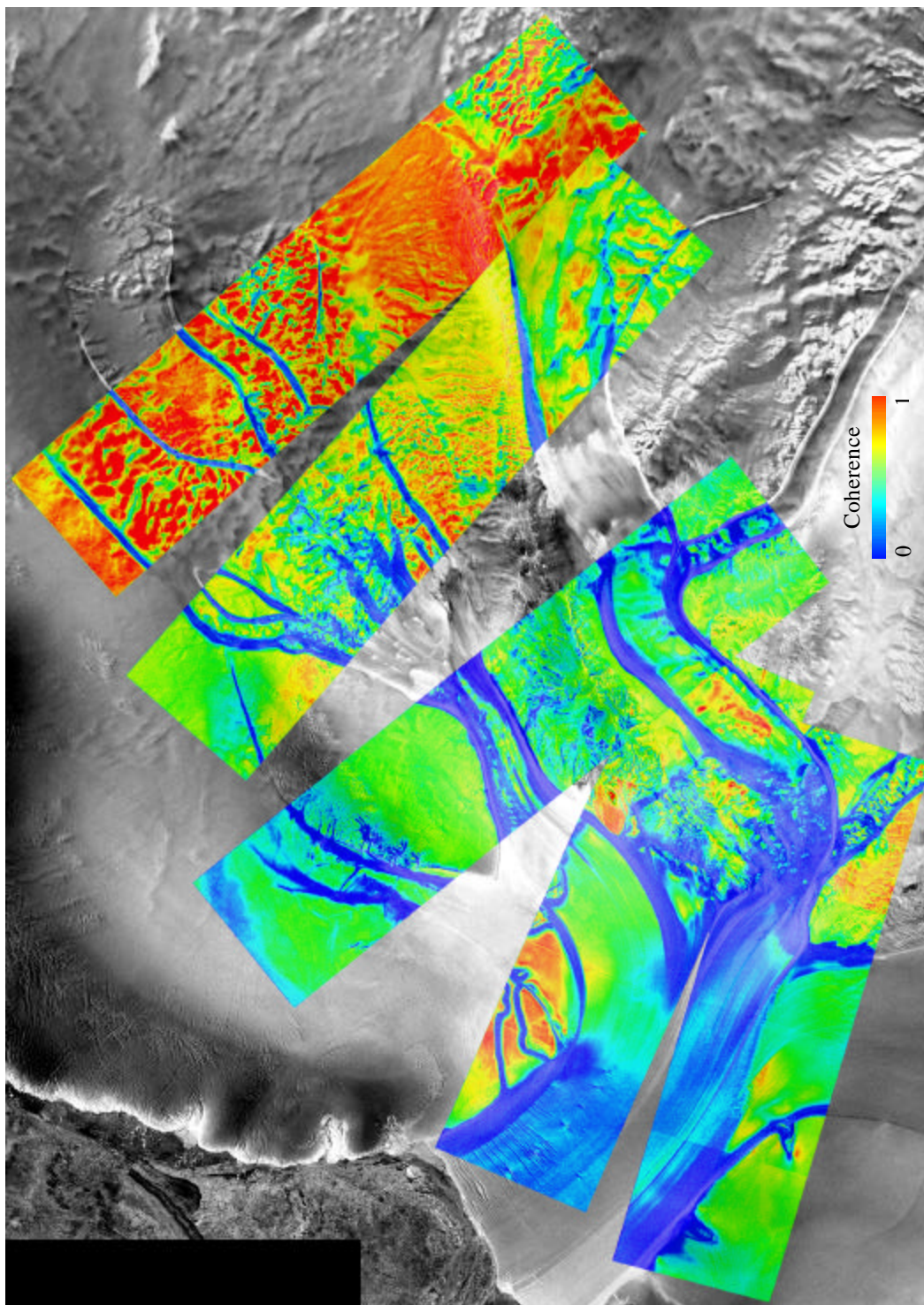


Figure 4.8: Coherence mosaic of the East Antarctic Ice Streams

CHAPTER 5

PHASE UNWRAPPING AND PHASE RECONCILIATION

5.1 Introduction

The measured interferometric phase is wrapped into the interval $(-\pi, \pi]$. There is a modulo- 2π ambiguity in the phase. To calculate surface motion or estimate surface elevation, the modulo- 2π ambiguity has to be removed and the wrapped value has to be converted into the unwrapped value.

Phase unwrapping has been studied for over 20 years. Many unwrapping algorithms have been developed and used in commercial software and research. They can handle a variety of situations and effectively unwrap phase for most applications, even with relatively low coherence. However, for application of RADARSAT InSAR over Antarctica, challenges still exist. For the Antarctic Ice Streams, ice moves fast (>200 m/year) and the shear margin is highly deformed. RADARSAT's 24-day repeat observation can result in temporal decorrelation. Shear margins or other low coherence regions partition the interferogram into isolated "islands". Each island has visible fringes and can be unwrapped successfully. Between any two islands, there is no fringe link. Figure 5.1 shows an example of such a situation. In Figure 5.1(a), the RAMP Glacier (middle) merges with Recovery Glacier (left to right). Due to heavy crevassing, shear

margins for both glaciers have very low coherence (Figure 5.1(b)). The dark bands separate the interferogram into several disconnected regions. Each individual region has clear fringes and can be phase unwrapped successfully. However, there is a phase ambiguity between these regions. If there are control points over every region, phase unwrapping can be solved using existing algorithms. In this research, we solve for the phase ambiguity between these regions with the help of range offset from speckle matching. Once all the regions are fitted into the single surface, phase ambiguity between every two regions can be solved.

In this chapter a brief review of phase unwrapping methods will be presented. The methods can be found in the literature (Goldstein and others, 1988; Ghiglia and Romero, 1994; Xu and Cumming, 1999; Joughin, 1995). Then the phase reconciliation method will be introduced. It can align all unwrapped phase components of the same image to a single reference. Error analysis, examples, and implementation of the method are also presented.

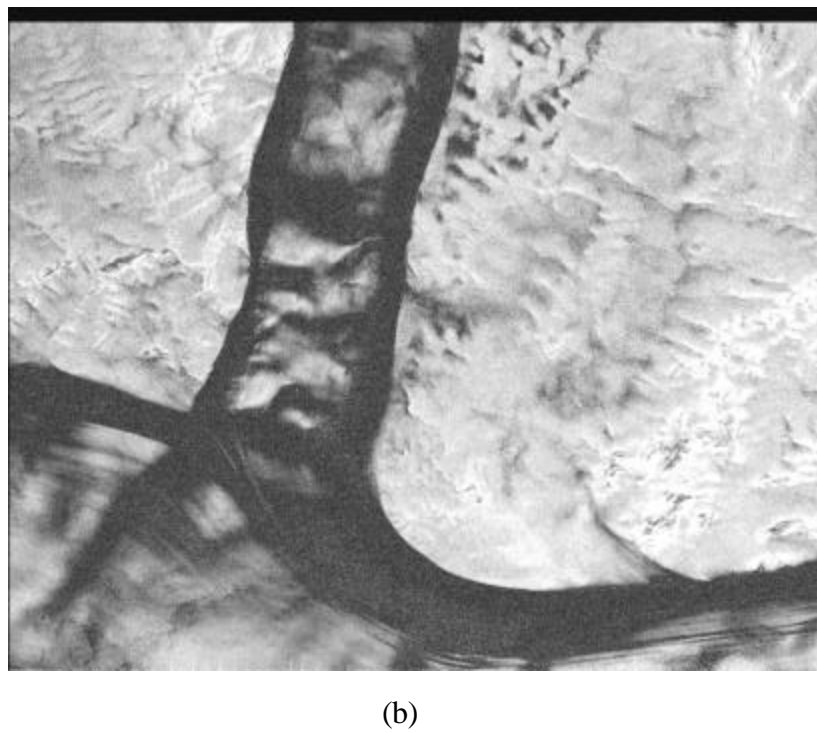
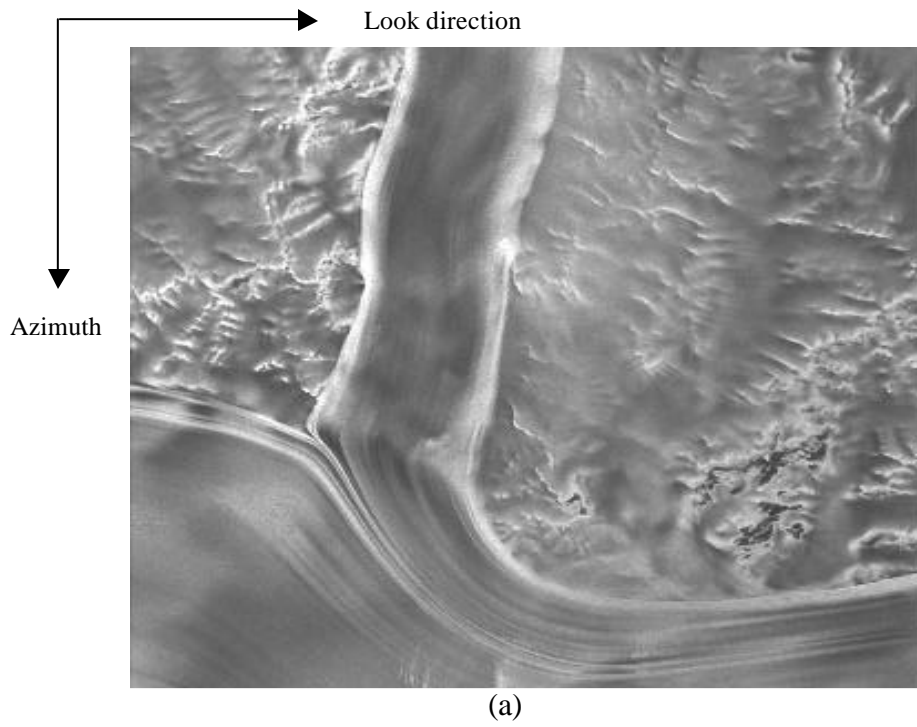


Figure 5.1. InSAR frame 5556 of orbit 9822/10165.
(a) SAR intensity image. (b) Coherence image

5.2 Phase Unwrapping

A basic phase unwrapping approach is an integration-based approach developed by Goldstein and others (1998). The approach is to integrate phase differences, adding the integer number of cycles that minimizes the phase differences. The image resolution is assumed to be fine enough that the phase change between two neighboring pixels does not exceed a half cycle. Under this assumption, the phase image is differentiated and the phase difference is wrapped to the interval $[-\pi, \pi]$.

If the phase image is error free, line integration from point A to point B should be independent of path. In other words, the integration along a closed path should be zero. Goldstein and others (1998) identify two types of errors in the unwrapped results: (1) local error caused by the noise from a few points, and (2) global errors in which local errors may be propagated to the entire data set. Local errors are indicated by residues, which are residues of closed path integration formed by each set of four pixels that are mutual neighbors. The residues are 0 if there is no local error, and $\pm\pi$ if there is local error.

Residues play a key role in selecting an integration path. If the path encloses a single residue, integration is not zero. However, if the path encloses an equal number of positive residues and negative residues, the integration is zero due to cancellation. To avoid the non-zero integration, branch cuts are made between residues to prevent any integration path from crossing. So the approach is to connect nearby positive and negative residues with cuts that intersect the integration path so that no net residues can be encircled and no global error generated, although local errors in the immediate vicinity of the residues may occur.

Goldstein and others (1988) implement the approach in a way to minimize the total length of the cuts and thereby minimize the total discontinuity. The image is scanned to find a starting residue. Then a box of size 3 is drawn around the residue, and another residue is searched in the box. If another residue is found, a branch cut is made between the two residues. If the new residue is of opposite sign, the cut is unchanged, and the image is searched for a new starting residue. Otherwise, the box moves to the new residue and repeats the above procedures. This process continues until no new residue is found in the box or an opposite sign residue that balances the cut is found. The box size will be increased by 2 for a new starting residue.

Joughin (1995) uses information in the residues themselves to help determine the shape of discontinuities. The algorithm classifies residues into two groups. The first group is for residues in regions where the density of residues is low and the second group is for residues from high-density regions. The classification is done by counting the number of residues in a box surrounding the residue. If the number of residues is smaller than a pre-defined threshold, the residue is assigned as a low-density residue. Otherwise, it is assigned as a high-density residue.

Low-density residues are typically related to a random error of phase, while the high density residues are related to phase changes. They are processed separately. Low-density residues are connected with a branch cuts if they have opposite signs and the distance between them is less than a threshold value. High-density residues are grouped to form regions using a morphological dilation operation. Then regions are labeled and balanced. Branch cuts are determined by the minimum of the weighted distances. Once

the branch cuts are selected, phase differences are integrated to calculate the unwrapped phase.

There are also other algorithms, which are not based on residues and branch cuts. One example is the algorithm developed by Ghiglia and Romero (1994). This algorithm first determines the wrapped phase difference in two dimensions, then finds a phase surface that fits the observations using least squares. The algorithm can generate an unwrapped phase by adding arbitrary values, not only multiples of 2π . Another algorithm developed by Xu and Cumming (1999) uses region growing to unwrap phase. The region-growing algorithm minimizes unwrapping errors by starting at pixels with high quality and processing along paths with high confidence. The algorithm is capable of correcting unwrapping errors to a certain extent and stopping their propagation.

5.3 Phase Reconciliation

All algorithms reviewed in the previous section can unwrap phases for a region where fringes are well connected. However, an interferogram image may be segmented by highly decorrelated areas. This often occurs in ice streams. For this case, we developed a phase reconciliation method that can merge all these individual regions into a large area in which all phase values have the same reference.

For an InSAR data pair, assume that the interferogram is divided into m pieces of isolated islands, called fringe zones, by highly decorrelated channels, called non-fringe zones. Each piece of interferogram can be unwrapped using the phase unwrapping algorithm described above, if the seed point is selected inside a fringe zone. Each fringe

zone has its own relative reference. m fringe zones have m reference points. As a result, there are m unknowns for the entire image.

Instead of finding solutions for m unknowns, “phase reconciliation” is used to fit all fringe zones into the same reference and to reduce the number of unknowns from m to 1. The key to the algorithm is to use range offset from speckle matching as a guide across the whole image. Figure 5.2 illustrates the relationship between the range difference of the two passes and the pixel offset in the two images.

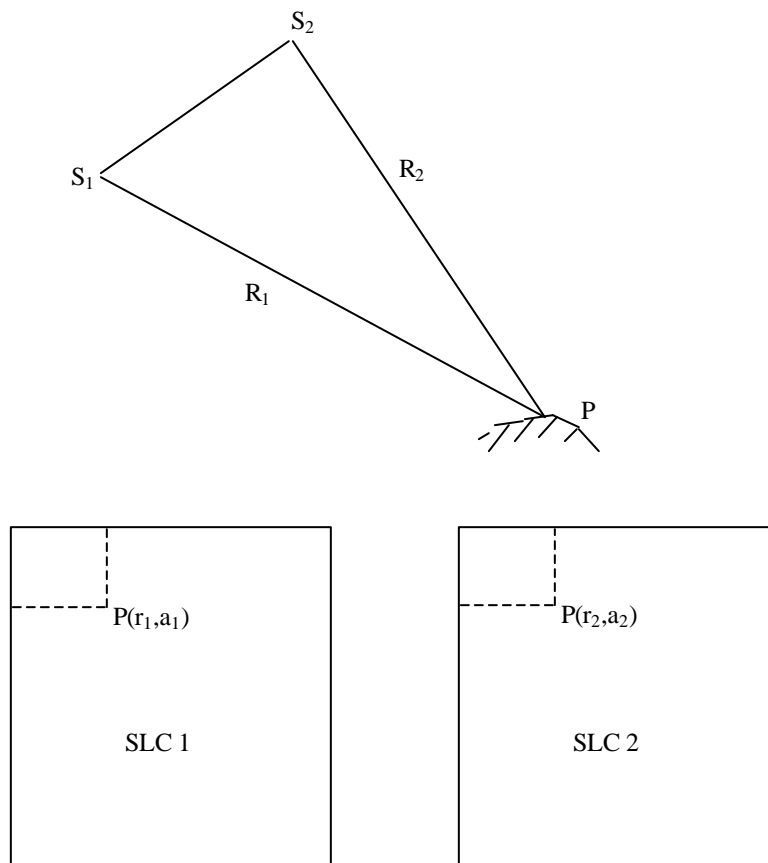


Figure 5.2 Relationship between range difference and pixel offset

Assume R_1 and R_2 are distances from the satellite to the target in the first and second passes. Then the range offset Δ is

$$\Delta = R_2 - R_1 \quad (5.1)$$

If we assume the unwrapped phase is Φ , we have

$$\Delta = \frac{1}{4p}(\Phi + \Phi_0) \quad (5.2)$$

where Φ_0 is a constant value associated with the relative reference point in phase unwrapping. Φ includes all effects from baseline, DEM, and motion.

From Figure 5.2, R_1 and R_2 can be expressed as functions of their pixel positions r_1 and r_2 in the slant range SLC images

$$R_1 = R_1^0 + r_1 R_r \quad (5.3)$$

$$R_2 = R_2^0 + r_2 R_r \quad (5.4)$$

where r_1 and r_2 are pixel positions of the target in range direction in the first and second images. R_1^0 and R_2^0 are ranges from the satellite to the first pixel in the first and second images, R_r is the pixel spacing in the range direction.

Subtracting equations (5.3) from (5.4) yields

$$R_2 - R_1 = R_2^0 - R_1^0 + R_r(r_2 - r_1) = R_2^0 - R_1^0 + R_r \mathbf{d}_r \quad (5.5)$$

where $\delta_r = r_2 - r_1$ is the range offset measured from speckle matching. Combining Equations (5.1), (5.2), and (5.5), we have the relationship between the unwrapped phase Φ and the range offset δ_r from the speckle matching as

$$R_r \cdot \mathbf{d}_r = \frac{1}{4p} \Phi + \left(\frac{1}{4p} \Phi_0 + R_1^0 - R_2^0 \right) \quad (5.6)$$

Since R_1^0 and R_2^0 are constant for the each frame, Φ_0 is constant for all points for a fringe zone, then the second term $\frac{I}{4p}\Phi_0 + R_1^0 - R_2^0$ in Equation 5.6 is constant for the fringe zone. Let $\Phi' = \Phi_0 + \frac{4p}{I}(R_1^0 - R_2^0)$, then Equation 5.6 can be rewritten as

$$R_r \cdot d_r = \frac{I}{4p}\Phi + \frac{I}{4p}\Phi' \quad (5.7)$$

Here Φ' is the unknown phase for the fringe zone and is related to the reference point used for phase unwrapping in the fringe zone and the InSAR geometry.

Notice that Φ is the unwrapped phase, which includes baseline, DEM, and motion effects. The range offset δ_r also includes these effects. Now we see that Φ and δ_r are two different measurements for the same thing: range offset. But they are different in the following aspects.

1. Φ is a phase measurement, while δ_r is measured from speckle matching
2. Φ unit is rad, while δ_r unit is pixel
3. Φ is a more accurate measurement than δ_r .
4. Φ is a relative measurement with respect to a arbitrary reference in a fringe zone, while δ_r is an absolute measurement across the frame.

The purpose of phase reconciliation is to find Φ' for every fringe zone and add it to the unwrapped phase. Using least squares adjustment, Φ' can be solved as

$$\Phi' = \frac{1}{N} \sum \left(\frac{4p}{I} R_r \cdot d_r - \Phi \right) \quad (5.8)$$

where N is the total number of points in the fringe zone. After solving Φ' , replace Φ with $\Phi + \Phi'$ for this fringe zone. Repeat this process for all fringe zones. The final phases for

all fringe zones in the frame are adjusted to remove the phase ambiguities between the fringe zones.

The method can be simply explained in this way. For the range shift, speckle matching provides a complete and absolute surface with relatively high noise. Interferometry provides many small patches with relatively high accuracy. If we add an additional phase value for a region, this region can fit into the range shift surface.

5.4 Error analysis

From (5.8), the uncertainty in Φ' is

$$\mathbf{s}^2_{\Phi'} = \frac{1}{N} \frac{16\mathbf{p}^2 Rr^2}{I^2} \mathbf{s}^2_d + \frac{1}{N} \mathbf{s}^2_{\Phi} \quad (5.9)$$

Whence

$$\mathbf{s}_{\Phi'} = \frac{\sqrt{\frac{16\mathbf{p}^2 Rr^2}{I^2} \mathbf{s}^2_d + \mathbf{s}^2_{\Phi}}}{\sqrt{N}} \quad (5.10)$$

where σ_{δ} is the range offset error from speckle matching, σ_{Φ} is phase error. Uncertainty in Φ' introduces systematic error in the final phase for the fringe zone. The system error is inversely proportional to square root of N, which is the number of points used in calculation in the fringe zone. The random error of the final phase is still the same as that of the original phase. Phase reconciliation does not change the random error of the phase.

Baseline, DEM and reference effects

The above discussion assumes that unwrapped phase Φ includes the baseline and DEM phases and the motion phase, since range offset δ from speckle matching also

includes this information. Baseline and DEM cause phase ramp and a high gradient in the interferogram. It may cause problems in phase unwrapping. A practical way is to remove the base line and DEM effect from the measured phase prior to phase unwrapping. Then add them back after phase unwrapping. Another way is to remove the baseline and DEM effects from the measured phase and speckle matching offsets. No matter which way we use, these effects will be canceled in Equation 5.8. So errors in the baseline and DEM will not contribute to the phase reconciliation.

The selection of a reference point in phase unwrapping does not affect phase reconciliation. When the reference changes from P_1 to P_2 , there is a constant phase change $\Delta\Phi$ in Φ . From Equation 5.8 we see that there will also be a opposite change $-\Delta\Phi$ in Φ' . So the new phase $\Phi+\Phi'$ remains the same, no matter which reference point we use.

5.5 Example

We will demonstrate the phase reconciliation technique using an InSAR frame 5556 of orbit 9822 and 10165 shown in Figure 5.1(a). In the frame, the RAMP glacier moves from the top down to an intersection with the Recovery Glacier, which is moving from left to right. The left upper quarter of the image and most of the right side of the image is slow moving ice. Some exposed rocks are visible from the image. High backscatter returns are visible in the shear margins of both the Recovery and RAMP glaciers. Extensive flow stripes appear where the RAMP and Recovery glaciers merge. Figure 5.1(b) shows the coherence of the two observations. As expected, shear margins have low coherence and are in dark tones. The off glacier areas (two sides of the RAMP

glacier) have high coherence. Inside the RAMP glacier and the Recovery glacier, there are large portions of areas with good coherence.

Figure 5.3 shows the interferogram of the frame after the baseline and DEM effects are removed. Figure 5.3(a) is for the entire frame and Figure 5.3(b) is the enlarged view of the box in Figure 5.3(a). The interferogram is the effect of surface motion only. Fringes are clearly on the slow motion area and most parts of the interiors of both glaciers. Fringes are destroyed at the shear margins. To do phase unwrapping, five seed points marked in the image are used. Their locations are listed in Table 5.1.

Each seed point listed above is used to run the phase unwrapping process. The process starts from the seed point and expands the unwrapped region until it is stopped by highly decorrelated channels. Figure 5.4 shows the five unwrapped regions from the five seed points. Each region has its own reference, as marked in Figure 5.3 (a). Regions A and B have a very small variation because they are slow moving areas. Regions C and D have larger phase variations because of the ice motion on Recovery Glacier.

The phase reconciliation method is applied on the five regions. Range offset from speckle matching is used as a global reference for each region. Since phases here include only motion effect, baseline and DEM effects are also removed from range offsets. For each region, we estimate the phase Φ' using (5.7) and then replace Φ with $\Phi+\Phi'$ for this region. The phase reconciliation result is listed in Table 5.1.

Region	Seed point	N	F' (rad)	S _{F'} (rad)
A	200,200	1994	17471	0.8
B	2500,1000	5172	17318	0.5
C	3363,2545	287	20091	2.1
D	70,2500	1607	19007	0.9
E	1420,500	884	16559	1.2

Table 5.1: Statistics of phase reconciliation for frame 5556 of orbit 9822/10165

In the table, column N is the number of points used in the calculation of Φ' . Φ' is the adjusted phase for a region. $S_{F'}$ is the systematic error of phase for the zone introduced by phase reconciliation. It is calculated using 5.10 in which $\sigma_{\delta}=0.02$, $Rr=8$ m, $\sigma_{\Phi}=0.2$. It is very small because it is inversely proportional to the square root of N. For region C, $S_{F'}$ of 2.1 rad is equivalent to a velocity error of 0.14 m/year.

The reconciliated phase is shown in the right bottom corner of Figure 5.4. The entire frame uses the same reference point. The two sides of the RAMP Glacier have small variation because they are stationary. The Recovery Glacier moves from left to right and the velocity increases from left to right. In the interior of the RAMP glacier, there are areas where phases are smaller than stationary areas. This is because the orientation of the RAMP Glacier is moving down and slightly toward the left. This means there is a motion component in the range direction moving toward the satellite.

A one-dimensional profile shown in Figure 5.5 is used to illustrate the change of phase in these steps. The profile is along a constant azimuth line near the bottom of the frame and crosses through region D and C. Figure 5.6(a) is an unwrapped phase of the

surface motion effect, only before phase reconciliation. The left segment is from region D and the range coordinate is from 0 to 2000. The phase value is about 50 at point 0, -250 at point 700, and 550 at 2000. From Table 1, Φ' is 19007 for region D. So the new phase for region D is about 19057 at point 0 and about 19557 at 2000. The segment from 2400 to 3550 is from region C. The phase is increased by 20091 for this region, according to Table 1. So this segment moves higher than the segment in region D in Figure 5.5(b). After phase reconciliation, the two segments are well aligned although there is a break between them. The new curves suggest that ice velocity increases in the range direction along this profile.

The technique presented in this chapter is extremely useful for interferometry applications in the Antarctic using RADARSAT InSAR data. The inner bodies of fast moving glaciers have good coherence, but they are isolated by heavily decorrelated shear margins. It is unlikely to have a sufficient number of velocity control points on the moving glaciers. With this technique, we are able to reference the interferogram in the whole frame to the same reference. This makes the velocity calibration easy because we have only one unknown for range motion. We also developed a technique to transmit velocity control points from one frame to its neighbor frame so we use one reference for a long strip. This significantly reduces the requirement of velocity control points in the Antarctic where they are expensive to obtain.

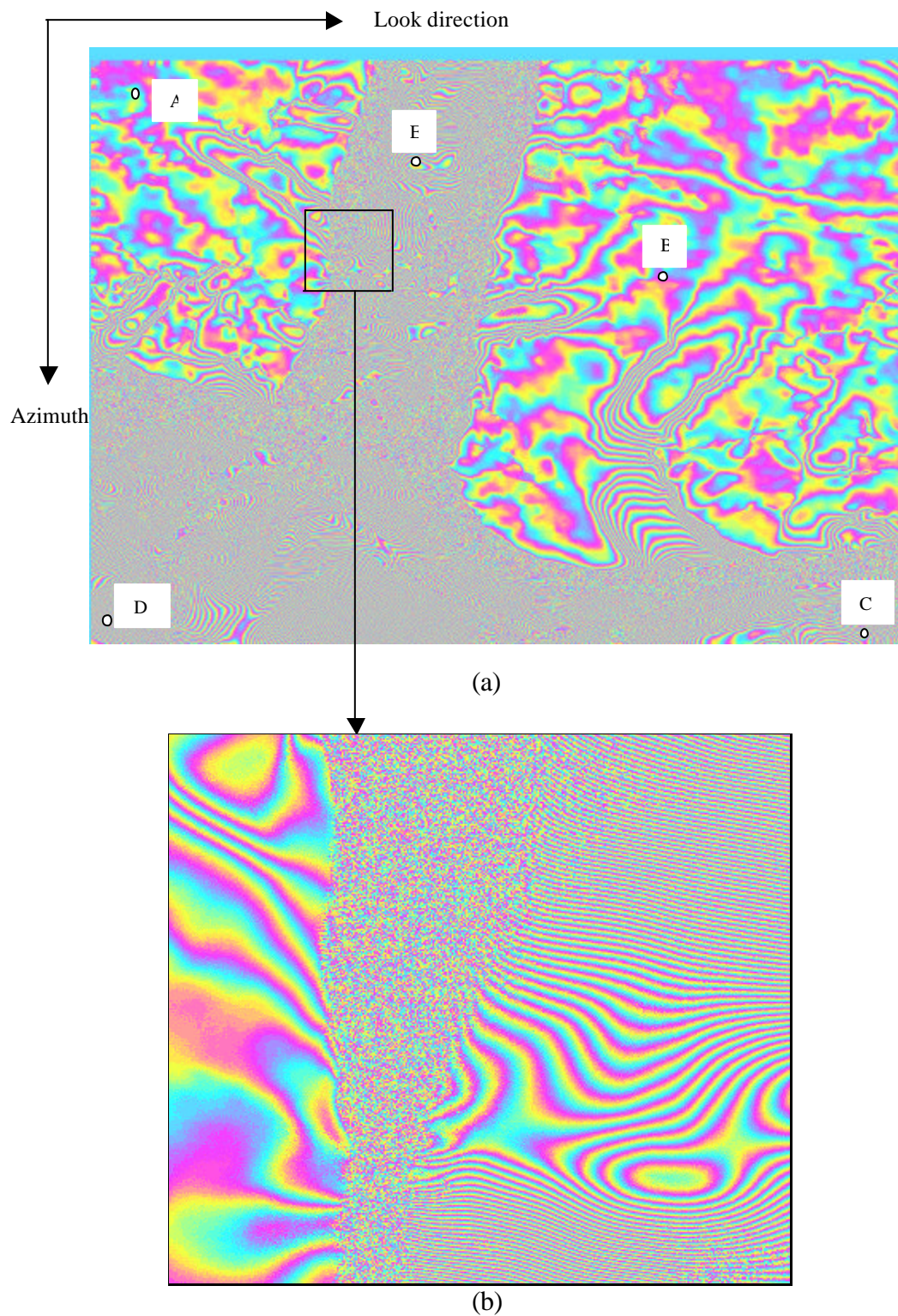


Figure 5.3: Wrapped phase after removal of baseline and topography. (a) entire frame with five seed points. (b) zoom in of small box in (a).

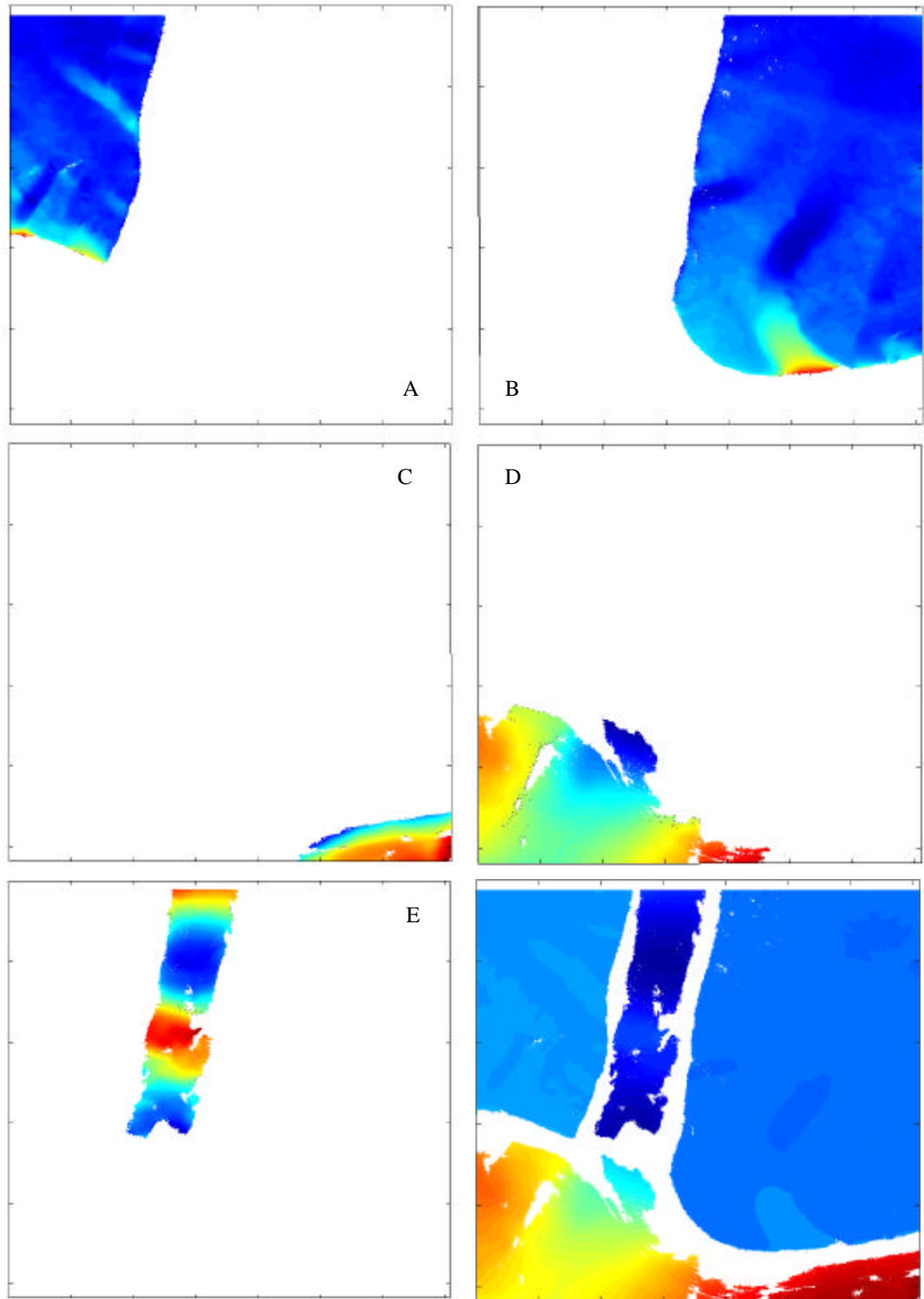
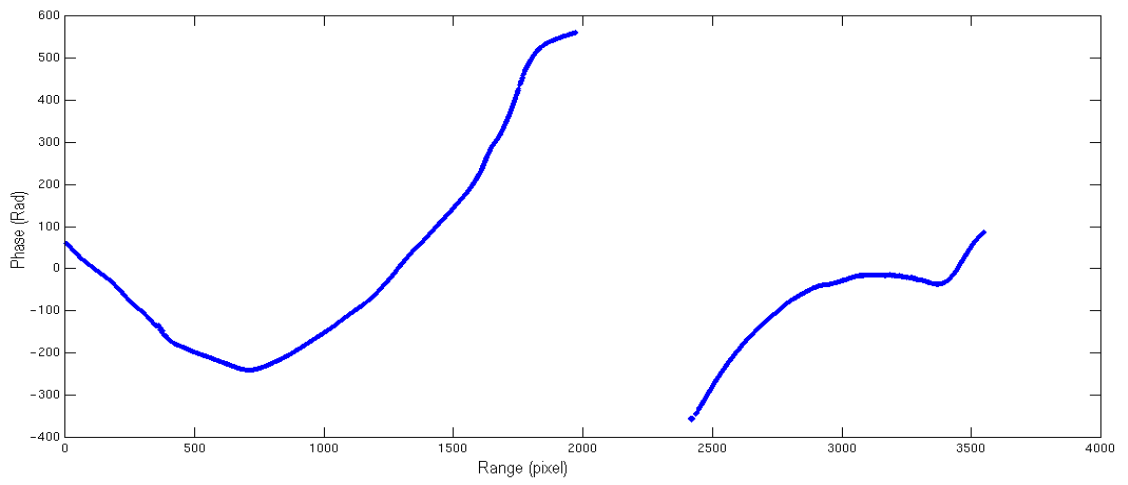
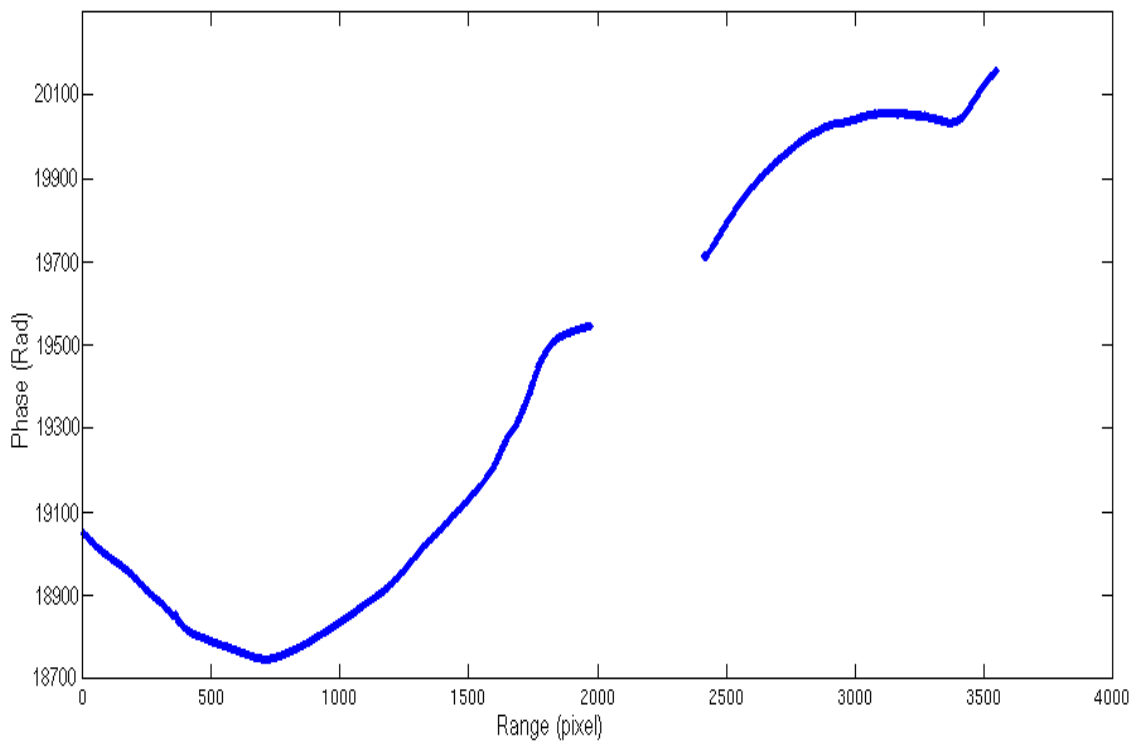


Figure 5.4: Unwrapped phase of five regions A-E using five reference points marked in Figure 5.3 and the merged phase. The final merged phase is at the right bottom corner. All phases are motion phases.



(a)



(b)

Figure 5.5: Phase profiles along a constant azimuth line before phase reconciliation (a) and after phase reconciliation (b)

5.6 Implementation

We demonstrate the technique in two steps: phase unwrapping and phase reconciliation. The implementation can integrate these two steps into one. The input to the process is the unwrapped phase of the entire frame and the range offset data from speckle matching. Baseline and topography effects should be removed from the unwrapped phase and range offset. The process first scans the phase image to find a reference point. Then from this point, phase unwrapping is performed. The pixels successfully unwrapped will be marked with a region number. After finishing a region, the region size is compared with a threshold. If the size is smaller than the threshold, then this region is discarded and marked as a failed region. If the size is larger than the threshold, then we use least squares to find the adjusted phase for this region with the range offset surface from speckle matching in this region. We continue to search another unprocessed pixel as a reference and repeat the steps above. After all pixels are processed, the image has a value that has either failed in unwrapping (like shear margins) or has been unwrapped and adjusted to range offset. In this case, the entire unwrapped phase has only one reference point. This is the only unknown in the range direction to calculate absolute velocity. How to estimate this unknown and calculate the absolute velocity are the topics to be covered in the next chapter.

CHAPTER 6

TWO-DIMENSIONAL SURFACE VELOCITIES OF THE EAST ANTARCTIC ICE STREAMS

6.1 Introduction

Two-dimensional ice sheet surface velocity is of prime importance in studying ice dynamics and mass balance. Methods to obtain two-dimensional surface velocity maps include in-situ observations, feature tracking from photogrammetric image sequences (Whillans and others, 1993) or optical satellite image sequences (Scambos and Binschadler, 1993), SAR interferometry (Joughin and others, 1998), and speckle matching of SAR images (Gray and others, 1998).

As discussed in Chapters 2 and 3, interferometry provides an excellent measurement of motion in the range direction, and speckle matching provides an optimal estimation of azimuth offset. We seek to make full use of the strength of both techniques to obtain the best possible result. The two-dimensional surface velocity field will be calculated by combining the range motion from interferometry and azimuth motion from speckle matching. In fact, Joughin and others (1999) have already used the idea on RADARSAT data over the West Antarctic Ice Streams. However, our work is different from Joughin and others (1999) in the following aspects. First, we provide a detailed

discussion on the calibration models and error analysis. Second, in addition to traditional velocity control points, we also use flow directions as velocity control points in velocity calibration. Third, we developed a strip calibration model designed to preserve velocity consistency between frames. We first present two-dimensional surface velocity calibration models for absolute velocity calculation. Then procedures and tools for processing RADARSAT InSAR data to generate a velocity maps are discussed. Also presented are analysis, quality assessment of the velocity mosaic, and comparison with velocity maps from other investigators.

6.2 Two-dimensional surface velocity

6.2.1 Velocity control points and velocity calibration

We compute the two-dimensional surface velocity for an InSAR pair by combining the range motion from interferometry and the azimuth motion from speckle matching. Requirements of velocity accuracy for scientific objectives are listed in Table 6.1 (Jezek, 1999b). Interferometry has excellent accuracy of 4 m/year for range motion. So range motion from interferometry is used as the range component in velocity. For the azimuth direction, speckle matching is the only way to generate motion in this direction using one InSAR pair. Fortunately, according to discussion in Section 3.4, the accuracy of azimuth motion from speckle matching is 10 m/year, better than speckle matching's range motion accuracy of 20 m/year. Although the accuracy of the speckle matching method is limited by pixel resolution, the azimuth motion from speckle matching has a better accuracy than range motion from speckle matching. This is because, first, the pixel spacing in the azimuth direction is smaller than the pixel spacing in the range direction (for

RADARSAT standard beams). Second, the range offset is dependent on the baseline and surface elevation. These factors contribute errors to the range motion. While the azimuth shift is almost independent to surface elevation, the shift due to orbit crossing is linear.

Science Product	Velocity Accuracy Requirement	Grid Spacing	Contribution to Measurement Objective
Continental coverage of velocity field	10% in speed, 5° in direction	5 km grid	Flow styles Flow variation Balance velocity
Selected study areas (e.g., East and West Antarctic Ice Streams, Lambert Glacier)	5 % in speed, 5 ° in direction	1 km grid	Mass balance Ice dynamics Nonsteady flow Calving flux
Grounding line velocities	20% in speed, 10° in direction	500 m grid within 20 km of the estimated grounding line	Grounding lines

Table 6.1 Velocity product requirements (from Jezek 1999b)

We seek the velocity vector

$$\bar{V} = V_r \tilde{r} + V_x \tilde{x} \quad (6.1)$$

where V_r and V_x represent the magnitude of the velocity components in the cross track and along track directions respectively, \tilde{r} and \tilde{x} are unit vectors.

V_r is calculated from the interferometric phase Φ that is presumably unwrapped, reconciled, and the topography corrected phase. So phase Φ can be expressed as

$$\Phi = \Phi_0 + \Phi_{motion} \quad (6.2)$$

where Φ_0 is the constant phase and Φ_{motion} is the phase due to surface motion in the range direction. Then the ground motion in the cross track direction, V_r , is

$$V_r = \frac{\lambda}{4pT \sin(\beta - \alpha_r)} \Phi_{\text{motion}} = \frac{\lambda}{4pT \sin(\beta - \alpha_r)} (\Phi - \Phi_0) \quad (6.3)$$

where λ is wavelength, T is time interval between the two observations, β is the incidence angle, and α_r is the surface slope angle in the cross track direction. In (6.3), once Φ_0 is known, the phase Φ can be converted to absolute speed V_r on ground in the cross track direction.

Azimuth motion V_x can be calculated from the measured azimuth offset δ (the subscript x representing the azimuth direction is omitted because only the azimuth offset is used in this chapter). A linear model is used to express the azimuth shift δ as

$$\mathbf{d} = a_0 + a_1 r + a_2 x + \mathbf{d}_{\text{motion}} \quad (6.4)$$

where r and x are the slant range image coordinates in the range and azimuth directions, and δ_{motion} is the azimuth offset due to surface motion in pixel's unit. a_0 , a_1 , and a_2 are coefficients of the azimuth offset model. The azimuth speed V_x can be calculated as

$$V_x = \frac{Rx}{T \cos \alpha_x} \mathbf{d}_{\text{motion}} = \frac{Rx}{T \cos \alpha_x} (\mathbf{d} - a_0 - a_1 r - a_2 x) \quad (6.5)$$

where Rx is the pixel spacing in the azimuth direction, and α_x is the surface slope angle in the azimuth direction. Parameters a_0 , a_1 , and a_2 are related to InSAR geometry. That is, a_0 is related to the parallel baseline, a_1 is related to the orbit squint angle, and a_2 is related to the change of the squint angle along the flight track. Since the squint angle is almost a constant for a 100 km frame as used in this research, we ignore this term. For generality,

we include it in the derivation. Once the three coefficients (parameters) a_0 , a_1 , and a_2 are known, absolute azimuth speed V_x can be calculated from the measured azimuth offset δ .

In Equations (6.3) and (6.5), there are four unknowns for the calculation of velocity. They are Φ_0 , a_0 , a_1 , and a_2 . Once the four unknowns are solved, the two-dimensional surface velocity can be calculated.

Velocity calibration solves the four unknowns in the offset models using velocity control points (VCP) and then calculates the surface velocity. Normally, VCP refers to a point with known position and velocity. In this research, we have expanded the definition of VCP and include the points with known velocity and points with known flow directions. In the following sections we will create observation equations in the calibration model for these types of velocity control points

Point with known velocity

A velocity control point P has known velocity component U_r in the cross track direction and U_x in the azimuth direction. A stationary point is a special case in which $U_r=0$ and $U_x=0$. From Equations 6.3 and 6.5, we can create observation equations for a velocity control point as

$$\frac{1}{4pT \sin(\mathbf{b} - \mathbf{a}_r)}(\Phi - \Phi_0) = U_r \quad (6.6)$$

$$\frac{R_x}{T \cos \mathbf{a}_x}(\mathbf{d} - a_0 - a_1 r - a_2 x) = U_x \quad (6.7)$$

Points with known flow directions

Flow direction has been used to visually inspect velocity vectors on an image. Flow direction is also used to convert range motion to two-dimensional motion (Schmidt, 1999; Fatland, 1998). In this research, it is used to calibrate velocity for areas where there are no other control points. A flow direction observed from a flow stripe defines a ratio of range motion and azimuth motion, as shown in Figure 6.1. This relationship forms an observation equation for velocity calibration as

$$\frac{V_r}{V_x} = \frac{D_r}{D_x} \quad (6.8)$$

where D_r and D_x are cross track components and along track components of flow direction in a horizontal plane.

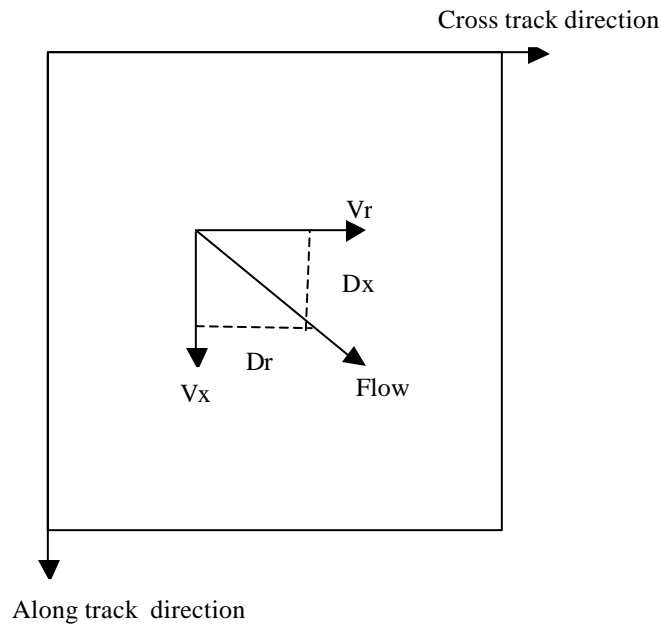


Figure 6.1 Flow direction control point

This type of point relies on the flow stripe to identify flow direction. In some areas where ice dynamics changes, flow stripes may not represent the true flow direction (Casassa and others, 1991). A carefully study is required before selecting the flow direction as a control point.

For a flow direction point shown in Figure 6.1, if the flow direction in the slant range single look complex image coordinate system is (d_r, d_x) , then the flow direction in the local ground coordinate system is

$$D_r = \frac{dr \cdot Rr}{\sin(\mathbf{b} - \mathbf{a}_r)} \quad (6.9)$$

$$D_x = \frac{dx \cdot Rx}{\cos \mathbf{a}_x} \quad (6.10)$$

Because velocity components and flow vector components have the relationship

$$V_r \cdot D_x = V_x \cdot D_r \quad (6.11)$$

Substitute Equations (6.3), (6.5), (6.9), and (6.10) into equation (6.11) to yield

$$\frac{I}{4pT \sin(\mathbf{b} - \mathbf{a}_r)} (\Phi - \Phi_0) \frac{dx \cdot Rx}{\cos \mathbf{a}_x} = \frac{Rx}{T \cos \mathbf{a}_x} (\mathbf{d} - a_0 - a_1 r - a_2 x) \frac{dr \cdot Rr}{\sin(\mathbf{b} - \mathbf{a}_r)} \quad (6.12)$$

Canceling terms in (6.12) and the equation can be simplified to

$$\frac{I}{4p} (\Phi - \Phi_0) dx = (\mathbf{d} - a_0 - a_1 r - a_2 x) dr \cdot Rr \quad (6.13)$$

Each velocity control point creates one or two observation equations. Then, four unknowns can be solved by least squares adjustment techniques. Since there are two observation variables in one equation, we use least squares model of conditional equations with unknown parameters (Mikhail and Ackermann, 1976).

6.2.2 Baseline refinement

The baseline distance is used in calculation to subtract the topographic phase from the measured phase. Initially, the baseline is calculated from the satellite orbit ephemeris and may have errors up to several meters. Zebker and others (1994) and Joughin (1995) have discussed baseline refinement with ground control points. We follow the work of Joughin (1995) and extend the model to include velocity points and points with known flow direction.

In a 100 km frame, a baseline can be modeled as a linear function of azimuth coordinates x . The model has four parameters:

B_{n0} : Perpendicular baseline at the image center

B_{p0} : Parallel baseline at the image center

dB_n : Perpendicular baseline change rate along flight direction. Unit is m/m

dB_p : Parallel baseline change rate along flight direction. Unit is m/m

Then the perpendicular baseline at pixel position (r,x) can be expressed as

$$B_n = B_{n0} + dB_n(x - x_0)R_x \quad (6.14)$$

where x_0 is the azimuth coordinate at image center and R_x is the azimuth pixel spacing.

Similarly, the parallel baseline at the pixel position (r,x) can be expressed as

$$B_p = B_{p0} + dB_p(x - x_0)R_x \quad (6.15)$$

From Equation (2.4), for case there is no motion, we have

$$B \sin(\mathbf{q} - \mathbf{x}) = -\Delta - \frac{\Delta^2}{2r_0} + \frac{B^2}{2r_0} \quad (6.16)$$

The left side can be expressed as

$$B \sin(\mathbf{q} - \mathbf{x}) = B \sin((\mathbf{q}_c - \mathbf{x}) + \mathbf{q}_d) = Bn \sin \mathbf{q}_d + Bp \cos \mathbf{q}_d \quad (6.17)$$

Combining (6.16) and (6.17), the range shift can be expressed as

$$\Delta = -\frac{\Delta^2}{2r_0} + \frac{B^2}{2r_0} + B \sin(\mathbf{q} - \mathbf{V}) = -\frac{\Delta^2}{2r_0} + \frac{B^2}{2r_0} + Bn \sin \mathbf{q}_d + Bp \cos \mathbf{q}_d \quad (6.18)$$

If we represent Δ as a phase difference, then (6.18) can be written as

$$\Phi + \Phi_{topo} - \Phi_0 = \frac{4\mathbf{p}}{\mathbf{I}} \left(-\frac{\Delta^2}{2r_0} + \frac{B^2}{2r_0} + Bn \sin \mathbf{q}_d + Bp \cos \mathbf{q}_d \right) \quad (6.19)$$

where Φ is the unwrapped phase, after removing the baseline and the DEM effect, Φ_{topo} is the phase due to the baseline and DEM, and Φ_0 is the phase adjustment to an absolute reference. Since Φ refers to the phase without DEM and baseline effect in this chapter, $\Phi + \Phi_{topo}$ represents the measured phase after phase unwrapping.

Equation (6.19) assume stationary control points. If the surface is moving with phase Φ_{motion} , then (6.19) becomes

$$\Phi + \Phi_{topo} - \Phi_0 - \Phi_{motion} = \frac{4\mathbf{p}}{\mathbf{I}} \left(-\frac{\Delta^2}{2r_0} + \frac{B^2}{2r_0} + Bn \sin \mathbf{q}_d + Bp \cos \mathbf{q}_d \right) \quad (6.20)$$

Substitute (6.14) and (6.15) into (6.20), yield

$$\begin{aligned} & \Phi + \Phi_{topo} - \Phi_0 - \Phi_{motion} \\ &= \frac{4\mathbf{p}}{\mathbf{I}} \left(\frac{Bp^2}{2r_0} + Bn_0 \sin \mathbf{q}_d + dBn(x-x_0)Rx \sin \mathbf{q}_d + Bp_0 \cos \mathbf{q}_d + dBp(x-x_0)Rx \cos \mathbf{q}_d \right) \end{aligned} \quad (6.21)$$

So the range velocity V_r can be expressed as

$$\begin{aligned}
 V_r &= \frac{\mathbf{I}}{4pT \sin \mathbf{b}} \Phi_{motion} \\
 &= \frac{\mathbf{I}}{4pT \sin \mathbf{b}} \left[\Phi + \Phi_{topo} - \Phi_0 - \frac{4p}{\mathbf{I}} \left(\frac{Bp_0^2}{2r_0} + Bn \sin \mathbf{q}_d + dBn(x - x_0)Rx \sin \mathbf{q}_d + Bp \cos \mathbf{q}_d + dBp(x - x_0)Rx \cos \mathbf{q}_d \right) \right]
 \end{aligned} \tag{6.22}$$

In this expression, there are four unknowns: Bp_0 , dBp , Bn_0 , and dBn . Because Bp is very small when compared to r_0 , the term $\frac{Bp^2}{2r_0}$ can be approximated by $\frac{Bp_0^2}{2r_0}$.

For the azimuth direction, the velocity model is derived by Equation (6.5). It has three parameters. Together, range and azimuth velocity models have seven parameters. Here Φ_0 is determined from velocity calibration.

By applying (6.3) and (6.5) to the observation equations of various velocity control points, the baseline refinement observation equations can be created. Using a least squares adjustment model, the seven parameters mentioned above can be solved. Among those seven parameters, four are baseline parameters.

Assume X is unknown with elements

$$X = \begin{bmatrix} Bn_0 \\ dBn \\ Bp_0 \\ dBp \\ a_0 \\ a_1 \\ a_2 \end{bmatrix} \tag{6.23}$$

Then observation equations for each type of control points can be derived with the use of steps similar to those shown in Section 6.2.1. For velocity control point P with velocity

Ur in the cross track direction and Ux in the along track direction, two observations equations are

$$\begin{bmatrix} \sin \mathbf{q}_d & (x-x_0)R_x \sin \mathbf{q}_d & \cos \mathbf{q}_d & (x-x_0)R_x \cos \mathbf{q}_d & 0 & 0 & 0 \end{bmatrix} X = \left[\frac{1}{4p}(\Phi + \Phi_{topo} - \Phi_0) - UrT \sin \mathbf{q} - \frac{B_{p0}^2}{2r_0} \right] \quad (6.24)$$

$$\begin{bmatrix} 0 & 0 & 0 & 0 & R_x & rR_x & xR_x \end{bmatrix} X = [\mathbf{d} \cdot R_x - T \cos \mathbf{a}_x U_x] \quad (6.25)$$

For a flow direction control point P with flow direction vector (d_r, d_x) in slant range SLC image, the observation equation is

$$\begin{bmatrix} dx \sin \mathbf{q}_d & dx(x-x_0)R_x \sin \mathbf{q}_d & dx \cos \mathbf{q}_d & dx(x-x_0)R_x \cos \mathbf{q}_d & drR_r & rdrR_r & xdrR_r \end{bmatrix} X = \left[-\frac{1}{4p} dx(\Phi + \Phi_{topo} - \Phi_0) + \frac{B_{p0}^2}{2r_0} dx + dxR_r \mathbf{d} \right] \quad (6.26)$$

6.2.3 Strip calibration

Strip configuration

In Section (6.2.1), the velocity calibration is based on a single frame of InSAR data. For InSAR data used in this research, a strip of InSAR data is divided into frames 100 km long and with 10% overlap between frames. If the velocity calibration for each frame is independent, the velocities calculated from two neighboring frames in the overlap area might have large difference because of the different quality and distribution of velocity control points for each frame. Theoretically, velocities calculated from the two frames for the overlap area should be the same. This condition can be used as a constraint in a strip calibration.

Figure 6.2 is the configuration of a strip with M frames. Each frame has its own velocity control points. In the overlap area of any two neighboring frames, some points are selected as tie points. What follows is a discussion on how to use these points in the velocity calibration.

As discussed in Section 6.2.1, each frame has its own velocity control points and unknowns. For the i^{th} frame, the velocity calibration equations are

$$A_i X_i = B_i \quad (6.27)$$

where X_i is a vector of four unknowns for the i^{th} frame

$$X_i = \begin{bmatrix} \Phi^i_0 \\ a^i_0 \\ a^i_1 \\ a^i_2 \end{bmatrix} \quad (6.28)$$

A_i is an N_i by 4 matrix and B is an N_i by 1 matrix. N_i is the number of the observation equations for the i^{th} frame.

For a tie point in the overlap area of the i^{th} frame and $i+1^{\text{st}}$ frame, the phase in the i^{th} frame and $i+1^{\text{st}}$ frame can be expressed respectively as

$$\Phi^i = \Phi^i_0 + \Phi_{motion} \quad (6.29)$$

$$\Phi^{i+1} = \Phi^{i+1}_0 + \Phi_{motion} \quad (6.30)$$

Subtracting (6.30) from (6.29), yields

$$\Phi^i_0 - \Phi^{i+1}_0 = \Phi^i - \Phi^{i+1} \quad (6.31)$$

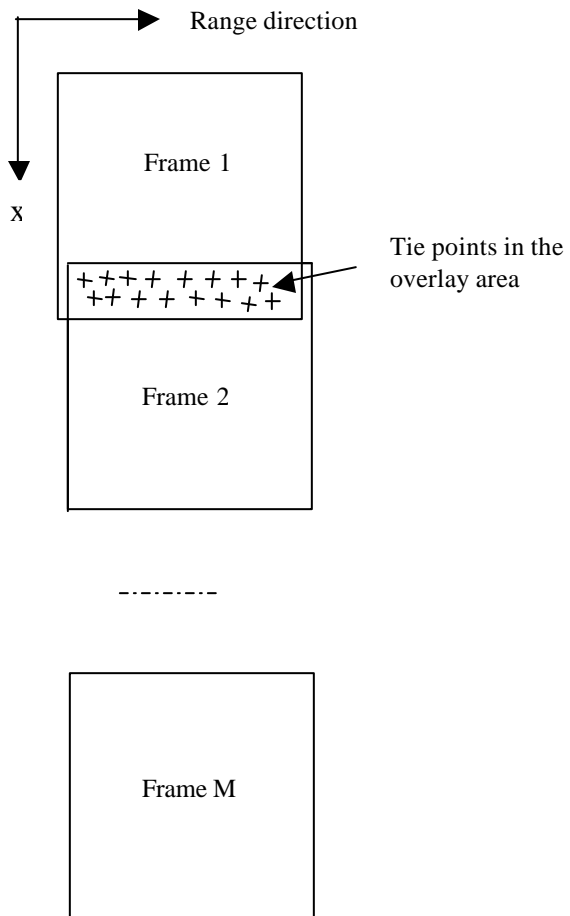


Figure 6.2: Frame configuration of strip calibration

In the azimuth direction, the azimuth offsets from the i^{th} frame and $i+1^{\text{st}}$ frame can be expressed respectively as

$$\mathbf{d}^i = a^i_0 + a^i_1 r^i + a^i_2 x^i + \mathbf{d}_{motion} \quad (6.32)$$

$$\mathbf{d}^{i+1} = a^{i+1}_0 + a^{i+1}_1 r^{i+1} + a^{i+1}_2 x^{i+1} + \mathbf{d}_{motion} \quad (6.33)$$

Subtracting (6.33) from (6.32), yield

$$a^i_0 + a^i_1 r^i + a^i_2 x^i - a^{i+1}_0 - a^{i+1}_1 r^{i+1} - a^{i+1}_2 x^{i+1} = \mathbf{d}^i - \mathbf{d}^{i+1} \quad (6.34)$$

(6.31) and (6.34) are two equations for each tie point. Assume there are k_i tie points on the overlap area of frame i and frame $i+1$, then the $2*k_i$ equations have the matrix format as

$$\begin{bmatrix} 1 & 0 & 0 & 0 & -1 & 0 & 0 & 0 \\ 0 & 1 & r^i_1 & x^i_1 & 0 & 1 & -r^{i+1}_1 & -x^{i+1}_1 \\ & & \dots & \dots & \dots & & & \\ 1 & 0 & 0 & 0 & -1 & 0 & 0 & 0 \\ 0 & 1 & r^i_j & x^i_j & 0 & 1 & -r^{i+1}_j & -x^{i+1}_j \\ & & \dots & \dots & \dots & & & \\ 1 & 0 & 0 & 0 & -1 & 0 & 0 & 0 \\ 0 & 1 & r^i_{k_i} & x^i_{k_i} & 0 & 1 & -r^{i+1}_{k_i} & -x^{i+1}_{k_i} \end{bmatrix} \cdot \begin{bmatrix} X_i \\ X_{i+1} \end{bmatrix} = \begin{bmatrix} \Phi^i_1 - \Phi^{i+1}_1 \\ \mathbf{d}^i_1 - \mathbf{d}^{i+1}_1 \\ \dots \\ \Phi^i_j - \Phi^{i+1}_j \\ \mathbf{d}^i_j - \mathbf{d}^{i+1}_j \\ \dots \\ \Phi^i_{k_i} - \Phi^{i+1}_{k_i} \\ \mathbf{d}^i_{k_i} - \mathbf{d}^{i+1}_{k_i} \end{bmatrix} \quad (6.35)$$

In the left matrix, the upper index refers to the frame number, while the lower index refers to the point number. Using new notations, Equation (6.35) can be simplified as

$$[C_i \quad C'_i] \cdot \begin{bmatrix} X_i \\ X_{i+1} \end{bmatrix} = [D_i] \quad (6.36)$$

where C_i and C'_i are matrices of size $2*k_i$ by 4, and D_i is a matrix of size $2*k_i$ by 1.

Combining all the observation equations for all the frames and all the tie point observation equations for the overlap areas, the new observation equations for the strip of M frames are

$$\begin{bmatrix} A_1 & 0 & \dots & 0 & 0 \\ 0 & A_2 & \dots & 0 & 0 \\ \dots & \dots & \dots & \dots & \dots \\ 0 & 0 & \dots & A_{M-1} & 0 \\ 0 & 0 & \dots & 0 & A_M \\ C_1 & C'_1 & \dots & 0 & 0 \\ \dots & \dots & \dots & \dots & \dots \\ 0 & 0 & \dots & C_{M-1} & C'_{M-1} \end{bmatrix} \cdot \begin{bmatrix} X_1 \\ X_1 \\ \dots \\ X_M \end{bmatrix} = \begin{bmatrix} B_1 \\ B_2 \\ \dots \\ B_{M-1} \\ B_M \\ D_1 \\ \dots \\ D_{M-1} \end{bmatrix} \quad (6.37)$$

In this model, 4*M unknowns for M frames are solved. Since there are some equations contain two observation variables, least squares model of conditional equations with unknown parameters is used to solve parameters (Mikhail and Ackermann, 1976). The model minimizes errors for the overlap areas and preserves the consistency between frames. For a frame with no velocity control points, we cannot calibrate based on a single frame. By using tie points in the overlap areas with other frames, the four unknowns for this frame can be solved and the velocity can be calculated in the strip calibration model. So this technique improves the accuracy of the velocity calculation for the entire strip. Moreover, it solves problems for frames in which there are no velocity control points. The velocity control points in other frames can contribute to the calibration through tie points between frames. Examples in Section 6.2.4 will show how velocities are improved using this technique.

6.2.4 Examples

Frames 5527 of orbit 9851/10194 are used as an example to demonstrate the methods of velocity calibration, baseline refinement, and strip calibration. These methods use any type of velocity control points or combination of velocity control points. Flow direction control points are a new type of velocity control point used in this research. Figure 6.3 shows velocity control points selected for frame 5527 in the calibration tool. The flow direction is shown as a line segment, and the point is marked as a circle in the middle of the line segment. The flow directions are created by drawing a line on the slant range SAR image along the flow stripes. Using the 24 flow directions as shown in Figure 6.3, 24 observation equations are created using 6.1 and the parameters for the range and azimuth offset model are solved as $\Phi_0=-352.0649$, $a_0=4.2927$, $a_1=8.2624e-5$. The parameters are solved using only flow directions.

By substituting these values into Equations (6.3) and (6.5), the velocity components V_r and V_x , for any given point (r,x) , can be calculated as

$$V_r = \frac{I}{4pT \sin(\mathbf{b} - \mathbf{a}_r)} (\Phi + 352.0649) \quad (6.38)$$

$$V_x = \frac{Rx}{T \cos \mathbf{a}_x} (\mathbf{d} - 4.2927 - 0.000082624r) \quad (6.39)$$

The velocity vectors are displayed in Figure 6.4. An enlarged view of the left bottom corner of the frame is shown in Figure 6.5. The vectors fit the flow stripe very well. The calibration tool will be discussed in the next section.

We have conducted tests on the same frame using stationary points. Table 6.2 lists the parameters derived using two types of velocity control points

	F₀(rad)	a₀(pixel)	a₁(pixel/pixel)
Flow directions	-352.0649±1.1	4.2927±1.1e-5	8.2624e-5±2e-12
Stationary points	-400.379±7.066	4.207±3.57e-4	8.0128e-5±6e-12

Table 6.2: Calibration parameters from different type of velocity control points

Baseline refinement is performed using stationary velocity control points. The refined baseline and the baseline estimated from orbit parameters are listed in Table 6.3. The baseline from orbits is estimated by Vexcel's software PHASE.

	B_n (m)	dB_n (m/m)	B_p (m)	DB_p (m/m)
Baseline from orbit ephemeris	191.86	3.75e-5	-95.11	-6.18e-6
Refined baseline	200.97±3.52	3.32e-6±1.6e-9	-79.87±7.7e-3	-2.3e-5±2.3e-11

Table 6.3: Refined baseline and baseline from satellite orbits

The test for strip calibration is performed on frames 5527 and 5544, between which there is a 10 km wide overlap area. First, each frame is calibrated independently using its own velocity control points, then 100 tie points are added in the overlap area and the strip

calibration model is applied as discussed in 6.2.3 to calculate the new parameters for each frame. Table 6.4 lists the results of these parameters.

		$F_0(\text{rad})$	$a_0(\text{pixel})$	$a_1(\text{pixel/pixel})$
Frame calibration	5527	-400.379	4.2070	0.000080128
	5544	-260.424	-1.9727	0.000068165
Strip calibration	5527	-358.734	4.224159	0.00007495
	5544	-274.013	-1.982954	0.000071

Table 6.4: Calibration parameters from frame calibration and from strip calibration

As mentioned above, parameters Φ_0 , a_0 , and a_1 are related to the InSAR geometry. Since satellite orbits are quite smooth and change gradually along the flight direction, parameters Φ_0 , a_0 , and a_1 for frames in a strip are correlated. The strip calibration acts as a “smoother” to smooth the parameters derived from each individual frame. For example, a_1 , a parameter related to orbit squint, changes from 0.000080128 for frame 5527 to 0.000068165 for frame 5544 when velocity calibrations are performed independently for each frame. But when using strip calibration, a_1 changes from 0.00007495 for frame 5527 to 0.000071 for frame 5544. The jump of a_1 between the two frames becomes smaller.

To demonstrate how strip calibration improves the velocity, velocity differences for the overlap area from both frames are calculated. For frame based calibration, the velocity difference has a mean value of 4.39 m/year and a standard deviation of 6.72 m/year. The mean value of 4.39 m/year results from two frames using different control

points, different distribution, as well as a slightly different geometry between the two frames. When strip calibration is used, the velocity difference has mean value of 0.55 m/year and a standard deviation of 4.963 m/year. The systematic bias is almost eliminated because tie points are used to balance the parameters for the two frames. The standard deviation is also reduced from 6.7427 to 4.9628. The improvement for the standard deviation is not so significant because the variation is mainly due to the random noise of the phase and speckle matching.



Figure 6.3: Flow direction control points are selected in velocity calibration

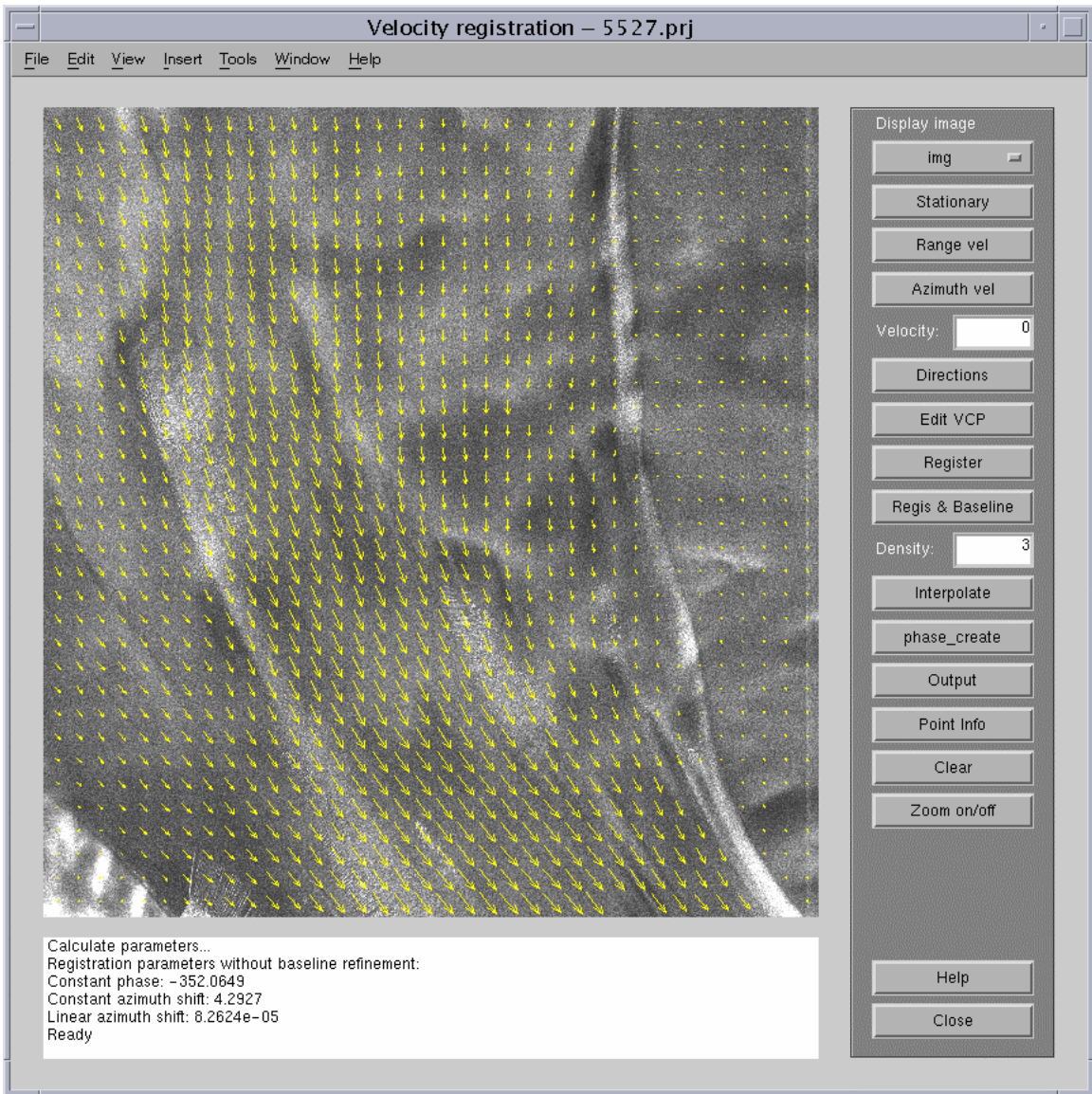


Figure 6.4: Velocity vectors after calibration using flow directions shown in Figure 6.3

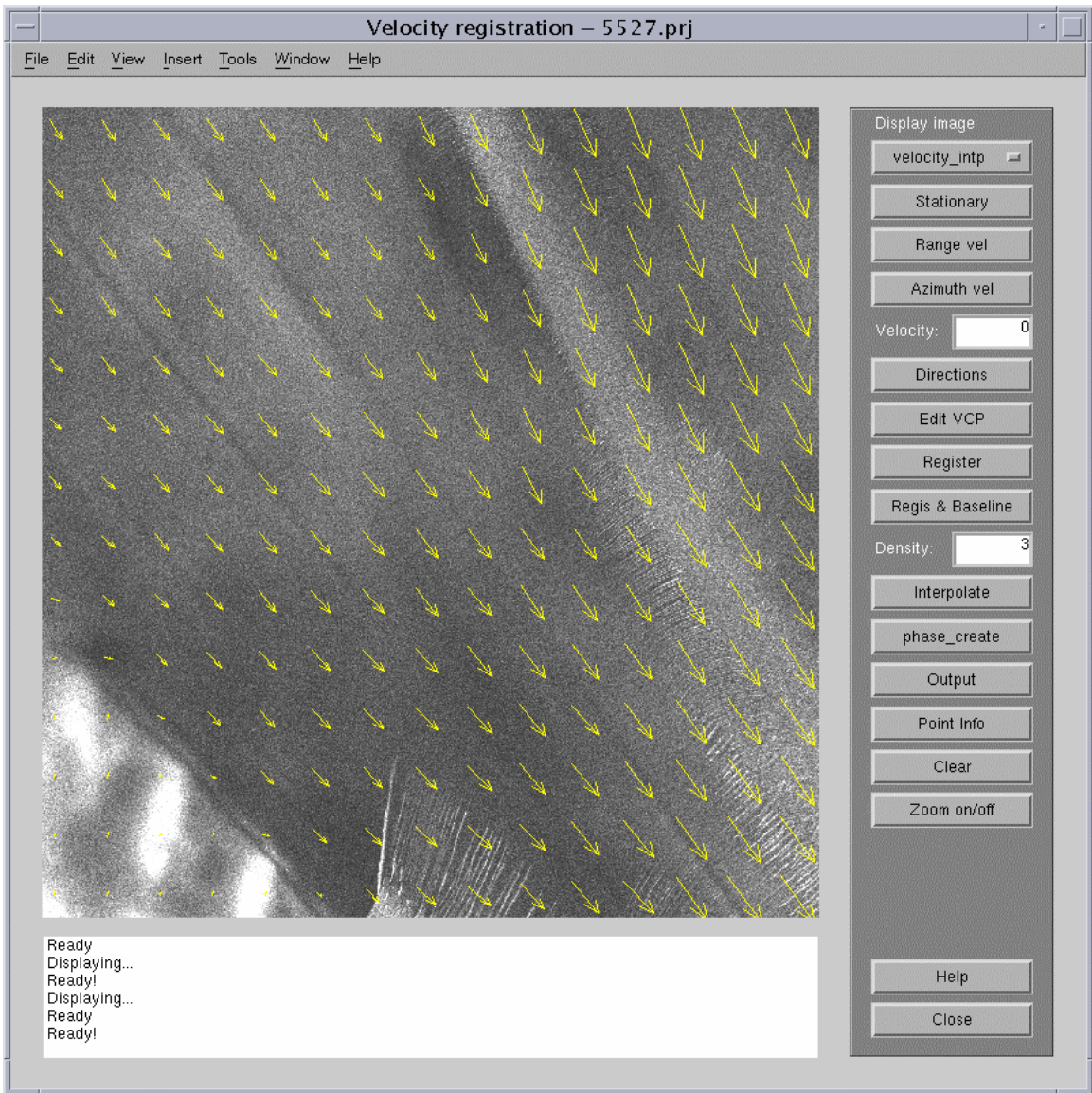


Figure 6.5: Enlarged view of the left bottom corner of the Figure 6.4

6.3 Velocity mosaic of the East Antarctic Ice Streams

6.3.1 Data

There are several AMM-1 InSAR pairs covering the East Antarctic Ice Streams as shown in Figure 6.6. The orbit numbers of the first cycle of the InSAR pairs are 9822, 9851, 9852, 9865, and 9866. All are ascending orbits. Three of them (9822, 9851, 9865) cross the Bailey Glacier, Slessor Glacier, and the Recovery Glacier. Two of them (9852, 9866) pass along the Filchner Ice Shelf. These pairs cover most areas of the Recovery Glacier, the Slessor Glacier, and the Filchner Ice Shelf, to which the two glaciers feed. The data received from the Alaska SAR Facility (ASF) have been cut into frames with a length of 100 km for each frame. There is 10% overlap between frames. The data are valuable not only because they cover the two large glaciers, but also because they extend south 80° latitude where RADARSAT normal mode and other satellites (e.g., ERS 1/2) are unable to reach. Detailed descriptions and characteristics of the data are listed in Table 6.5

Orbit pair	A/D	Mode	# of frames	Incidence angle	Baseline Bn (m)	Baseline Bp (m)	Dates (1997)
9822 10165	A	S7	5	47°	206.3	215.8	9/21 10/15
9851 10194	A	S2	5	27.5°	95.9	196.8	9/23 10/17
9852 10205	A	S2	4	27.5°	93.5	190.1	9/23 10/17
9865 10208	A	S2	5	27.5°	59.5	127.8	9/24 10/18
9866 10209	A	S2	4	27.5°	56.6	122.6	9/24 10/18

Table 6.5: Descriptions of InSAR data of the East Antarctic Ice Streams

In addition to SAR data, a surface elevation model of the Antarctic (Liu, 1999; Jezek, 1999c) and tidal data for Filchner Ice Shelf are used in generating surface velocity. The surface elevation model has a vertical accuracy of 10 meters for the areas of the East Antarctic Ice Streams (Liu, 1999). The tidal data are from a high resolution barotropic tidal model of the Weddell Sea (Robertson and others, 1998; Padman, 2000) at the times of the data acquisitions.

6.3.2 Data processing

As discussed above, to estimate two-dimensional surface velocity from InSAR data, a hybrid scheme of procedures is developed. The scheme includes some interferometric procedures from Vexcel's commercial software package 3dSAR (Vexcel, 1999) and some procedures to implement methods developed in this research. Figure 6.7 shows the diagram of processing for surface velocity calculation of the East Antarctic Ice Streams from Radarsat InSAR data. In the diagram, the shaded boxes represent the data set and the non-shaded boxes represent data processing procedures. The input data for the diagram are two single look complex images (including their orbit information), surface elevation, and tidal information, if the frame is over the ice shelf. The final result is a georeferenced and high-resolution velocity map with information on velocity magnitude and direction. The loop from velocity calibration to flattening is for recalculation of the motion phase after baseline refinement. The diagram does not suggest the processing as a black box system. Rather, the data processing is a complex system involving many procedures and many intermediate data sets. Several procedures, such as velocity calibration, may require interactive operations.

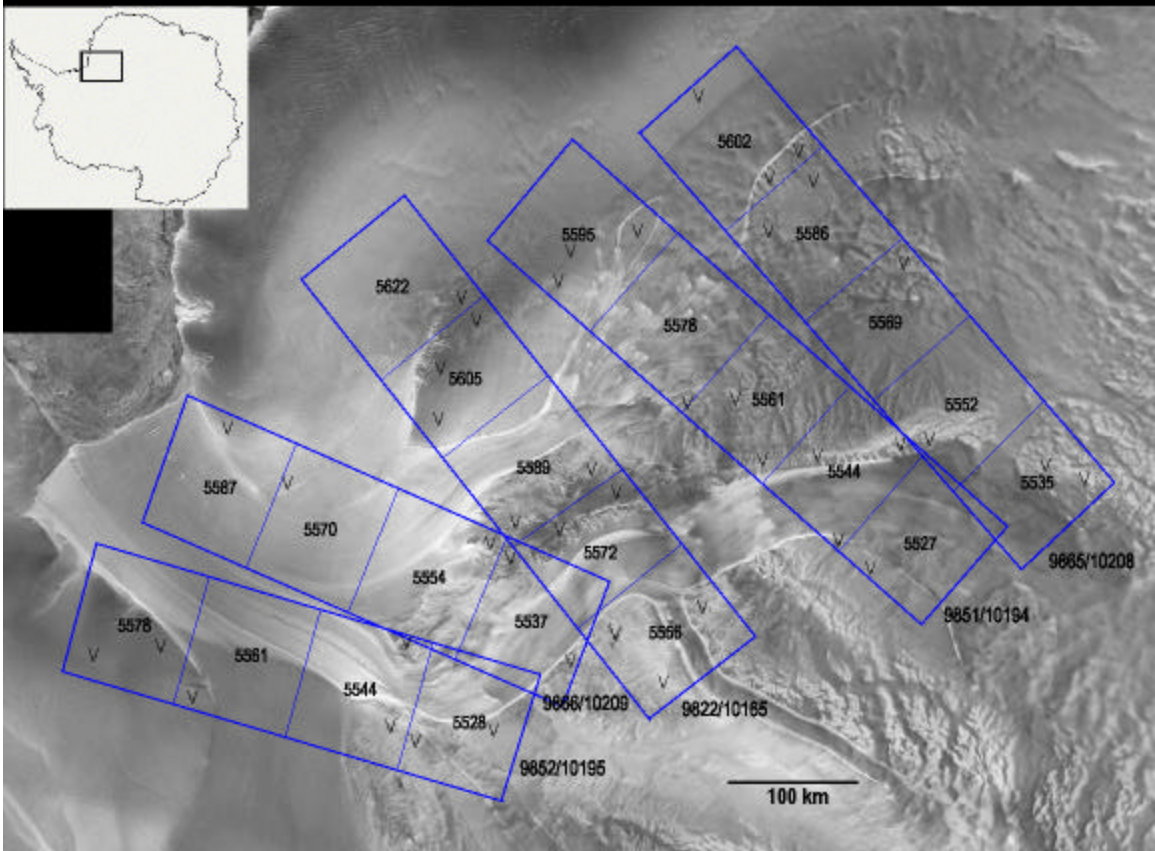


Figure 6.6: Locations of RADARSAT InSAR data used for derivation of surface velocities map of the East Antarctic Ice Streams. Orbit numbers and frame numbers are marked in the figure. Symbols V indicate areas where stationary control points are selected.

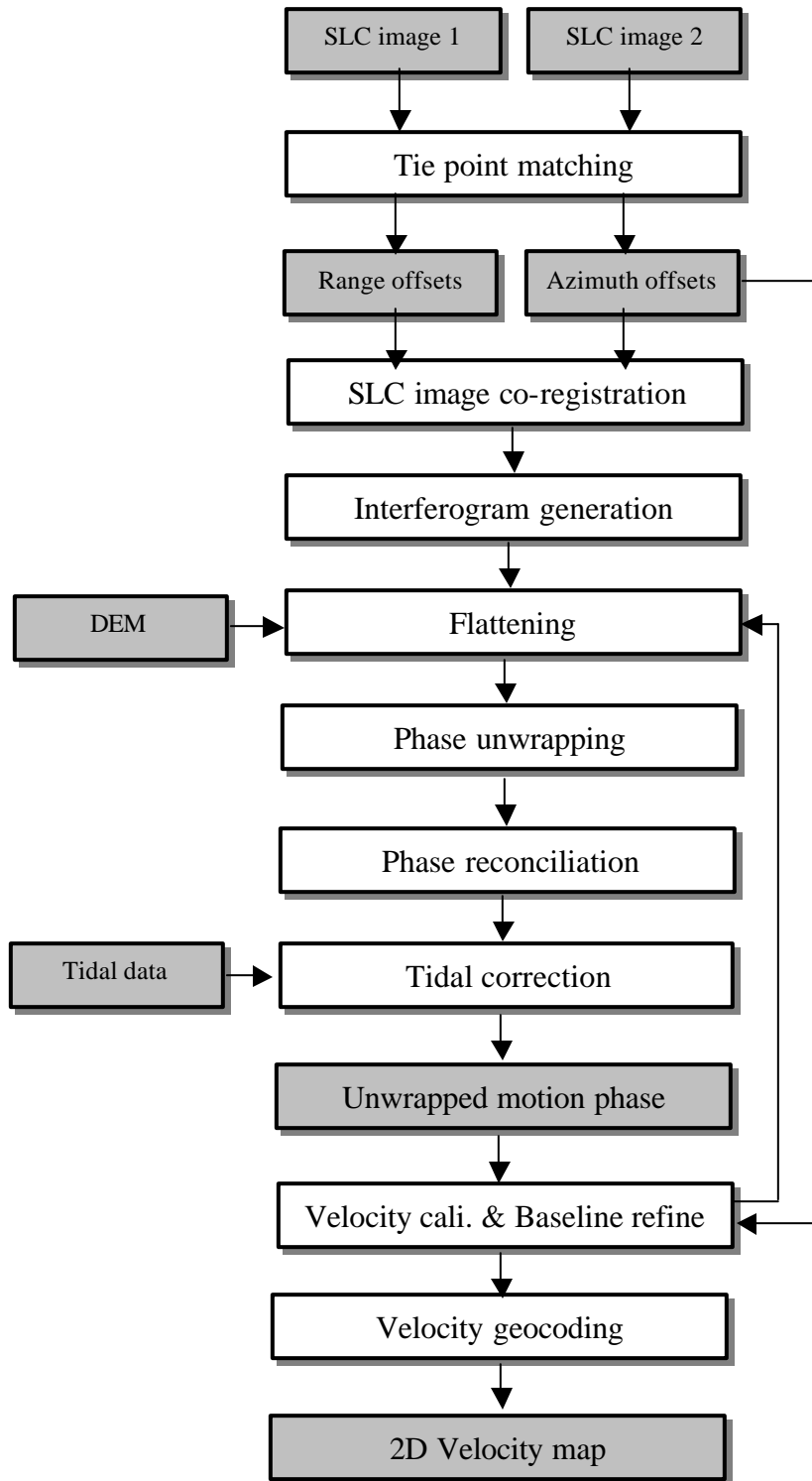


Figure 6.7: Diagram of processing for surface velocity calculation of the East Antarctic Ice Streams from Radarsat InSAR data. The shaded boxes represent data sets and non-shaded boxes represent processings.

Tie point matching from image pair

Tie point matching creates a grid of tie points between the two SLC images. The tie point matching is based on cross-correlation matching on speckle described in Chapter 3. The matching results are range offsets and azimuth offsets of tie points with sub-pixel accuracy on an evenly spaced grid. The initial position prior to matching is determined by state vector data and a surface elevation model, as described in Section 2.3.6. The matching results of range and azimuth offsets will be used by other procedures. SLC image co-registration uses range offsets and azimuth offsets to register two SLC images. Velocity calibration uses azimuth offsets, as well as phase, to generate two-dimensional surface velocity maps.

Create interferogram

The interferogram is formed by conjugate multiplication of two SLC images. Because two SLC images are not perfectly aligned, the second SLC image is co-registered with the first SLC and resampled. The co-registration use a Delaunay triangulation based on local co-registration, as described in Chapter 4. The co-registration method improves the quality of the interferogram. A by-product of this step is the coherence image that is an indicator of the quality of the interferogram.

Interferogram flattening

Interferogram flattening is used to remove the DEM and baseline effects on the interferogram. Phase due to the DEM and baseline is simulated based on the satellite

orbital data and the surface elevation model and subtracted from the measured phase. As a result, the flattened phase is only related to surface motion. A separate phase image for the DEM and baseline is created for later use.

Phase unwrapping and phase reconciliation

Phase unwrapping and phase reconciliation generates an unwrapped phase for the entire frame with the same relative reference phase described in Chapter 5. Goldstein's approach (Goldstein and others, 1988) is used to unwrap individual patches. Phase reconciliation uses range offsets as global guides to adjust the phase of an individual patch. After this step, the unwrapped phase for the entire frame is ready to calculate absolute velocity with only one unknown left that will be determined in the velocity registration.

Tidal correction

If the frame covers areas of floating ice, a tidal correction should be considered. Tidal correction adds an additional phase, caused by elevation differences between the two cycles to the unwrapped phase

$$\Phi_{correction} = \Phi + \frac{4p}{l} \cos \psi (z_2 - z_1) \quad (6.40)$$

where $\Phi_{correction}$ is the phase after tidal correction, ψ is the incidence angle, z_1 and z_2 are the surface elevation at the time of the first and second cycles, respectively. In this research, two swaths of data (9852 and 9866) were processed for tidal corrections.

Velocity calibration

Velocity calibration converts the relative azimuth offsets and range phase into absolute two-dimensional surface velocity. It is designed to solve several unknowns in the azimuth offset model and phase model using velocity control points. The method is described in Section 6.2. A velocity calibration tool implemented in the MATLAB environment is used to select control points, calibrate velocity, interpolate velocity, and view velocity vectors. The interface is shown in Figures 6.3, 6.4, and 6.5. In the main window of the interface, a slant range SAR image is displayed. We can select various types of control points by clicking points on the slant range SAR image shown in the calibration tool. For example, if we want to add a flow direction control point, first click the button 'direction' to select a control type, and then draw a line along the flow stripe to define a flow direction. We can add any type of control points. The 'Register' button will calibrate the velocity using the control points and display the velocity vectors on the SAR image. The 'Output' button will write the velocity result into a file, which contains magnitude and direction for each velocity point. The velocity points are in the slant range coordinate system.

Velocity mosaicking

Velocity mosaicking creates ground range velocity points on a regular grid. This is done by the SAR simulation technique described in Section 2.3.6. For a given point (X,Y,Z) on the ground, its position (r,a) in the slant range image can be found using satellite orbital information. Then the velocity value at (r,a) is assigned value at (X,Y,Z) . The position simulation is based on the SAR model and the Doppler centroid. Every

frame projects the data onto the global coordinate system. For the overlap area between two neighboring frames, a weighted average is used. If the joint adjustment is performed between frames, the difference of velocity between two frames for the overlap area will be very small.

6.3.3 Velocity mosaic

We have generated a surface velocity mosaic of the East Antarctic Ice Streams from the five swaths of InSAR data. Velocity control points are selected from areas marked as V in Figure 6.6. The velocity data are on a regular grid with 200m spacing. The velocity data are represented by a velocity magnitude and angle from the X-axis in the polar stereographic projection. Figure 6.8 shows the surface velocity mosaic in HSV color model in which the velocity magnitude is as hue, SAR image is as intensity and saturation is fixed at 0.9. The velocity vector directions are consistent with flow stripes observed from the SAR image. The speed ranges from near 0 m/year in the interior ice sheet to 1 km/year on the Filchner Ice Shelf. We will discuss the accuracy and the quality of the velocity result in the next section.

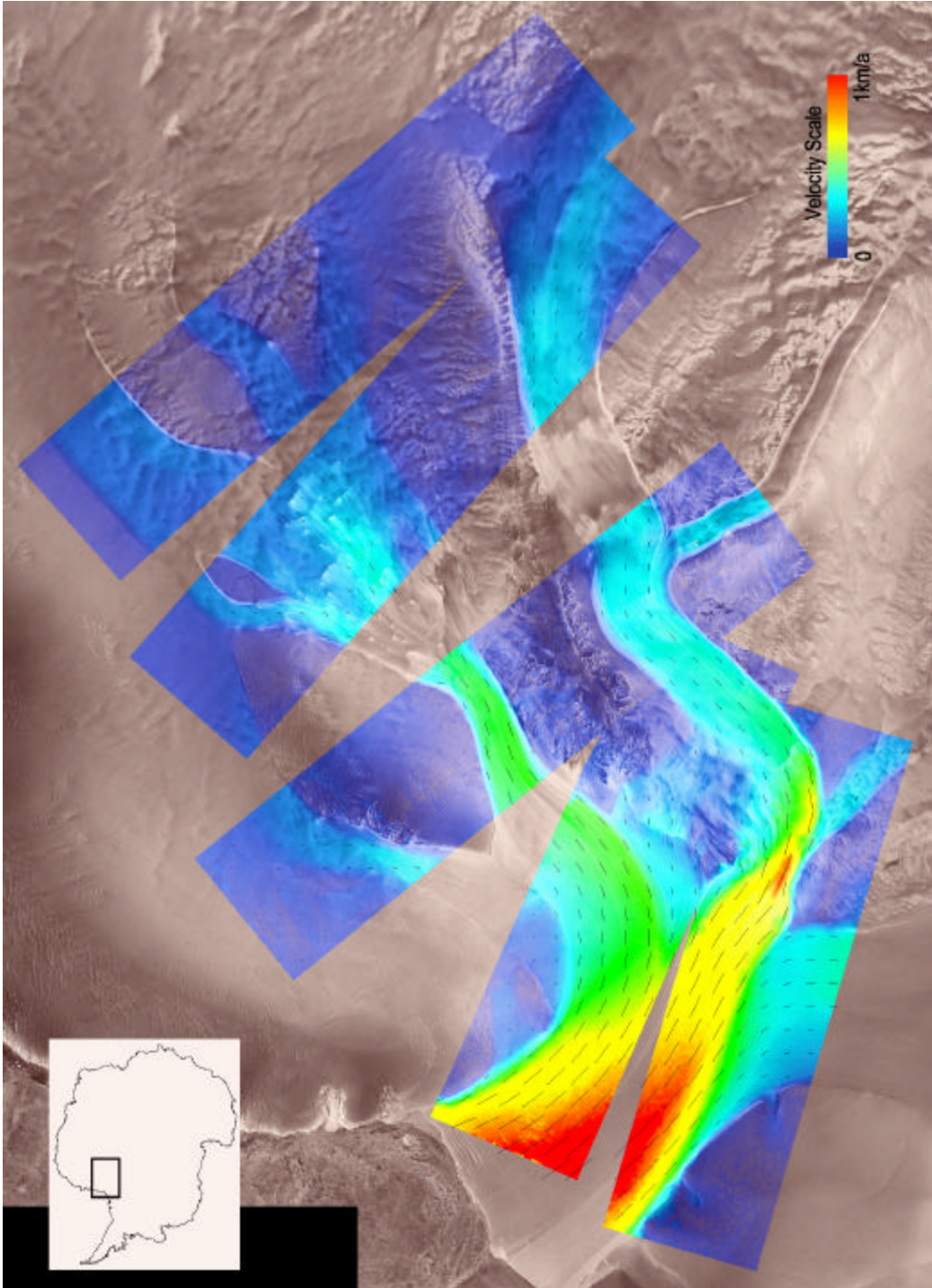


Figure 6.8: Surface velocity mosaic of the east Antarctic Ice Streams. The speed is encoded as hue and SAR is encoded as intensity in the HSV color model

6.4 Error analysis and quality assessment

6.4.1 Error analysis

Errors in the velocity mosaic of the East Antarctic Ice Streams result from several sources and processing procedures. The error sources include random noise in phase and speckle matching, baseline error, and velocity control point error. The velocity is the vector sum of two components in the range and azimuth directions. After calibration, the range motion is calculated by Equation (6.3). The random uncertainty of V_r with phase error is

$$\mathbf{s}_{V_r} = \frac{l}{4pT \sin(\mathbf{b} - \mathbf{a}_r)} \mathbf{s}_\Phi \quad (6.41)$$

The azimuth motion is determined by Equation (6.5). The random uncertainty of V_x with speckle matching error is

$$\mathbf{s}_{V_x} = \frac{Rx}{T \cos \mathbf{a}_x} \mathbf{s}_d \quad (6.42)$$

The systematic errors in V_r and V_x result from inaccurate parameters Φ_0 , a_0 , a_1 , and a_2 determined by velocity control points and the baseline distance estimates. These can be expressed as

$$dV_{r, \Phi_0} = \frac{l}{4pT \sin(\mathbf{b} - \mathbf{a}_r)} d\Phi_0 \quad (6.43)$$

$$dV_{x, a_0} = -\frac{Rx}{T \cos \mathbf{a}_x} da_0 \quad (6.44)$$

$$dV_{x, a_1} = -\frac{rRx}{T \cos \mathbf{a}_x} da_1 \quad (6.45)$$

$$dV_{x, a_2} = -\frac{xRx}{T \cos \mathbf{a}_x} da_2 \quad (6.46)$$

The velocity of a point (r,x) with range component, V_r , and azimuth component, V_x , is represented by magnitude V and its flow angle α with respect to the X axis of the polar stereographic projection of the Antarctic. V and α can be expressed as

$$V = \sqrt{V_r^2 + V_x^2} \quad (6.47)$$

$$\alpha = \alpha_0 + \tan^{-1}\left(\frac{V_r}{V_x}\right) \quad (6.48)$$

where α_0 is the angle of the flight direction with respect to the X axis in the polar stereographic projection. Without losing generality, we assume $\alpha_0 = 0$ in the discussion.

According to error propagation theory, the standard deviation of V is

$$\mathbf{s}_V^2 = \left(\frac{\partial V}{\partial V_r}\right)^2 \mathbf{s}_{V_r}^2 + \left(\frac{\partial V}{\partial V_x}\right)^2 \mathbf{s}_{V_x}^2 \quad (6.49)$$

Using the geometric relationships

$$V_r = V \sin \alpha \quad (6.50)$$

$$V_x = V \cos \alpha \quad (6.51)$$

Equation (6.49) can be rewritten as

$$\mathbf{s}_V^2 = (\sin \alpha)^2 \mathbf{s}_{V_r}^2 + (\cos \alpha)^2 \mathbf{s}_{V_x}^2 \quad (6.52)$$

The standard deviation of V is an ellipse with two axis lengths of σ_{V_r} and σ_{V_x} . The value always varies between σ_{V_r} and σ_{V_x} , depending on the flow direction. Similarly, the standard deviation of flow direction α is given by

$$\mathbf{s}_\alpha^2 = \frac{1}{V^2} (\cos \alpha)^2 \cdot \mathbf{s}_{V_r}^2 + \frac{1}{V^2} (\sin \alpha)^2 \cdot \mathbf{s}_{V_x}^2 \quad (6.53)$$

The direction error of the velocity vector is inversely proportional to the velocity magnitude. When the velocity increases, the direction error decreases. The direction error varies also with flow direction. Given $\sigma_{v_x} > \sigma_{v_r}$, then the minimum direction error is along the flight direction.

There is another type of velocity error related to velocity interpolation. For some areas with high decorrelation, there may be no phase data or speckle matching data. The velocities for these areas are interpolated from surrounding areas. In many cases, the interpolation produces velocities with small additional error. But for areas that are near the edge of the frame, or areas of large size low coherence, interpolation will create a large additional error. This happens on areas near the grounding line of the Recovery Glacier where high decorrelation occurs. The maximum direction error there reaches 25° .

6.4.2 Quality assessment

Visual inspection

Quality assessments are made in several ways to verify the quality of the velocity mosaic. Speed is displayed on the SAR image as shown in Figure 6.8. The change in speed is consistent with glacier regions. Velocity increases when ice moves downstream to the Filchner Ice Shelf and then to the sea.

Comparison of velocity direction with flow stripes is made. We randomly selected 73 points on the Filchner Ice Shelf and the ice streams. We measured the angle difference between the flow stripe on the SAR mosaic and our velocity vectors. The error distribution is shown in Figure 6.9. Figure 6.9 (a) is a plot of error for every point. Most points have an angle error less than 3° . Several points have angle error larger than 5°

caused by poor interpolation of velocity around the grounding line of Recovery Glacier. Figure 6.9 (b) is the histogram of the angle errors. The standard deviation of the error is 2.89° . Our analysis suggests that the angle error on the Filchner Ice Shelf and the three glaciers is better than 5° , except for the grounding area of the Recovery Glacier.

Figure 6.10 is a portion of frame 5554 of orbit 9866/10209 displayed in the velocity calibration tool. In the figure, ice flow directions are quite diverse and the velocity vectors fit the flow stripe very well. If there were larger systematic errors in velocity, it would not fit well anywhere. Ice flows down from the Shackleton Range into the Filchner Ice Shelf. In the left bottom corner, ice comes from the Slessor Glacier. Because the SAR image is slant range, the velocity vectors are also in slant range coordinates.

Figure 6.11 shows velocity vectors displayed on a SAR mosaic in which the SAR image and velocity vectors are orthorectified and terrain corrected. The area is upstream of the Slessor Glacier. There are extensive crevasses in the area and the flow pattern is complex. Our velocity vectors match the flow stripes in the area.

Tidal correction is applied to the two swaths over the Filchner Ice Shelf, 9866 and 9852, using tidal data from Padman and others (1999). Range offsets are compensated for tides using Equation (6.37). Figure 6.12 shows a comparison of the velocity vectors before and after tidal correction. Without tidal correction, the velocity vectors have larger directional errors for areas where motion is slow. After tidal correction, the velocity vectors fit the flow stripe very well, even in the slow motion areas.

Compare with the existing velocity data

Velocities derived in this research are compared with existing velocities that are derived by others. Kim (1999) estimated velocity of 15 points on the Filchner Ice Shelf by tracking crevasses between 1963 DISP images and 1997 RADARSAT SAR. He also compared his result with velocities derived interferometrically by Laurence Gray and others (1998). Table 6.6 is an expanded table from Kim (1999) adding the velocity result derived in this research. The newly added column is labeled as Zhao. The X and Y columns are 1963 polar stereographic coordinates of tracking points. Figure 6.13 shows the locations of the tracking points at time 1997 marked as numbers 1 to 15. The comparison of velocities between Zhao and DISP is shown in Figure 6.14(a). The comparison of velocities between Zhao and Gray is shown in Figure 6.14(b). The error bar used is 15 m/year for our data, 5.8 m/year for DISP (Kim, 1999), and 20 m/year for Gray and others (1998). The velocities derived in this research are 8.5 m/year less than velocity from DISP. We already know one problem that contributes this systematic bias. This is location difference between the two measurements. Velocity value from feature tracking should be assigned to the middle position of the feature on 1963 DISP and 1997 SAR image. But Kim (1999) assigned to the position of feature on 1963 DISP. Take consideration of this factor of location difference, the systematic bias will be further reduced. The Gray velocity is 8.3 m/year higher than velocity from DISP. Since the Gray velocities did not apply tidal correction, they are higher than the true velocity.

Point #	X (m)	Y (m)	DISP (m/a)	Zhao (m/a)	Gray (m/a)
1	-697667	904019	667.8	651.3	664.1
2	-711063	911713	692.6	707.9	702.4
3	-723864	920418	723.6	723.0	739.1
4	-736775	930423	755.6	745.4	767.7
5	-737826	931570	756.0	748.2	767.7
6	-738719	932874	754.3	750.0	770.4
7	-741459	934817	765.3	765.1	772.8
8	-743402	936656	762.5	764.7	780.8
9	-744066	938107	785.3	773.1	787.9
10	-745678	939910	781.8	773.1	787.9
11	-746974	941101	790.8	774.1	789.7
12	-750669	944516	799.2	780.7	807.6
13	-757569	951627	829.5	797.3	825.0
14	-759881	955427	832.4	813.2	836.7
15	-769181	968037	846.9	848.2	869.9
Error			5.8 m/a	15 m/a	20 m/a

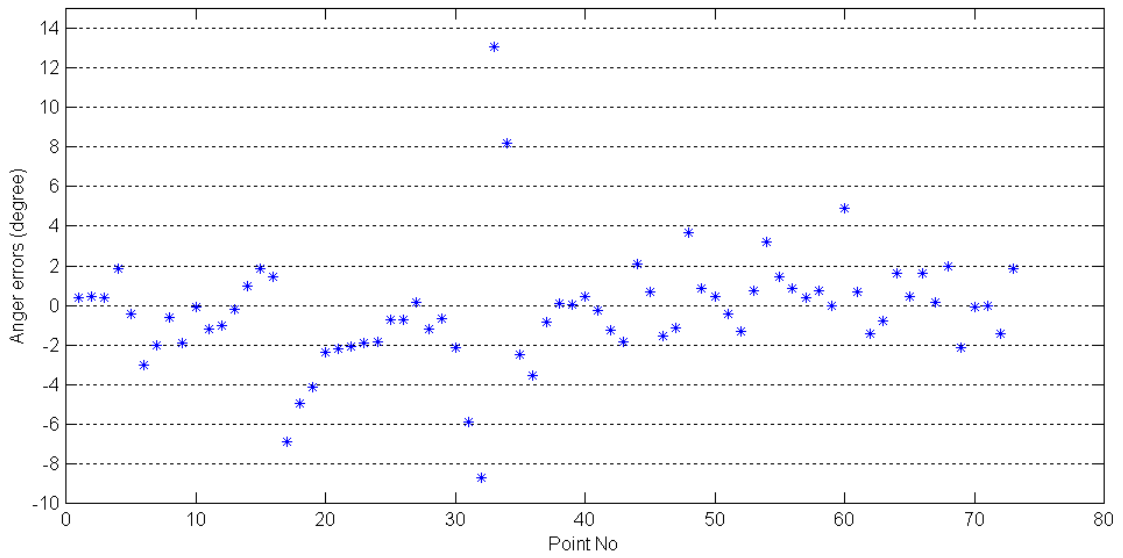
Table 6.6: Velocities on the Filchner Ice Shelf from different sources

There are also velocity data on the Filchner Ice Shelf (locations are shown in Figure 6.13 and marked as A-I) derived by feature tracking from Landsat MSS images of 1986 and ERS-1 SAR images of 1993 (Vaughan and Jonas, 1996). The velocities are compared with velocities derived in this research in Table 6.7 and Figure 6.14 (c).

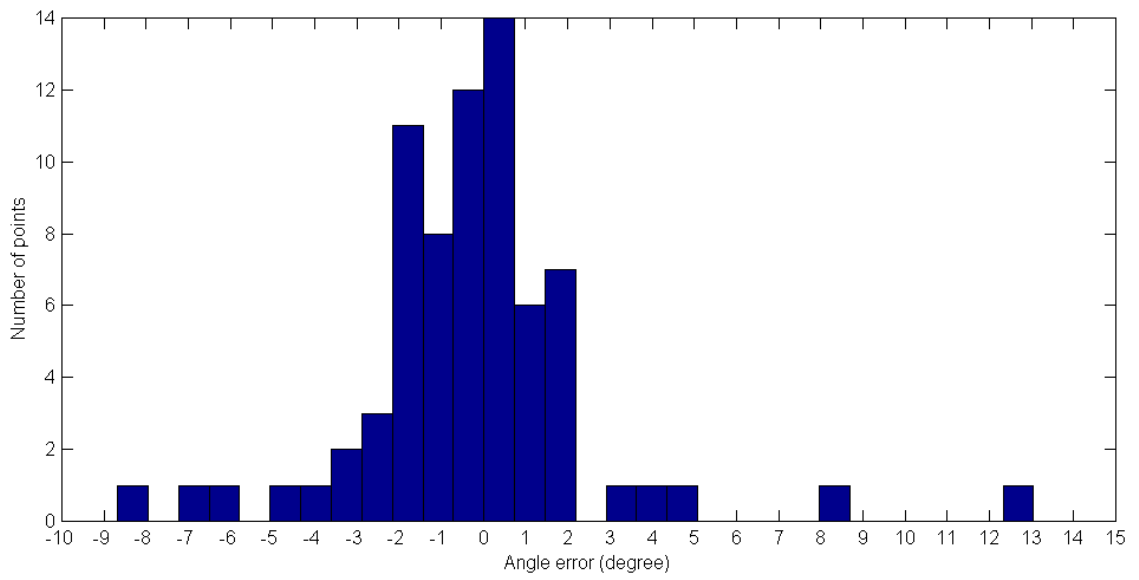
Points	Latitude	Longitude	Vaughan (m/a)	Zhao (m/a)
A	-78.407	-37.184	671.0±36	799.2±15
B	-78.425	-37.193	666.8±36	794.5±15
C	-78.479	-37.242	671.0±36	782.5±15
D	-78.61	-37.314	638.9±36	751.2±15
E	-78.647	-37.322	642.5±36	740.5±15
F	-78.781	-37.3	870.0±36	688.9±15
G	-78.665	-38.413	784.6±36	842.1±15
H	-78.956	-38.335	687.3±36	760.6±15
I	-79.11	-38.24	879.3±36	738.6±15

Table 6.7: Velocities from Vaughan and Jones (1996) and this research

The comparison shows that velocities derived in this research are about 100 m/year less than velocities from Vaughan and others (1996), except for point F and I where there are local peaks. Such peaks do not exist, neither in contours of Figure 6.4 nor in contours from Schmidt and others (1999). The systematic error seems to be caused by independent georeferences of the Landsat MSS mosaic and ERS-1 mosaic (Sievers and others, 1989; Roth and others, 1993). DISP images are registered with the SAR mosaic; only a relative error of registration contributes to velocity error (Kim 1999).



(a)



(b)

Figure 6.9 Velocity angle error distribution

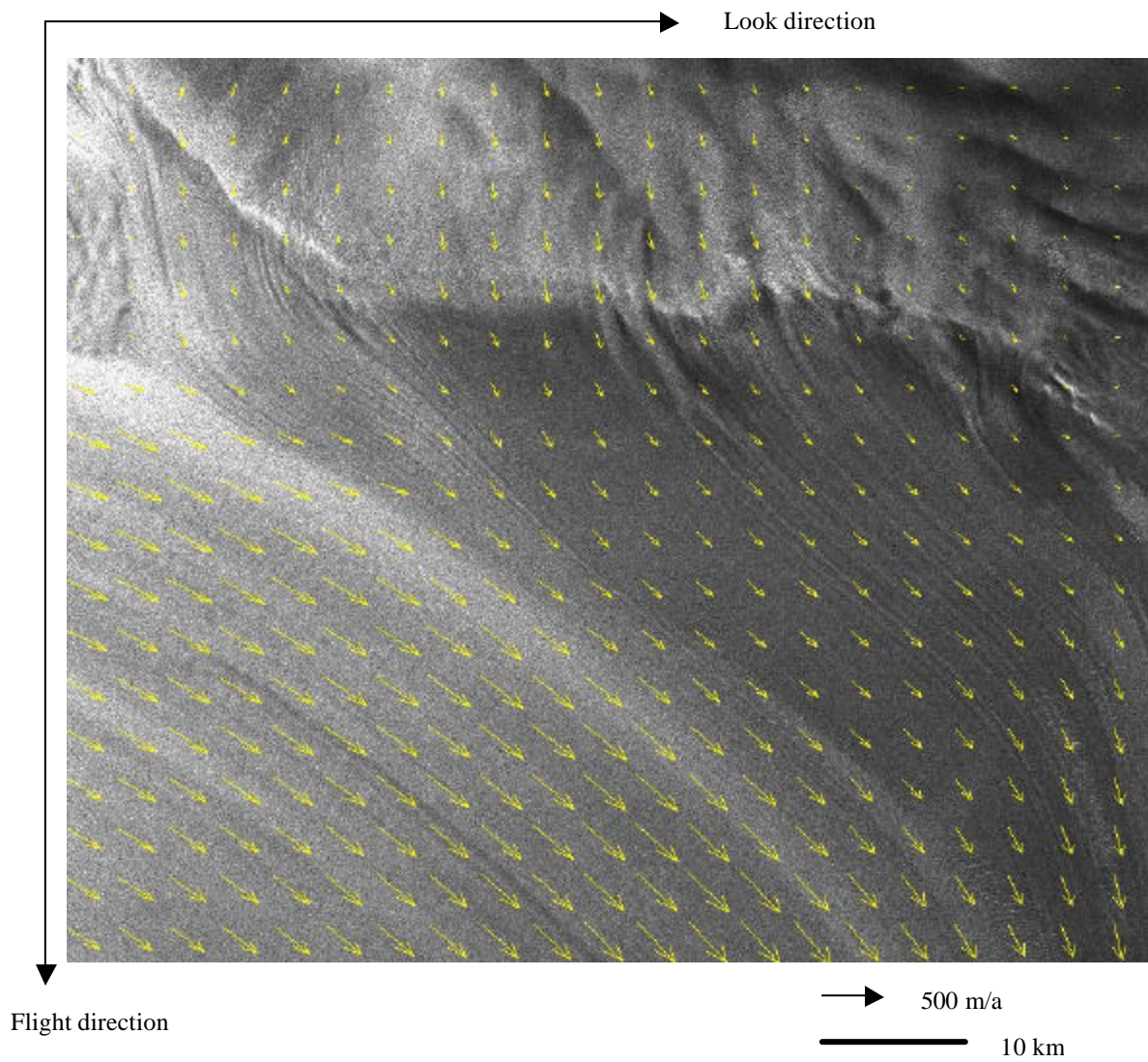


Figure 6.10 Velocity vectors on slant range SAR image. Image center: $33^{\circ}16'$ W, $80^{\circ}26'$ S.

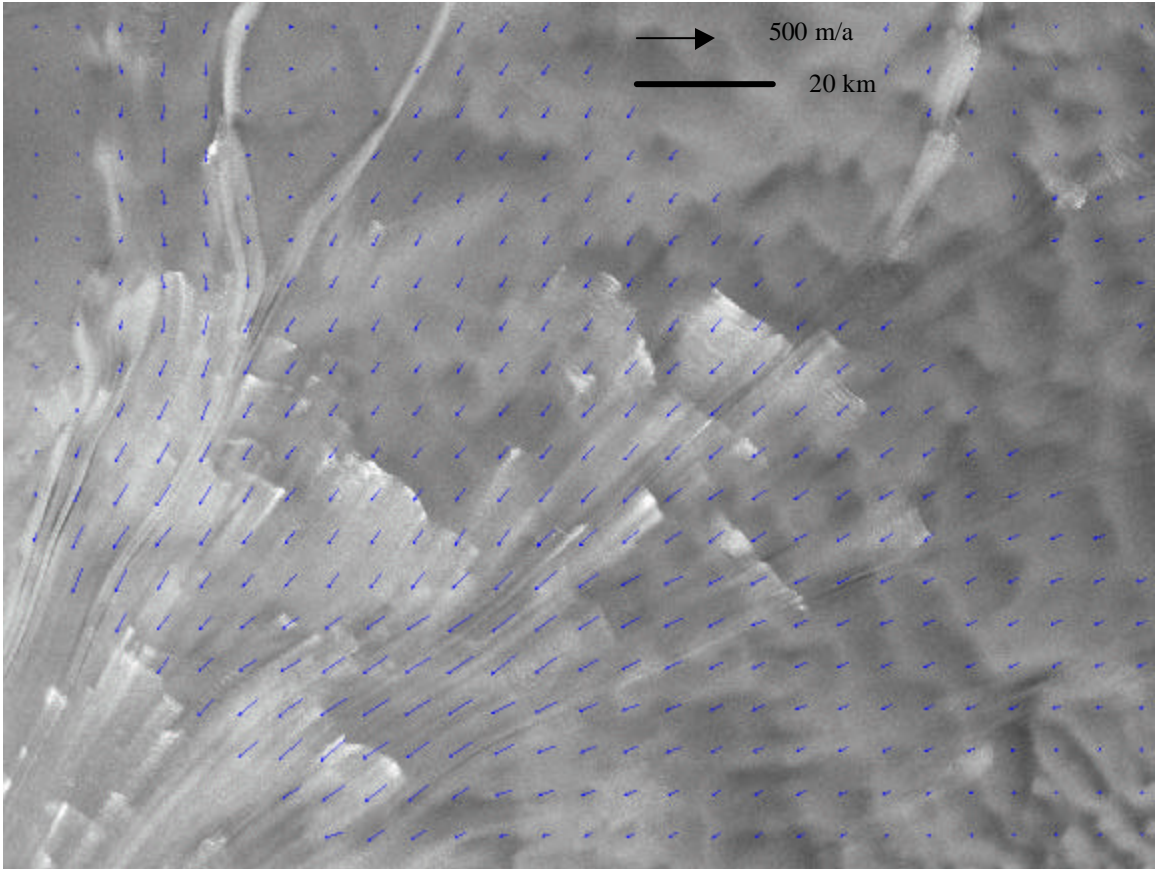
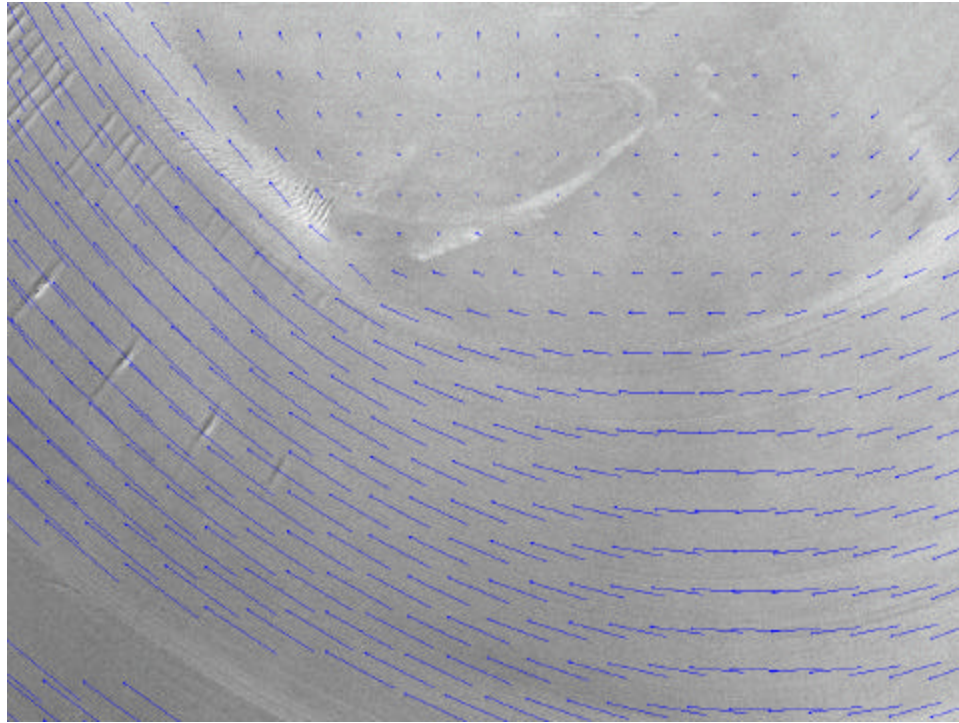
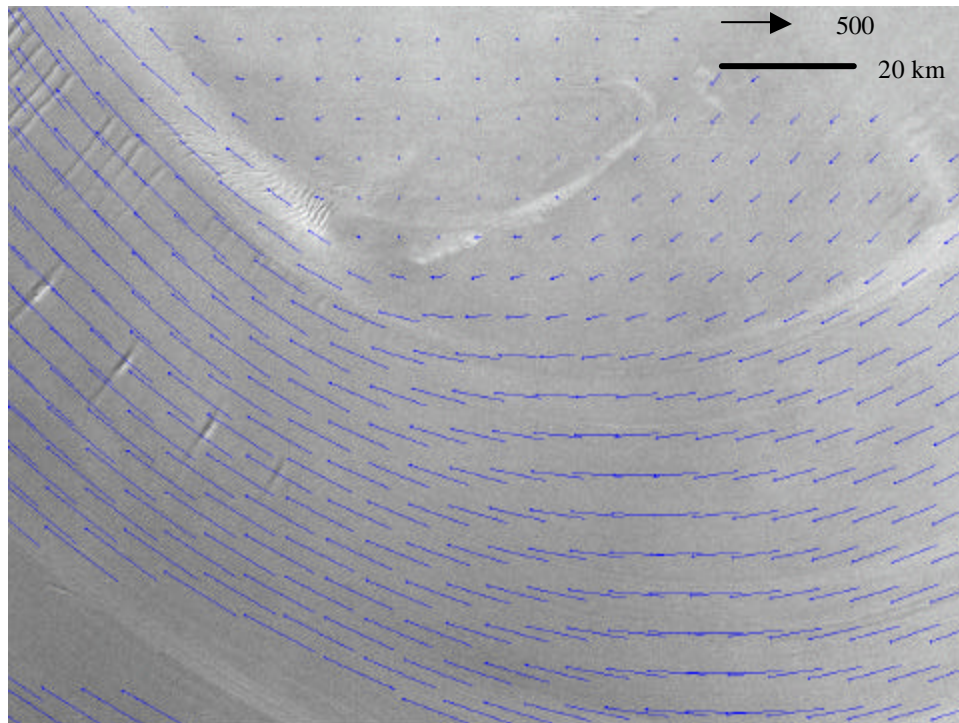


Figure 6.11: Velocity vectors upstream of Slessor Glacier. Image center: 17°41' W, 79°19' S.



(a)



(b)

Figure 6.12 Velocity vectors before tidal correction (a) and after tidal correction (b).
Image center: $35^{\circ}57'$ W, $79^{\circ}30'$ S.

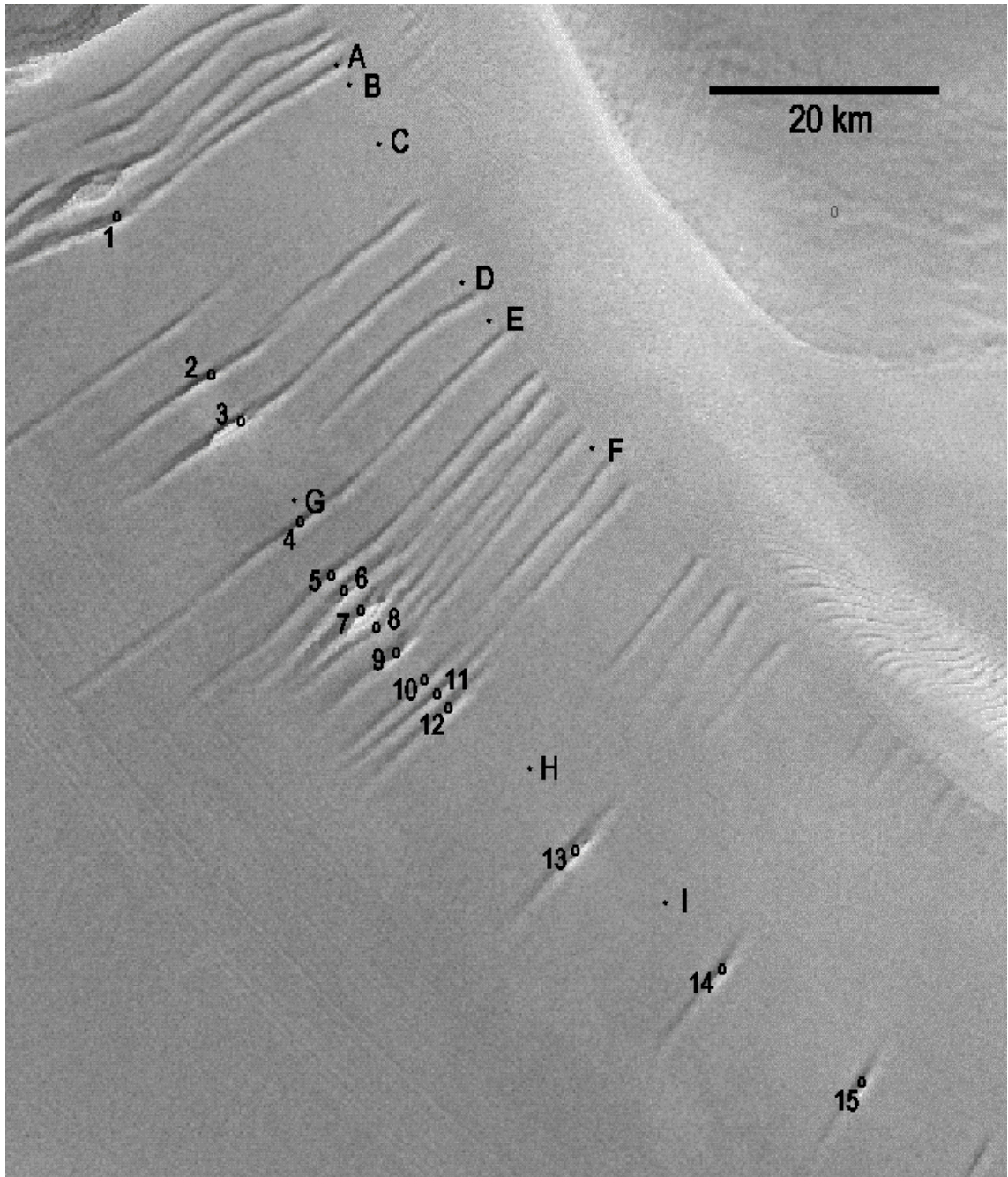


Figure 6.13 Velocity point locations on the Filchner Ice Shelf.

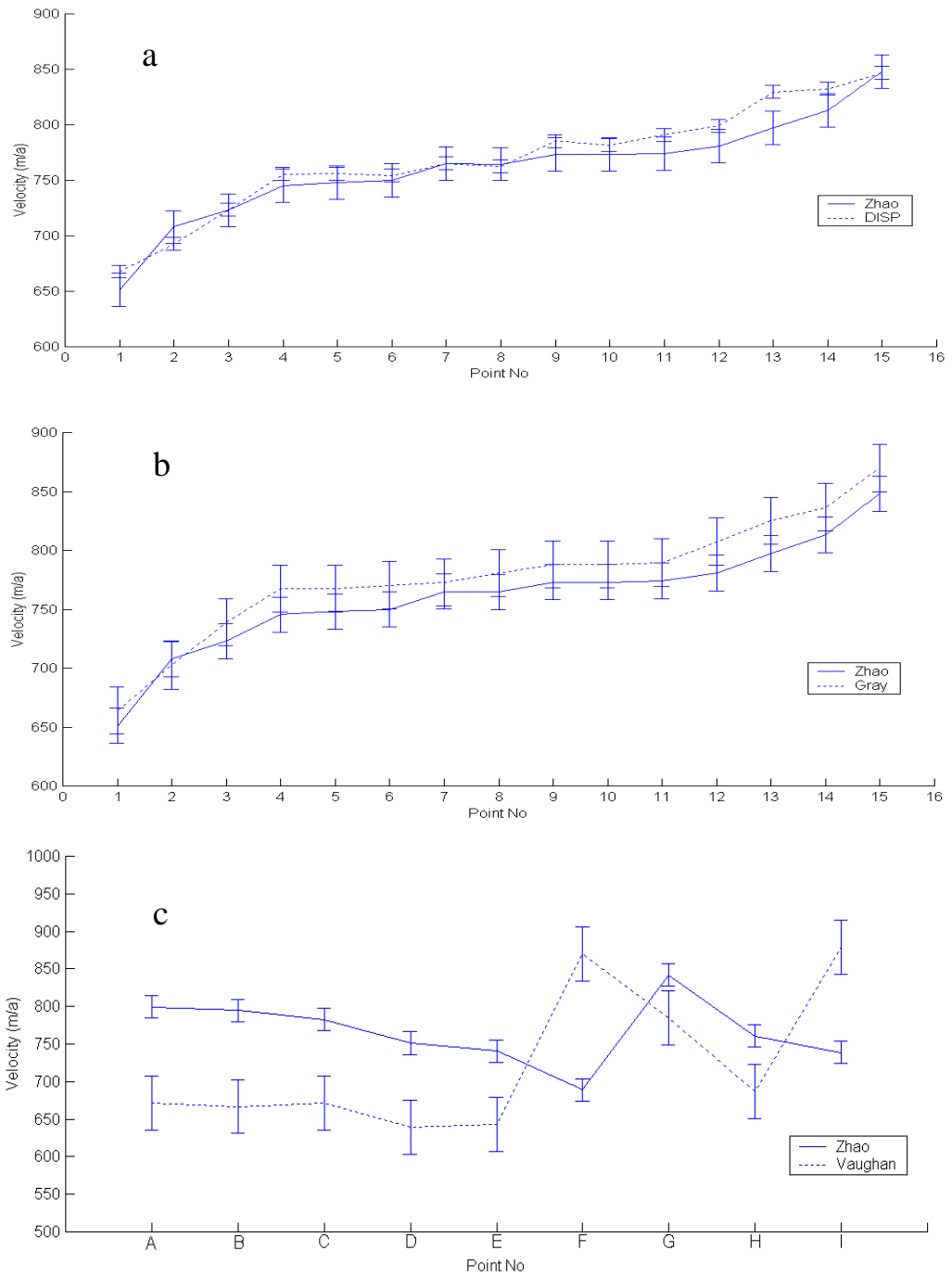


Figure 6.14 Comparison of velocities on the Filchner Ice Shelf

CHAPTER 7

THE EAST ANTARCTIC ICE STREAMS

7.1 Introduction

Ice streams are large rivers of ice that wind through the Antarctic Ice Sheet. Ice streams drain a significant fraction of the ice sheet (Drewry and others, 1982). Ice streams are also important because of their potential role in modulating the response of the ice sheet to climate change. The East Antarctic Ice Streams, including Recovery, Slessor, Bailey and RAMP glaciers form the dominant drainage into the Ronne-Filchner Ice Shelf (Gray and others, 2001). The extent of the East Antarctic Ice Streams range in latitude from 78° to 83°S, and in longitude from 0° to 40°W. The lengths of both the Slessor and Recovery Glacier are more than 1000 km each from the coast to the first indications of streaming flow.

Compared with the West Antarctic Ice Streams, the East Antarctic Ice Streams are far less studied (Hughes, 1975; Bentley, 1987; Bindshadler, 1991). There are many unanswered questions regarding their physical characteristics, flow dynamics, and mass balance. For instance, where are the margins of the East Antarctic Ice Streams? How do the East Antarctic Ice Streams vary in size? How does surface velocity vary across and

down the Antarctic Ice Streams? What is the ice flux through each stream? Are the East Antarctic Ice Streams thinning or thickening? Are the East Antarctic Ice Streams stable?

For the first time a data set is available for systematically studying the East Antarctic Ice Streams. Data acquired during the Radarsat Antarctic Mapping Project (RAMP) provide a continental-scale and high-resolution view of the ice streams (Jezek and others, 1998, Jezek, 1999a). Interferometric data acquired over the East Antarctic Ice Streams provide an unparalleled opportunity to study ice stream dynamics (Forster and others, 1998; Gray and others, 1998). As noted, we have derived surface velocity and coherence maps from the interferometric data. Using these results, as well as other data, we conducted a scientific analysis of ice dynamics and mass balance of the East Antarctic Ice Streams.

In this chapter, we analyze flow patterns and ice dynamics of the East Antarctic Ice Streams. Several new findings are identified. Then mass distribution and mass balance are calculated to study the stability of the ice streams.

7.2 Ice flow dynamics of the East Antarctic Ice Streams

7.2.1 Ice Stream Margins

Ice stream margins are boundaries between fast moving ice and slow moving ice. They provide general knowledge about ice stream geography and help answer questions such as how long and how wide are ice streams? Ice stream margin locations are also important in studying mass balance and ice dynamics. Prior to the RADARSAT-1 Antarctic Mapping Mission (AMM-1) in 1997 (Jezek, 1998), margins of the East Antarctic Ice Streams were not precisely identified. Using the SAR mosaic of Antarctica

produced by the AMM-1 mission, Jezek and Sohn (unpublished) manually extracted shear margins for the East Antarctic Ice Streams, including Bailey Glacier, Recovery Glacier, Slessor Glacier, and two newly discovered twin glaciers called RAMP glacier and Blackwall ice stream. For the most part, shear margins are well delineated by strong radar returns from lateral crevasses. From the SAR imagery, shear zones are normally brighter than the slow motion areas.

Although shear margins can be extracted from the SAR mosaic, the results are less accurate for slow, differential motion areas in the upstream reaches of the glacier. In this research, the coherence mosaic, a by-product of the interferometry process, is used as additional information for shear margin extraction. Coherence is sensitive to differential motion and temporal changes, and provides rich information for shear margin identification. The velocity map is also used in determining shear margins because it provides actual information on how velocity changes laterally across the flow. Using all three data sets, we have identified shear margins of the East Antarctic Ice Streams as shown in Figure 7.1.

In the figure, shear margins are drawn for Bailey Glacier, Slessor Glacier, Recovery Glacier, RAMP Glacier, Blackwall Ice Stream, and the Filchner Ice Shelf. Known features are marked with their names. Arrows indicate flow directions. There are four newly discovered and unnamed features that are respectively labeled A, B, C, and D. Feature A is a small ice rise on the east edge of the Filchner Ice Shelf that diverts the ice from the Bailey Ice Stream and Coats Land. The ice rise will be discussed in detail in Section 7.2.3. Features B, C, and D are three islands of slow moving ice in the upstream portion of the Slessor Glacier. They are associated with high bed topography, and

strongly influence the flow pattern of the ice stream. SFG&FIS indicates that ice in this part of the ice shelf is from the Support Force Glacier (SFG) and Foundation Ice Stream (FIS). In the East Antarctic ice stream system, Slessor and Recovery glaciers are almost parallel and are separated by the Shackleton Range. They flow from east to west, and then turn north where they merge into the Filchner Ice Shelf. The length of these two glaciers is more than 1000 km from the coast to the onset of streaming flow. Recovery Glacier has two, twin tributaries: RAMP Glacier and Blackwall Ice Stream. The twin glaciers have very similar geometrical and physical characteristics.

To demonstrate how powerful coherence is in determining shear margins, the SAR image and the coherence image are compared in the upstream portion of the Slessor Glacier (Figure 7.2). Due to the small differential motion across the shear margin, the SAR image in Figure 7.2 (a) does not clearly capture the contrast between fast and slow motion. In Figure 7.2 (b), the dark line defines the shear margins where ice deformation due to shear motion causes temporal decorrelation.

Controls on Ice Streams

Using AMM-1 estimates of ice stream margin positions, we have compared the location of ice streams with bedrock topography from BEDMAP (Lythe and others, 2000). As shown in Figure 7.3, the positions of the East Antarctic Ice Streams are correlated with topography. The generally convex shape of the East Antarctic Ice Streams coupled with correlation with bedrock topography suggests that these ice streams are more similar in dynamics to Jacobshavn Glacier than to the West Antarctic Ice Streams. That is, the glaciers are fast flowing because of a glaciostatic head funneled

through constricted channels in the glacier bed. This is unlike the WAIS which are fast flowing because of a well-lubricated bed.

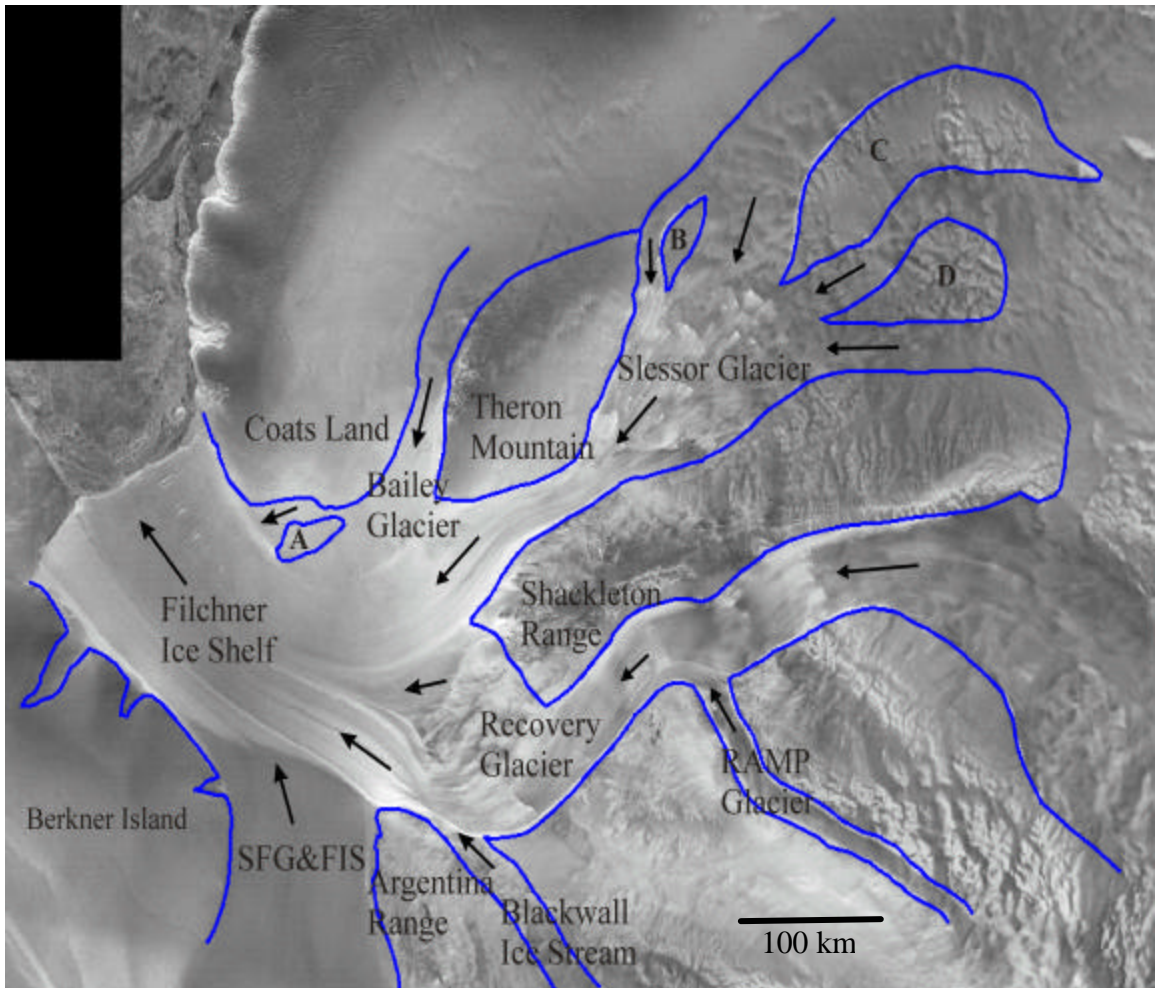
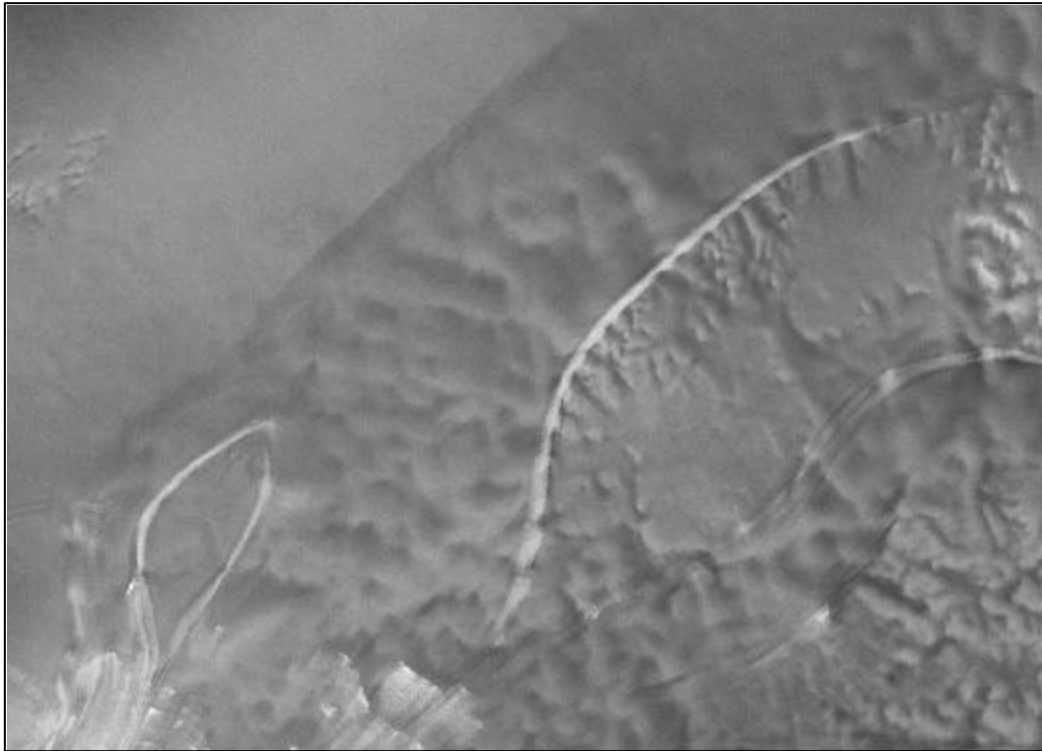
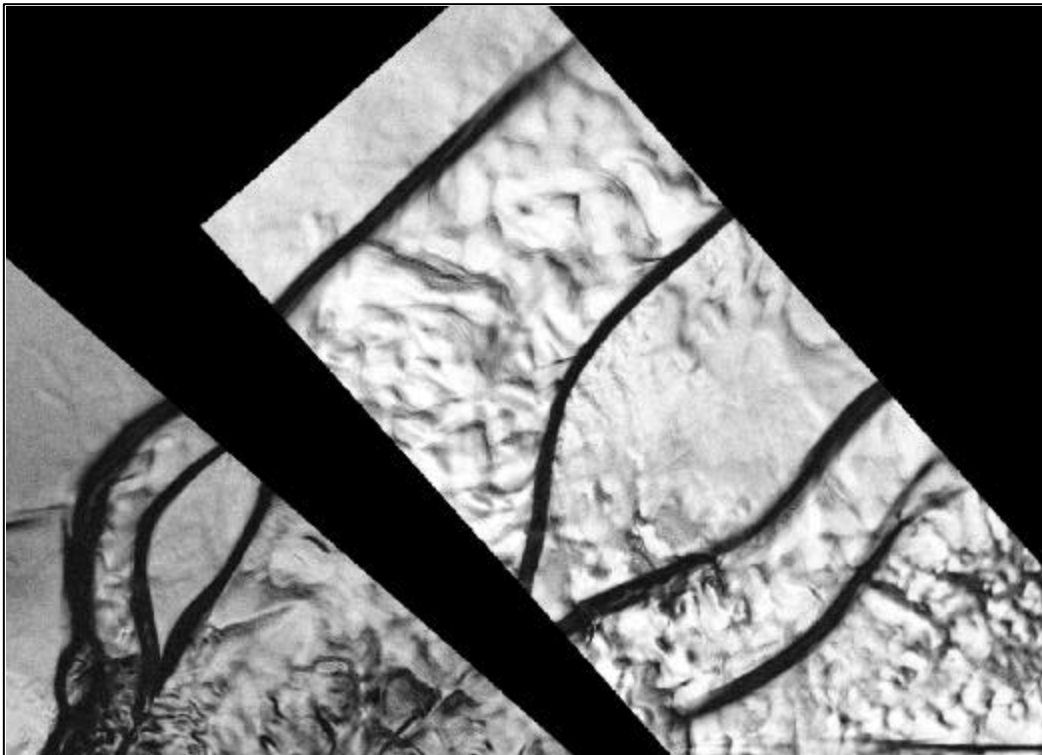


Figure 7.1: Shear margins of the East Antarctic Ice Streams



(a)



(b)

Figure 7.2: Shear margins on SAR image (a) and coherence image (b)

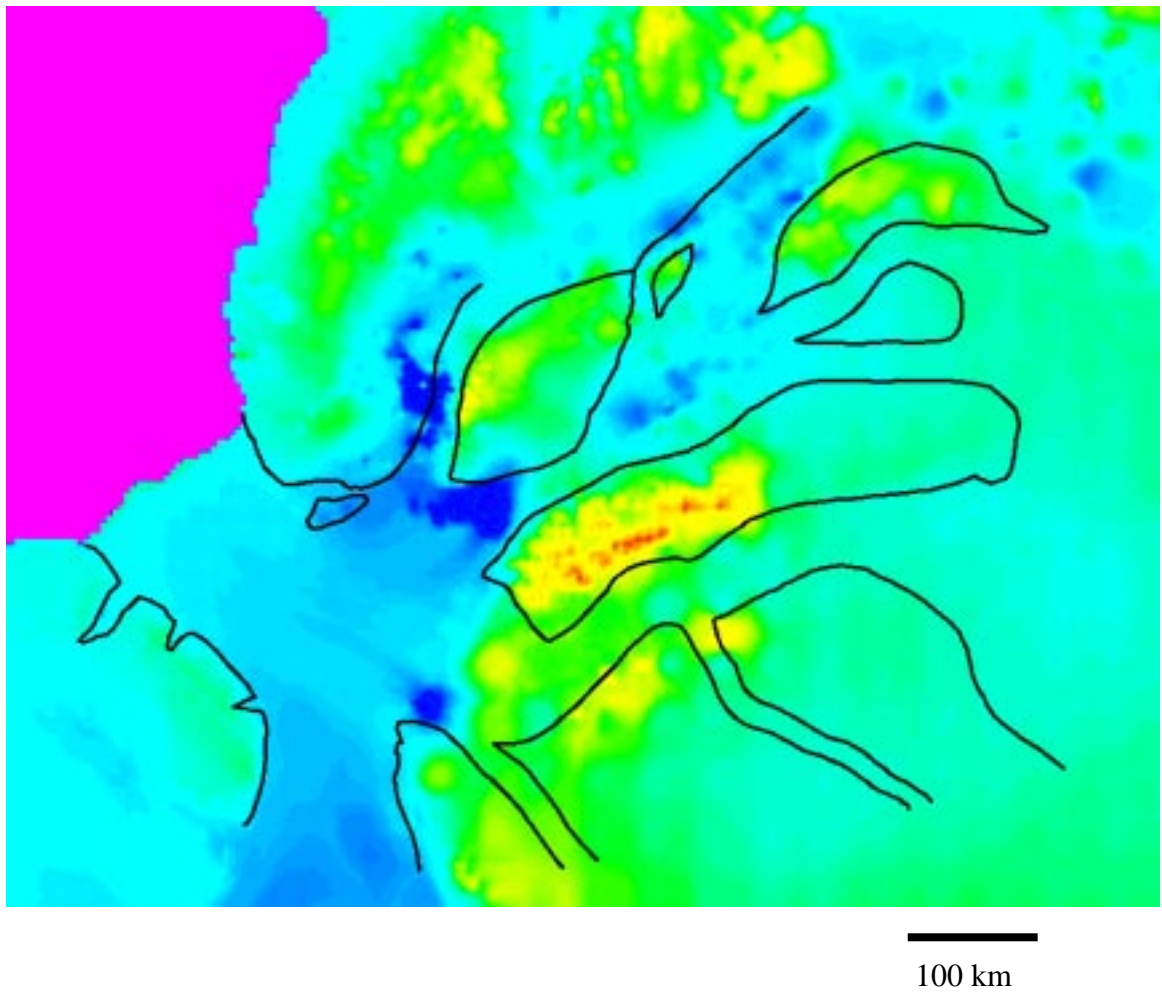


Figure 7.3 Ice stream margins and BEDMAP subglacial topography

7.2.2 Ice flow pattern

East Antarctic Ice Streams surface velocities are shown in Figure 6.8 and reveal flow direction and speed in the region. A more detailed view of flow patterns, velocity contours and longitudinal and cross flow velocity profiles are presented in this section. We also compare these data with profiles of the West Antarctic Ice Streams.

Figure 7.4 shows velocity contours drawn on the SAR image. The contours range from 50 m/year to 1000 m/year with an interval of 50 m/year. Dense contours appear in areas where the Recovery Glacier narrows down and merges into the Filchner Ice Shelf. There is also a local peak in velocity of 900 m/year. The local velocity peak is probably related to the large surface slope and narrow discharge channel around the grounding line of the Recovery Glacier. The contours on the Filchner Ice Shelf indicate that velocity continuously increases when ice moves to the sea through the Filchner Ice Shelf. This finding contradicts that of Vaughan and others (1996) whose result has a local velocity peak near the east side of the Filchner Ice Shelf. Our result also shows that the fastest ice on the Filchner Ice Shelf is associated with Recovery Glacier . outflow, rather than the center line of the Filchner Ice Shelf channel. This finding is consistent with velocity contours derived from ERS-1/2 InSAR over the Filchner Ice Shelf (Schmidt and others, 1999).

We also investigated the longitudinal and cross profiles over the East Antarctic Ice Streams. Figure 7.5 shows the profile locations. Profiles A, B, and C are longitudinal profiles for the Bailey, Slessor, and Recovery glaciers, respectively. Profiles D, E, F are cross profiles on the Filchner Ice Shelf at the downstream, midway, and upstream location respectively. Figure 7.6 shows the longitudinal profiles of the three glaciers. The

solid lines are surface elevation (upper) and bedrock elevation (lower). The dashed line is surface velocity. The breaks in velocity curves are due to the unavailability of InSAR data. The grounding line points are at 280 km, 315 km, 304 km points for the Bailey, Slessor, and Recovery glaciers, respectively.

The convex surface of Bailey and Slessor Glacier restore bedrock topography, which lies below sea level. Velocity is slow until ice merges into the Filchner Ice Shelf. Recovery Glacier has the most complex surface topography, suggestive of a non-equilibrium glacier. Recovery Glacier velocity increases nearly linearly from the 850 km point to the point around 380 km. Near the 300 km point, the velocity reaches a local peak of 900 m/year. On the Filchner Ice Shelf, velocity increases nearly linearly to the coast (Fig. 7.9). The driving stresses for the three parts of the ice shelf are below 10^5 Pa as shown in Figure 7.7.

Figure 7.7 shows three cross profiles at the different locations. Profile D crosses the Filchner Ice Shelf. The left side is from Coats Land and the right side is on Berkner Island. The high velocity segment is associated with floating ice. The velocity peak is around the 180 km point, which is associated with Recovery Glacier. Profiles E and F suggest a good correlation between fast moving ice and bed topography.

We reconstructed the surface elevation for Recovery Glacier from basal stress and ice thickness using profile equations from Paterson (1994). By adjusting basal stress, we fit the calculated surface elevation (the dashed line in Figure 7.8 (a)) to fit the true surface elevation. The basal stress used is shown as a dashed line at the bottom of the figure. The magnitude of the basal stress is shown in Figure 7.8(b). It is compared to the driving stress calculated from the ice thickness and surface elevation. Longitudinal ice

thicknesses down Recovery Glacier are interpolated and may be in error (Lythe, 2000). The surface elevations are also questionable, though comparison of measured flow line and DEM derived flow line is very good (Liu and others, 1999). Consequently, we cannot draw strong conclusions about ice dynamics from Figure 7.8. The peaks in the driving stress and the basal shear stress at 300 and 650 km could be real or could be due to errors in elevation (we think this is unlikely) or errors in bottom topography (very likely). If there are these errors, then the driving stress of every glacier may be more comparable to that found in WAIS.

Bentley (1987) has done a comprehensive review on Antarctic ice streams. He compared profiles of surface and bedrock elevation and driving stress between the East Antarctic Ice Streams and the West Antarctic Ice Streams. West Antarctic Ice Streams have low surface profiles and a small driving stress. It is the lubricated bed that makes Ice Streams B, D, and E move fast. Figure 7.9 (a) shows the profiles for Ice Streams B, D, and E, which are taken from Bentley (1987). Figure 7.9(b) shows profiles of the surface and bedrock elevation and driving stress for the three glaciers of the East Antarctic Ice Streams.

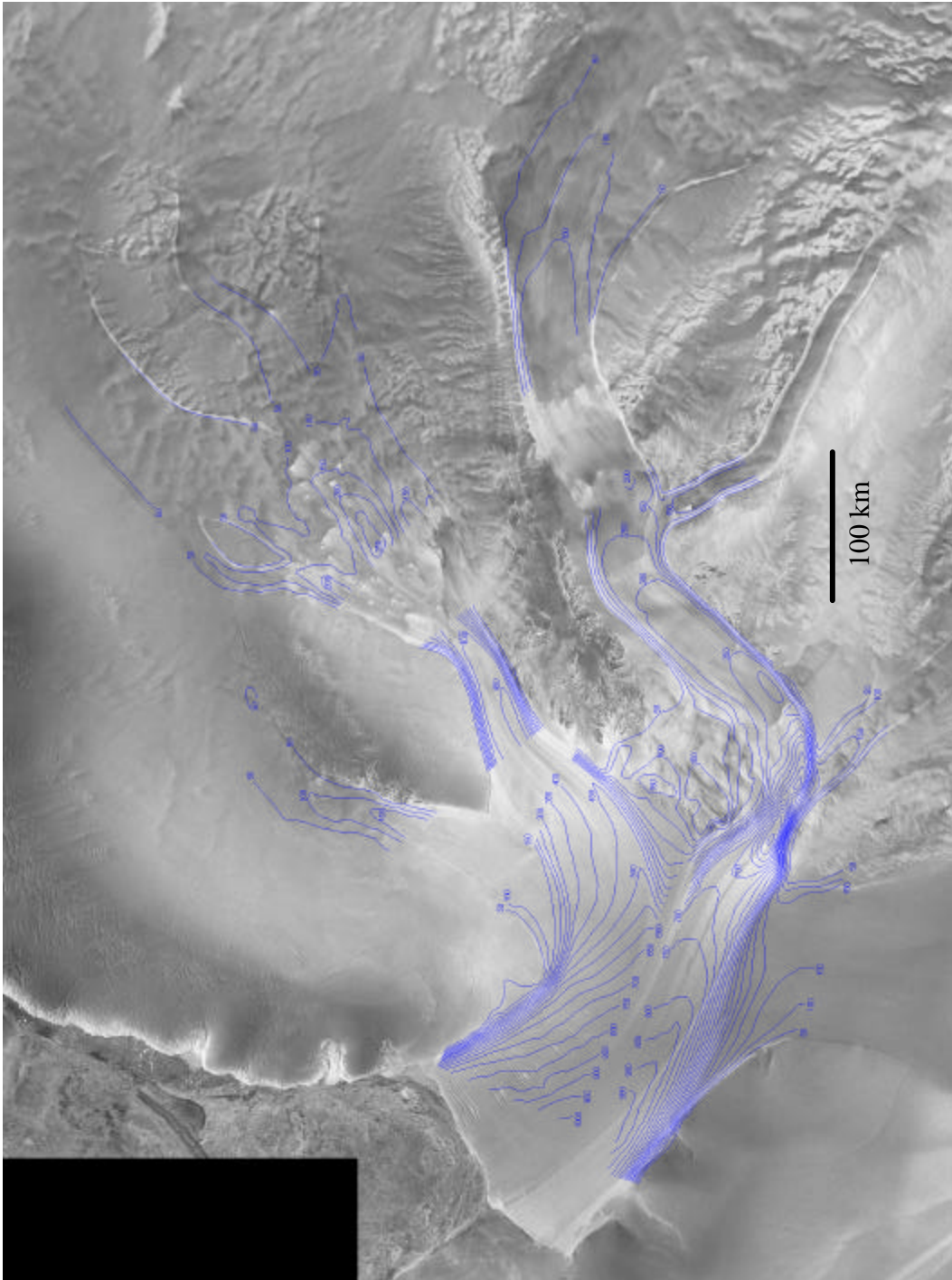


Figure 7.4: Contours of the surface velocity of the East Antarctic Ice Streams

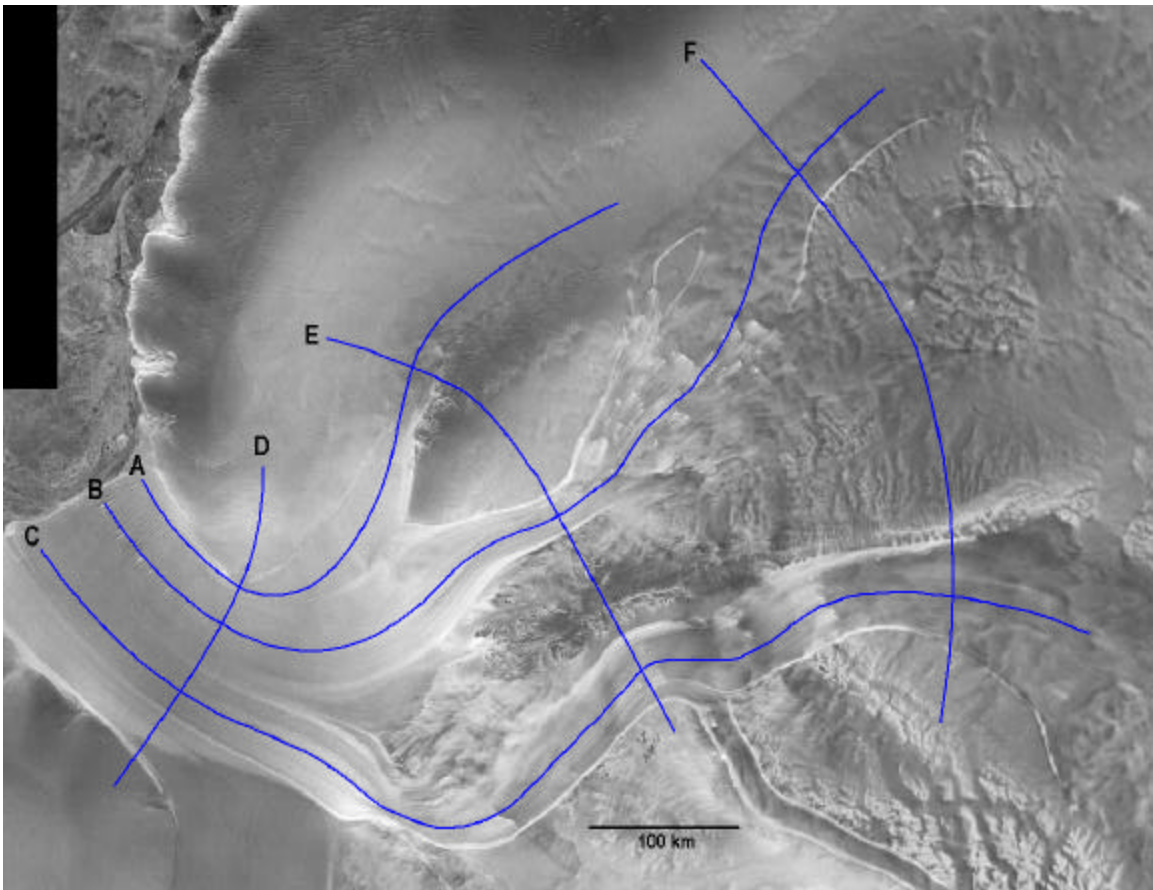


Figure 7.5: Locations of longitudinal and cross profiles over the East Antarctic Ice Streams. Profiles A, B, and C are longitudinal profiles for Bailey, Slessor, and Recovery glaciers, respectively. Profiles D, E, and F are cross profiles on the Filchner Ice Shelf at the downstream, midway, and upstream locations, respectively.

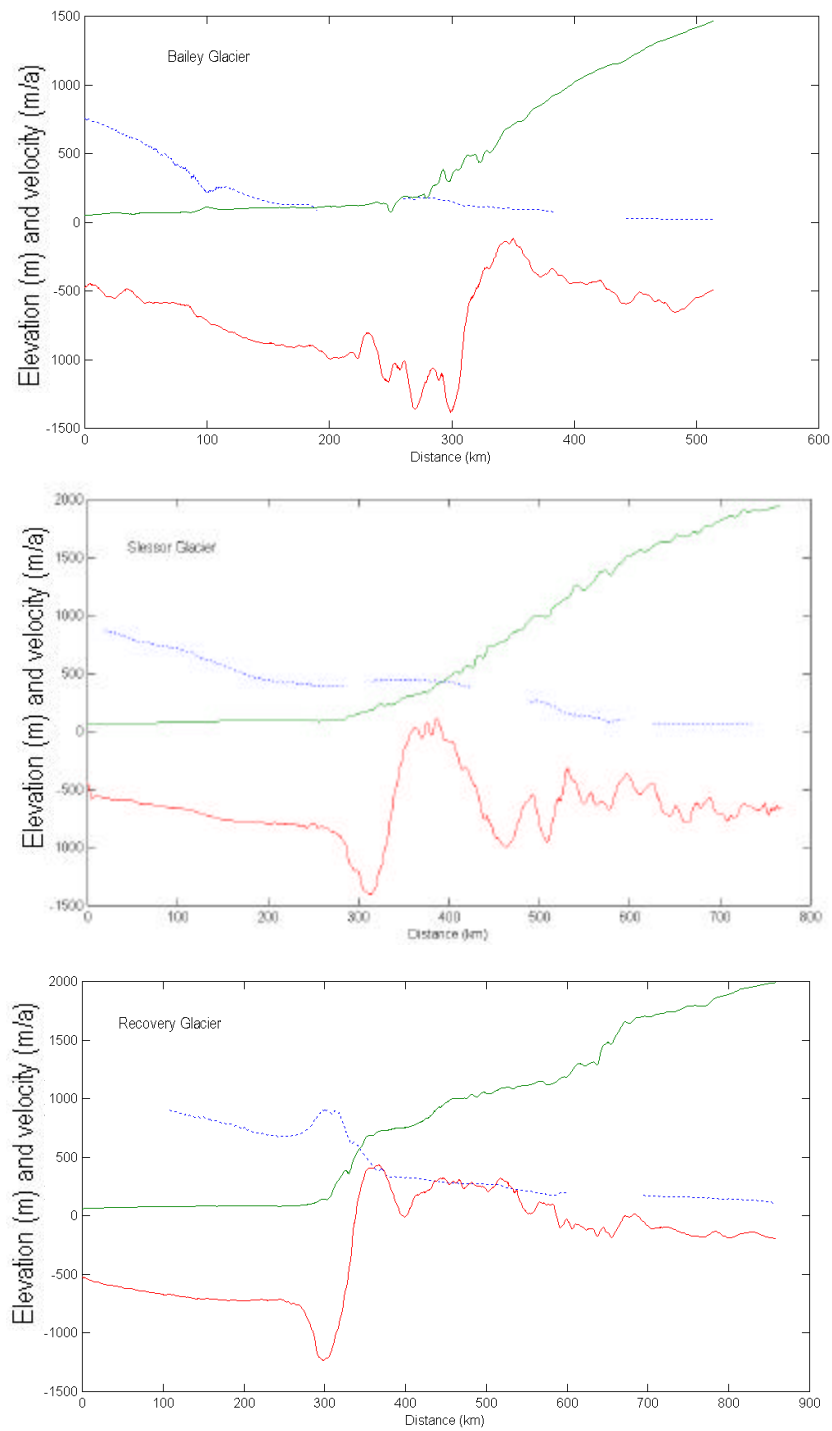


Figure 7.6: Profiles of surface and bedrock elevation and surface velocity for Bailer, Slessor, and Recovery glaciers. Dashed lines are surface velocities. Solid lines are surface elevation (upper line) and bedrock elevation (lower line).

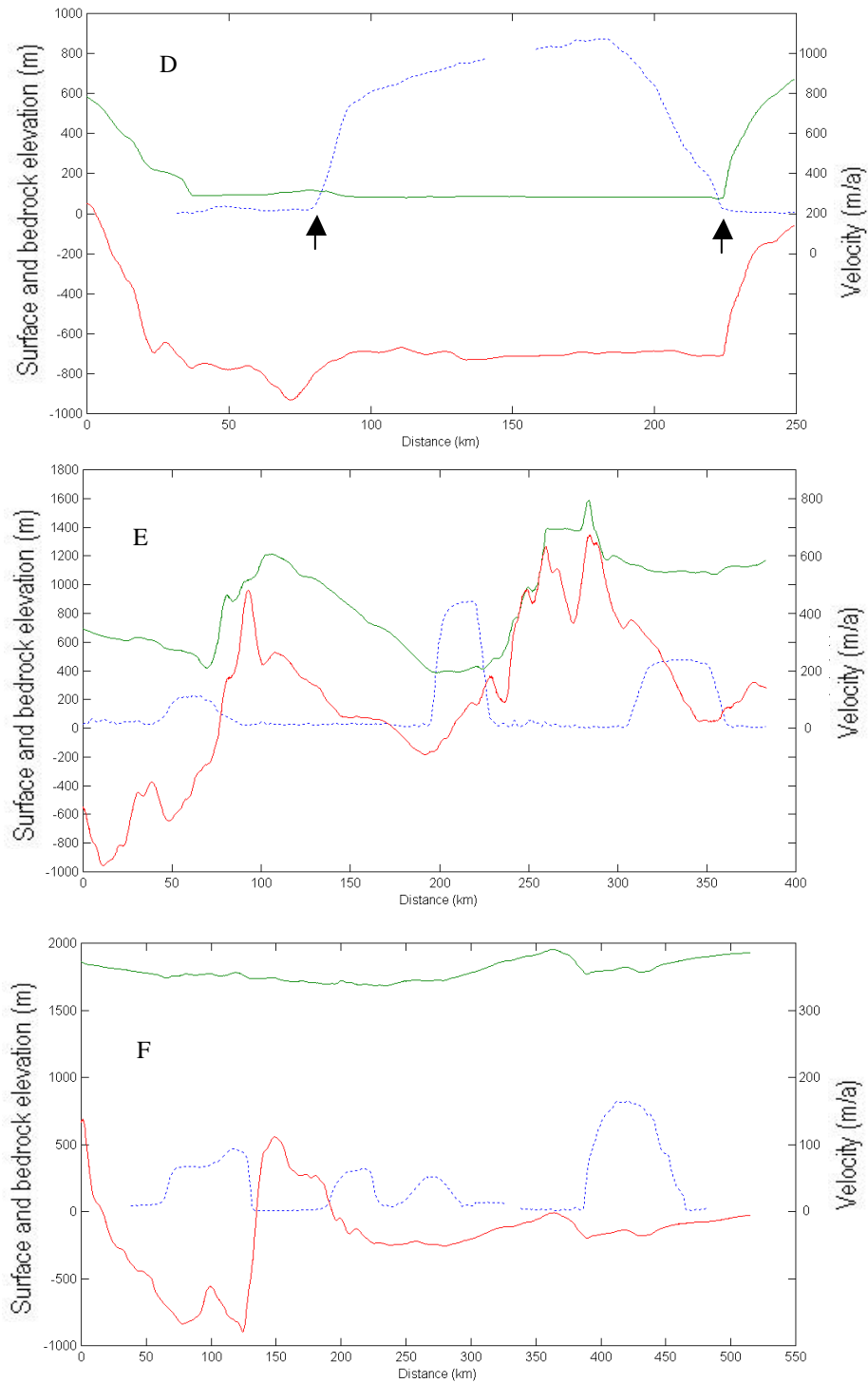
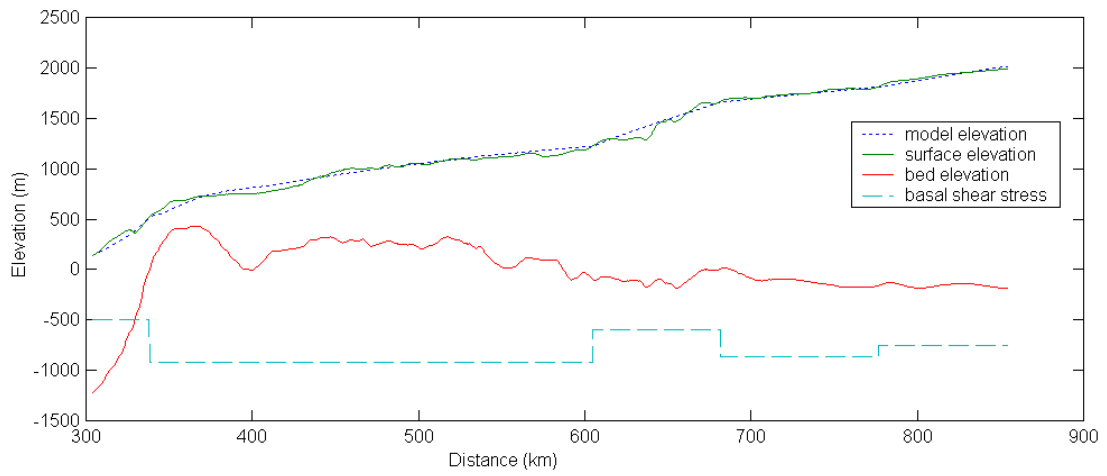
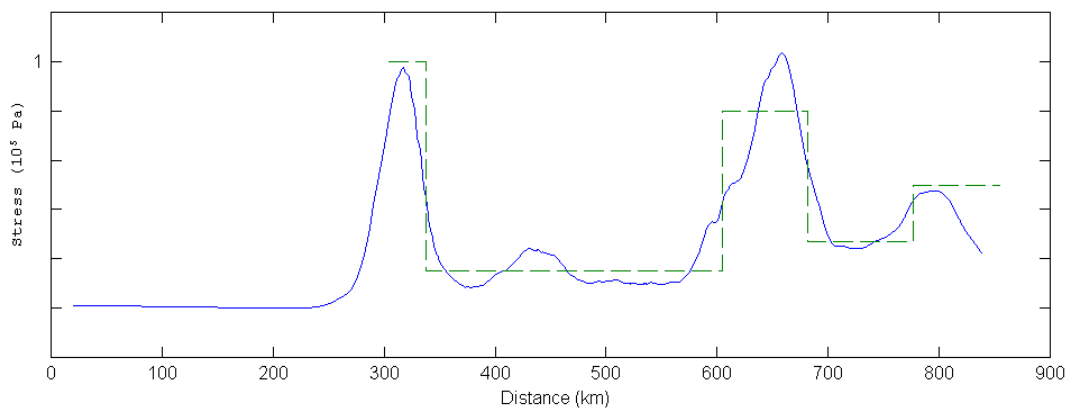


Figure 7.7: Profiles of surface and bed rock elevation and velocity for cross profiles D, E, and F. Dashed lines are surface velocity. Solid lines are surface elevation (upper line) and bed elevation (lower line). The arrows indicate locations of grounding line



(a)



(b)

Figure 7.8: (a) Surface elevation reconstruction and (b) comparison between basal stress (dashed line) and driving stress (solid line).

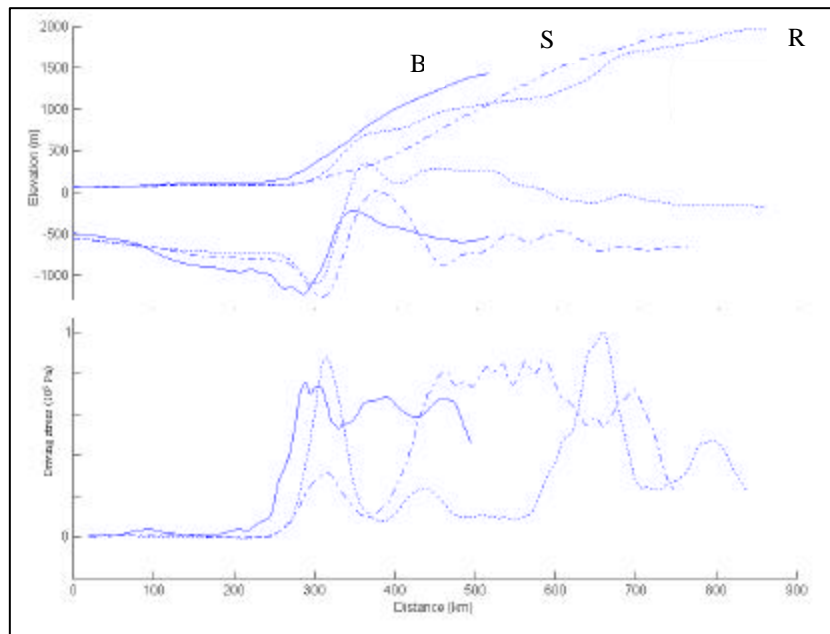
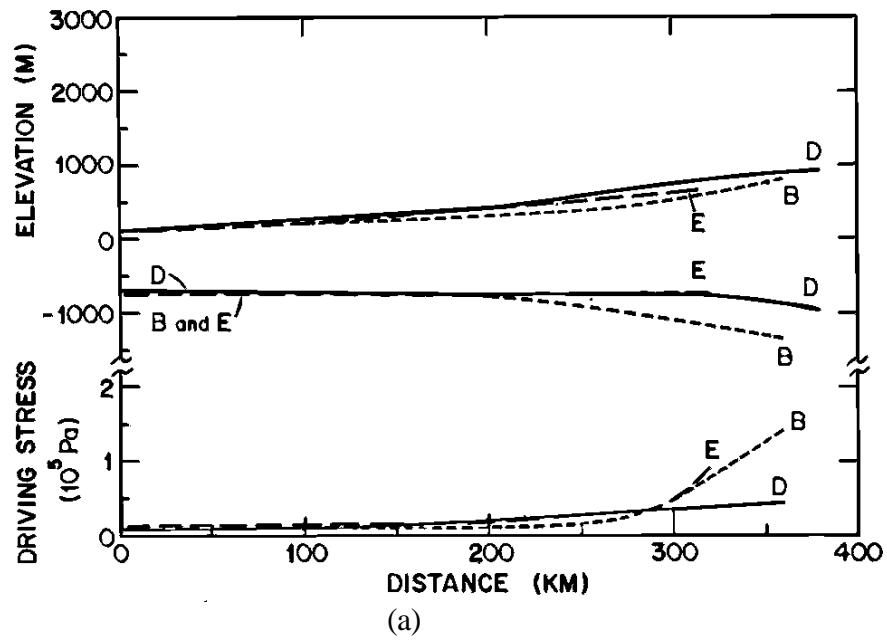


Figure 7.9: Comparison of surface and bedrock elevation and driving stress between WAIS and EAIS. (a) is taken from Bentley (1987) for WAIS; (b) is from the East Antarctic Ice Streams in this study.

7.2.3 Grounding lines and ice rise

The grounding line is a transition area that separates inland ice from the ice shelf. On the ice shelf, ice floats on water. The grounding line may change horizontally due to thinning or thickening of the ice sheet. So the migration of the grounding line is an indicator of mass balance and ice dynamics of the ice sheet (Herzfeld, 1994).

The grounding line can be identified from interferometric SAR processing (Goldstein and others, 1993; Rignot, 1996). Due to the vertical movement of floating ice and differential movement horizontally between grounded ice and floating ice, interferometric fringes change sharply with a high gradient. Fringes are lost or abrupt, coherence is very low at grounding lines. Based on the interferogram and coherence, we have identified the grounding line around the Filchner Ice Shelf. The grounding lines are also confirmed by hydrostatic relationship between ice thickness and surface elevation. In Figure 7.10, the solid lines are grounding lines derived from this research. The grounding lines are broken because of the unavailability of InSAR data. We have compared our grounding lines with previously determined grounding lines from the Antarctic Digital Database (BAS, 1998). ADD grounding lines for that area are extracted from Landsat imagery by human interpretation based on image tone or surface slope. The comparison shows that our grounding lines are consistent with the ADD grounding line, except in the area of Slessor Glacier and Bailey Glacier. In these two glaciers, ADD grounding lines go further inland than our grounding line. We believe that the area between our grounding line and the ADD grounding line in the Bailey and Slessor glaciers area is a large grounded zone that just touches the bedrock.

The isolated, enclosed grounding line near the east edge of the Filchner Ice Shelf indicates a small ice rise marked as A in Figure 7.11. This ice rise does not exist in the ADD database. The ice rise is very hard to detect from SAR images or optical images, because the surface elevation and tone are almost identical with its surrounding area. Interferometry detects the differential motion of the surrounding ice and also shows abrupt vertical movement at the grounding zone due to the tidal force. Figure 7.11 is the ice rise on the SAR and coherence images. The geometric center location of the ice rise is at 35°19'W, 79°15'S. The ice rise length is 55 km and the maximum width is 23 km. The area of the ice rise is 870 km². Figure 7.12 shows the interferometric fringes after removing for the baseline and topography. The fringes are solely related to surface motion in the range direction. On the ice rise the fringes are very sparse due to very slow motion on the ice rise. The fringes change abruptly at the grounding line. The bull-eye shape fringes are caused by vertical movement when the ice flows over a bump (Rignot and others, 1995). The existence of this ice rise has influence on the ice dynamics and mass balance of the Bailey Glacier.

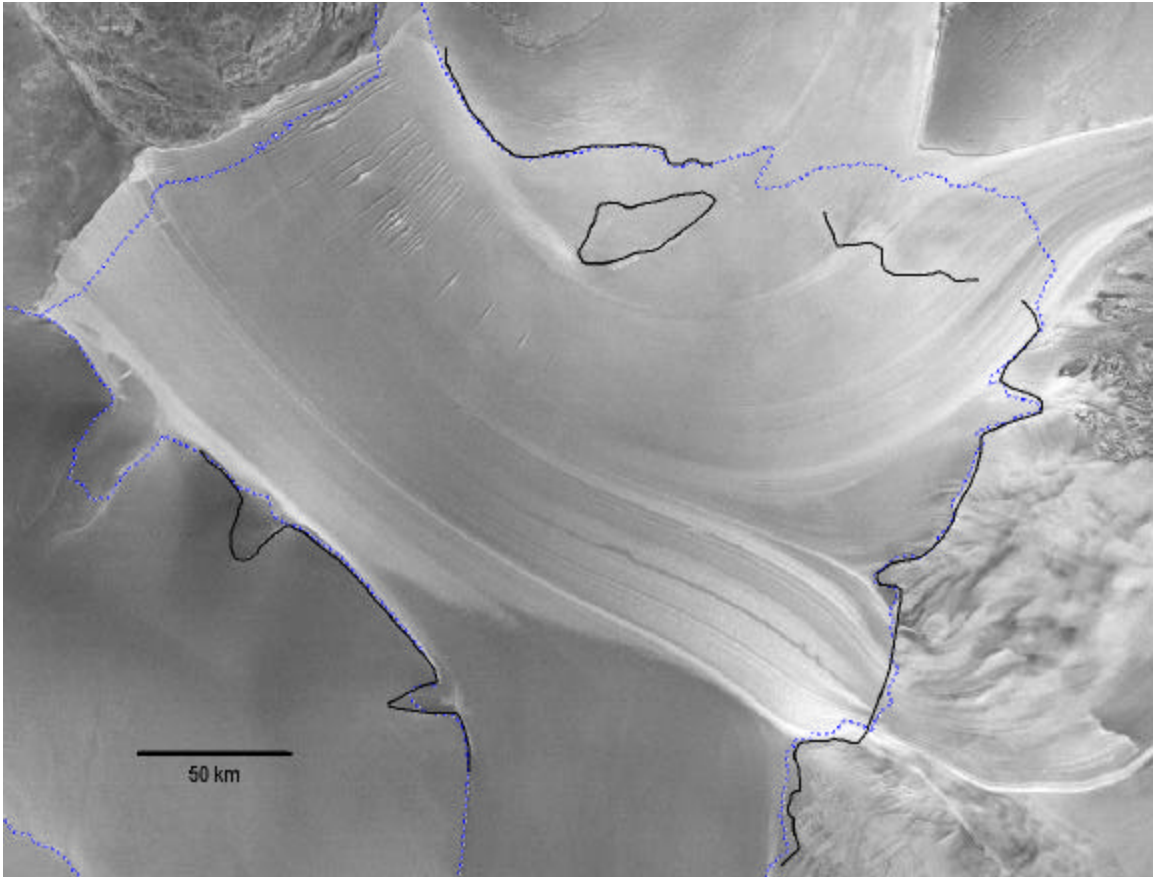


Figure 7.10: Comparison of grounding lines from interferometry (solid line) and from the ADD database (dashed line).

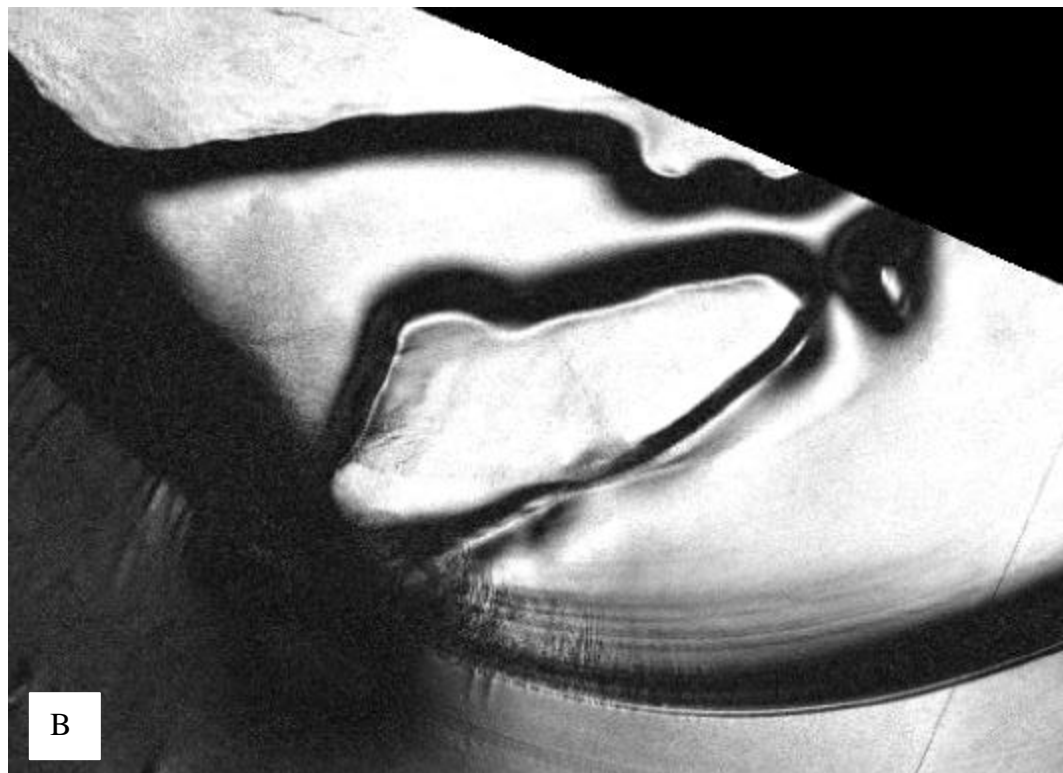
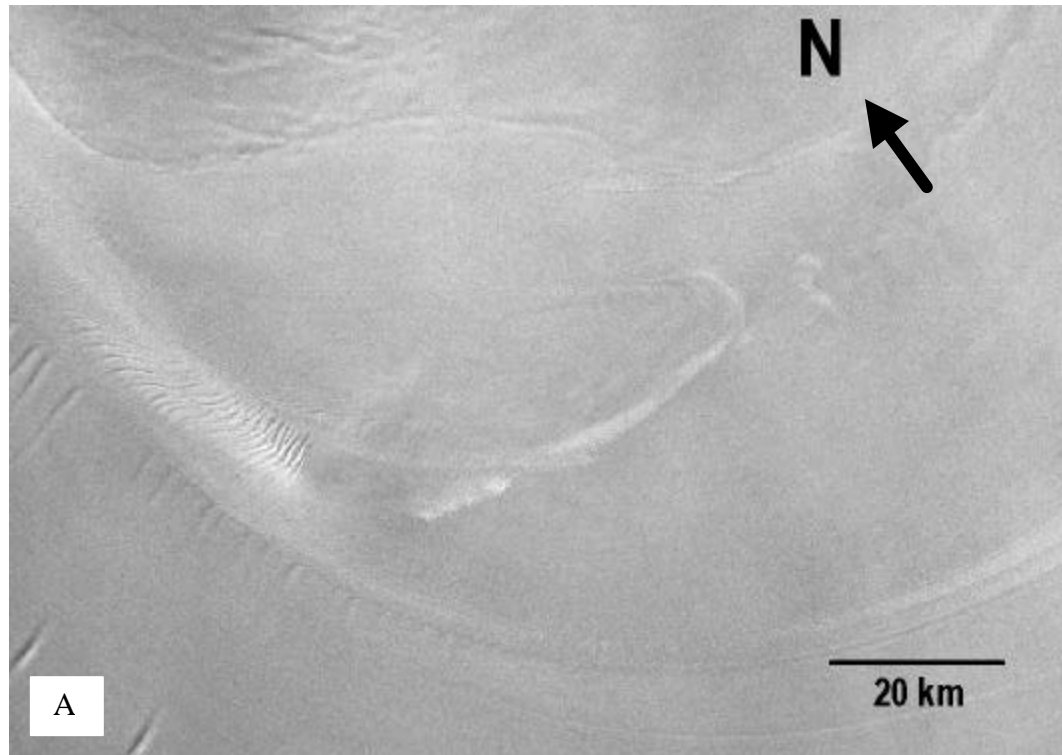
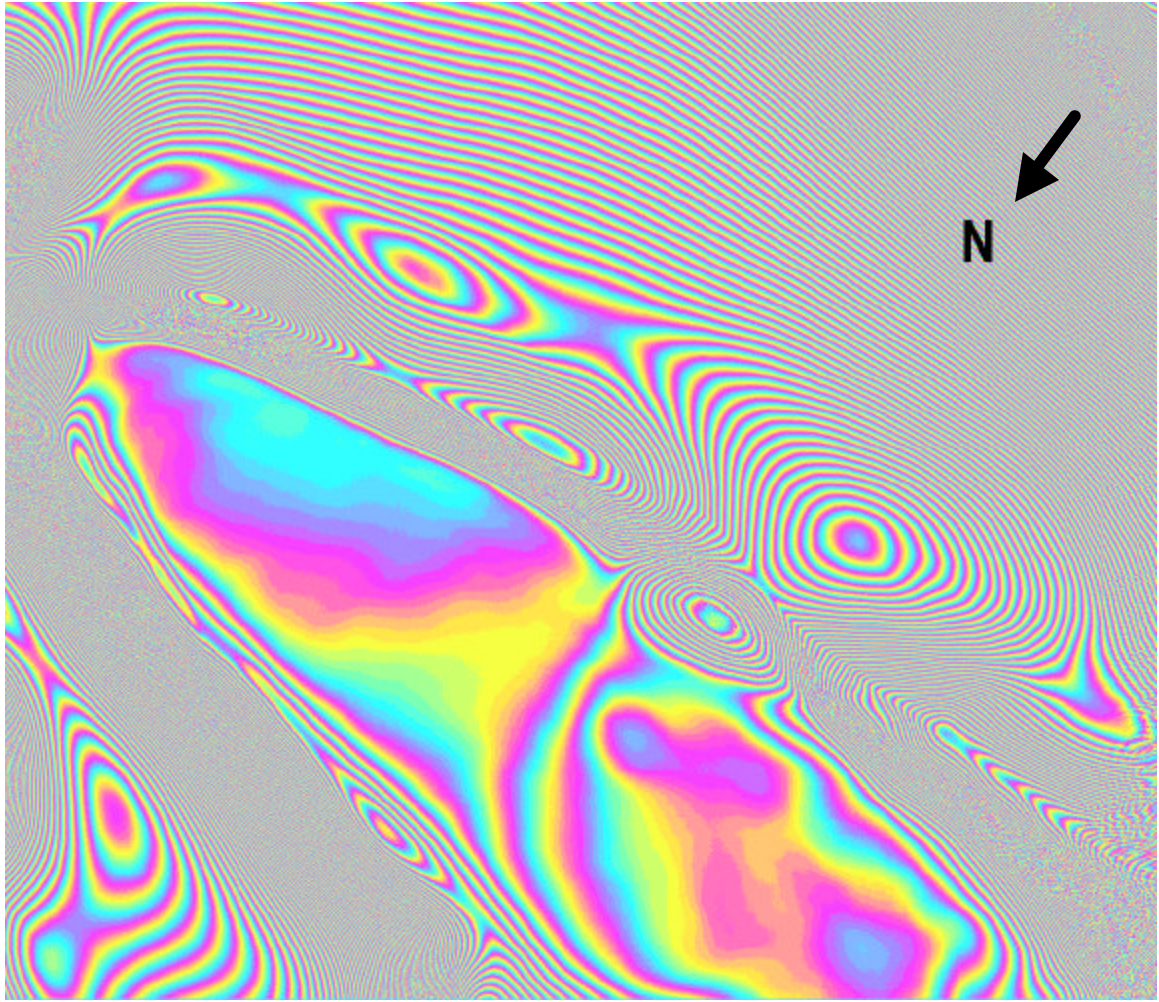


Figure 7.11: Ice rise in the SAR image and coherence image



10 km

Figure 7.12 Interferometric fringes around the ice rise

7.2.4 RAMP glacier and Blackwall Ice Stream

Recovery glacier has two tributaries: RAMP Glacier and Blackwall Ice Stream as shown in Figure 7.13. The RAMP Glacier starts at about 12°43'W/83°33'S and flows about 300 kms north, then merges with the Recovery glacier at the mid point of Recovery glacier. The glacier has a uniform width, and the shear margins are clearly visible on the SAR mosaic. The Blackwall Ice Stream is similar in shape and length to the RAMP glacier. The Blackwall Ice Stream merges into the Recovery Glacier at the point just before the grounding zone. The Blackwall Ice Stream shear margins are visible from the SAR image, but the contrast is not as high as that of the RAMP Glacier. Table 7.1 presents a comparison between the physical properties of these twin glaciers.

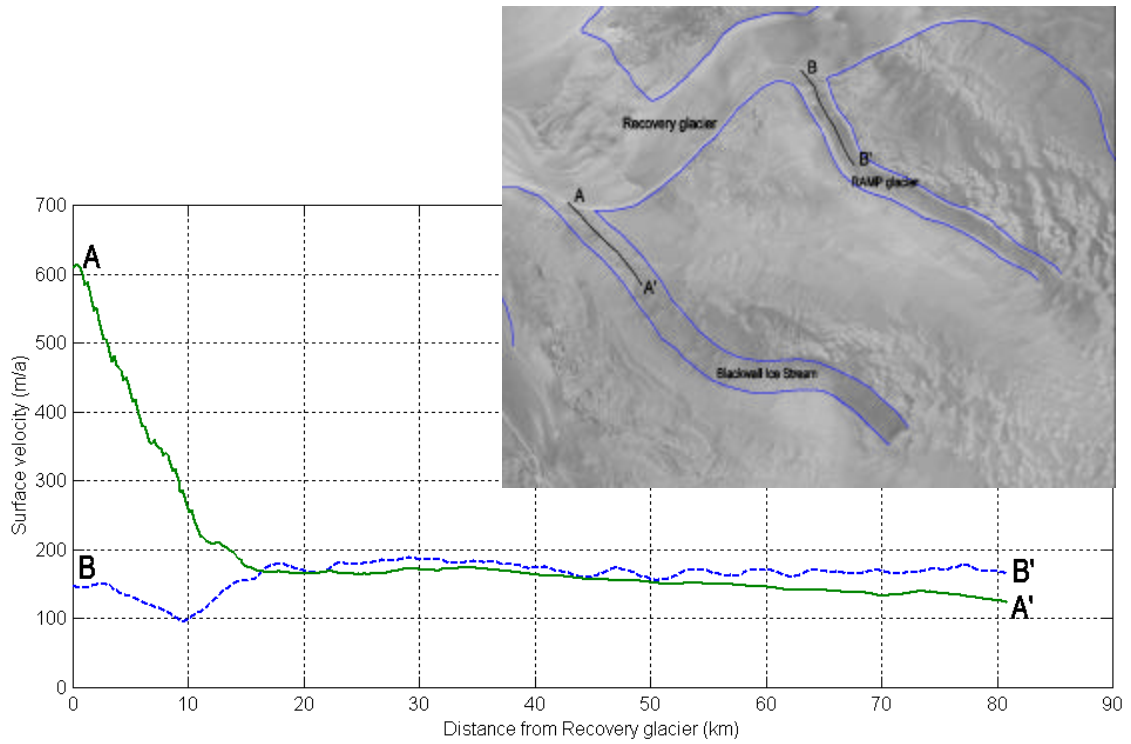
	RAMP	Blackwall
Shape	Pipe shape	Pipe shape
Length	300 km	340 km
Width	15-20 km	20-25 km
Velocity	150-180 m/year	150-200 m/year
Out flux	1.83 km ³ /a	1.96 km ³ /a

Table 7.1: Comparison between the RAMP Glacier and the Blackwall Ice Stream.

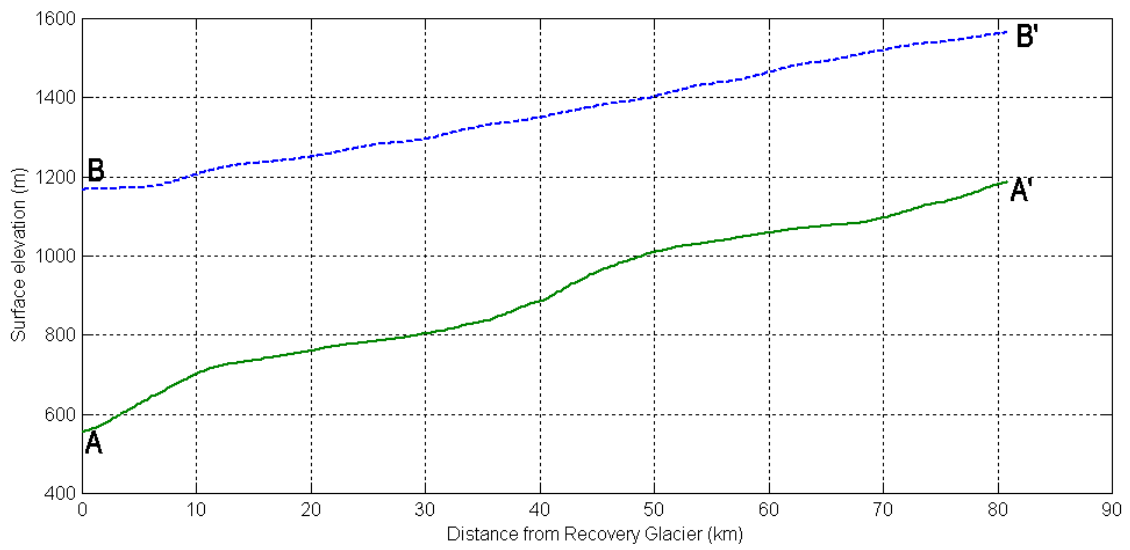
Longitudinal profiles A-A' and B-B' of the twin glaciers are compared in Figure 7.13. The profiles start from their merging point with Recovery Glacier and continue

along their centerlines. Figure 7.13 shows surface velocity (a) and surface elevation (b) changes along the glaciers. The surface elevation for the RAMP glacier decreases almost linearly down the glacier with a slope of 0.005 when moving toward the Recovery Glacier. Since the surface elevation in this area is interpolated from contour lines (Liu, 1999), detailed variations of surface change are lost. Blackwall Ice Stream has a similar profile shape of surface elevation.

Surface velocities of both glaciers are also similar after the 15-km point in the profiles. However, velocities for both glaciers are quite different before the 15-km point. The profiles suggest that Recovery Glacier is “pulling” the Blackwall Ice Stream and “damming” the RAMP Glacier.



(a) Surface velocity



(b) Surface elevation

Figure 7.13 Longitudinal profiles of the RAMP (B-B') and Blackwell Ice Stream (A-A')

7.3 Mass balance and mass distribution

7.3.1 Data sets

The calculation of mass balance requires surface velocity, ice thickness, and accumulation rate data. Surface velocities for the East Antarctic Ice Streams are generated in this research. The random error is 15 m/year and the systemic error is 20 m/year. Ice thickness data for the East Antarctic are from the BEDMAP database of the British Antarctic Survey (Lythe and others, 2000). The ice thickness on the Filchner Ice Shelf is derived from the surface elevation using the hydrostatic conversion model (Lythe and others, 2000). The error is better than 60 m. For areas of Recovery Glacier, the ice thickness is determined from model-based interpolation (Lythe and others, 2000). We are not confident in the ice thickness data from this area. Accumulation rate data are from Vaughan and others (1999). The uncertainty of accumulation rate is around $\pm 5\%$.

7.3.2 Mass balance calculation

Mass balance calculations estimate ice thinning or thickening rate for a region that is bounded by an input gate, output gate, and flow lines. The ice sheet thickening rate $\partial H/\partial t$ can be expressed as

$$\frac{\partial H}{\partial t} = \frac{Q_e - Q_o + S \dot{A} + S \dot{B}}{S} \quad (7.1)$$

where Q_e is the volume of ice entering into the region through an input gate in a unit time period, Q_o is the volume of ice outgoing from the region through the output gate in a unit

time period, \dot{A} is the accumulation rate, \dot{B} is the basal melting/freezing rate, and S is the area of the region.

Gate flux Q (represented by Q_e or Q_o) is calculated from n evenly spaced points. Each point has velocity V_i , and ice thickness H_i . Then

$$Q_e, Q_o = \sum_{i=1}^n V_i H_i W_i \quad (7.2)$$

where W_i is the distance between two neighboring points. Velocity V_i is assumed to be depth averaged velocity and is the normal component of the velocity to the gate.

The random error in gate flux Q is expressed as (Thomas and Bentley, 1978)

$$\Delta Q_e, \Delta Q_o = \pm \left\{ \sum_{i=1}^n \left[(W_i V_i |\Delta H_i|)^2 + (W_i H_i |\Delta V_i|)^2 \right] + (H_1 V_1 \Delta W)^2 + (H_n V_n \Delta W)^2 \right\}^{\frac{1}{2}} \quad (7.3)$$

There is also a systematic error in calculating net flux as (Thomas, 1978)

$$\Delta Q_s = \left\{ \left[\Delta V_s (\overline{H_e W_e} - \overline{H_o W_o}) \right]^2 + \left[\Delta H_s (\overline{V_e W_e} - \overline{V_o W_o}) \right]^2 \right\}^{\frac{1}{2}} \quad (7.4)$$

where ΔV_i and ΔH_i are random errors in velocity and ice thickness, ΔW is the position error for a gate, ΔV_s and ΔH_s are systematic errors for velocity and ice thickness, $\overline{H_e}$ and $\overline{H_o}$ are averaged ice thicknesses across and along the input output gates, $\overline{V_e}$ and $\overline{V_o}$ are averaged velocities across the input and output gates.

The total error for thickening rate is

$$\Delta = \pm \frac{1}{S} \left\{ \Delta Q_e^2 + \Delta Q_o^2 + \Delta Q_s^2 + \left(S \Delta \dot{A} \right)^2 + \left(S \Delta \dot{B} \right)^2 \right\}^{\frac{1}{2}} \quad (7.5)$$

To study the mass balance of the East Antarctic Ice Streams, four regions are defined as shown in Figure 7.14. Regions 1, 2, and 3 are for Bailey Glacier, Slessor Glacier, and Recovery Glacier respectively, and Region 4 is for the Filchner Ice Shelf. The total area of the four regions is considered as Region 5 for mass balance of the East Antarctic Ice Streams. Each region has one output gate and one or more input gates, which are marked by a number in the figure. The locations of the gates are selected, depending on the availability of velocity data and the velocity data quality.

In this study, 15 m/year is used for a random error, 20 m/year is used for the systematic error. Random error in ice thickness is 20 m. Ice thickness systematic errors vary depending on different regions (Lythe and others, 2000). They are 60, 100, 300, 50, and 150 meters for Region 1 to 5 respectively. The accumulation rate error is 5% (Vaughan and others, 1999). We choose a maximum position error for a gate as 800 m (4 pixels in the SAR mosaic of 200 m resolution). Using these errors and measured parameters, the gate fluxes are calculated in Table 7.2

Gate #	Flux (km ³ /a)	Error (km ³ /a)
1	4.30	±0.04
2	21.66	±0.1
3	14.09	±0.12
4	1.83	±0.18
5	1.96	±0.17
6	3.85	±0.20
7	0.24	±0.28
8	23.74	±0.38
9	2.77	±0.39
10	31.34	±0.36
11	10.80	±0.28
12	77.47	±0.34

Table 7.2 Gate flux of the 12 gates

Region	Area (km ²)	Input (km ³ /a)	Accumulation (km ³ /a)	Output (km ³ /a)	Thickening rate (m/a)
1	4414.65	4.3±0.04	0.64±0.03	3.85±0.20	0.248±0.06
2	18897.26	21.66±0.1	2.79±0.14	23.74±0.38	0.037±0.139
3	35602.04	17.88±0.27	5.16±0.26	31.34±0.36	-0.233±0.215
4	22428.75	72.74±0.79	4.69±0.23	77.47±0.34	-0.002±0.126
5	81342.70	57.66±0.63	13.27±0.66	77.47±0.34	-0.080±0.105

Table 7.3: Thickening rate of the east Antarctic Ice Streams

For the inland ice streams, we assume $\dot{B}=0$. So, based on Equation 7.1, ice-thickening rates are calculated as shown in Table 7.3 and Figure 7.14. The results indicate that the Bailey Glacier (Region 1) is thickening at a rate of 0.25 ± 0.06 m/year. The Recovery Glacier (Region 3) is thinning at a rate of -0.233 ± 0.215 . Slessor Glacier is in mass balance. $\frac{\partial H}{\partial t} - \dot{B}$ is insignificantly different from zero for the Filchner Ice Shelf. Mass balance for the entire region is also in balance (neglecting basal melting/freezing on the ice shelf).

Gray and others (2001) have also calculated the mass balance on the Filchner Ice Shelf in an area similar to Region 4. Their area does not include ice from Bailey Glacier. They conclude that the Filchner Ice Shelf is in balance, which agrees with our findings.

7.3.3 Mass distribution

Ice flux for each tributary of the East Antarctic Ice Streams was calculated. Figure 7.15 shows the flux distribution. Input gates for Region 4 in Figure 7.14 are used for the tributaries feeding into the Filchner Ice Shelf. Fluxes for the RAMP Glacier and Blackwall Ice Streams are from gates 4 and 5 in Figure 7.14. Since they feed into Recovery Glacier, Recovery Glacier flux includes these two glaciers. Upstream the Slessor Glacier is partitioned into three channels, separated by two stationary islands marked as C and D in Figure 7.1. The fluxes for the three channels are respectively SL_1, SL_2, and SL_3 in Figure 7.15. SL_2 is between islands C and D, SL_3 is between D and Shackleton Range. SL_1 is the channel north of island C.

From Figure 7.15, we see that Recovery Glacier and Slessor Glacier are the two major sources of ice flux into the Filchner Ice Shelf with $31.3 \text{ km}^3/\text{a}$ and $23.7 \text{ km}^3/\text{a}$, respectively. They account for about 43% and 33% of all the ice feeding into the Filchner Ice Shelf. The flux for Recovery Glacier is different from Gray and others (2001) because the flux for Recovery Glacier here includes ice from Shackleton Fall that originates from the Recovery Glacier. Taking this factor into consideration, our calculation of flux distribution is consistent with that of Gray and others (2001).

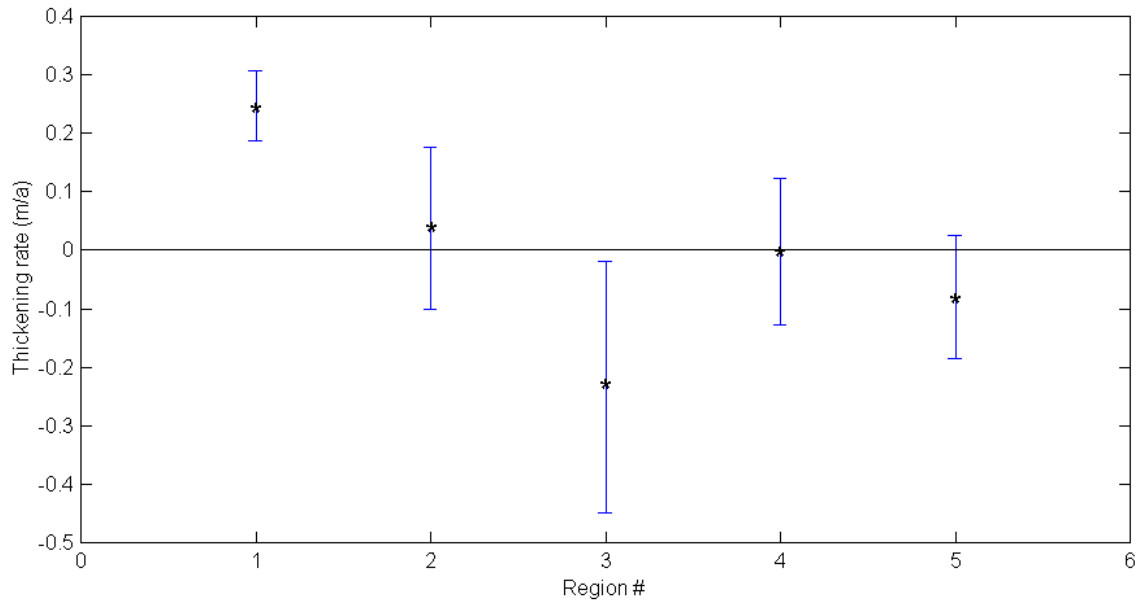
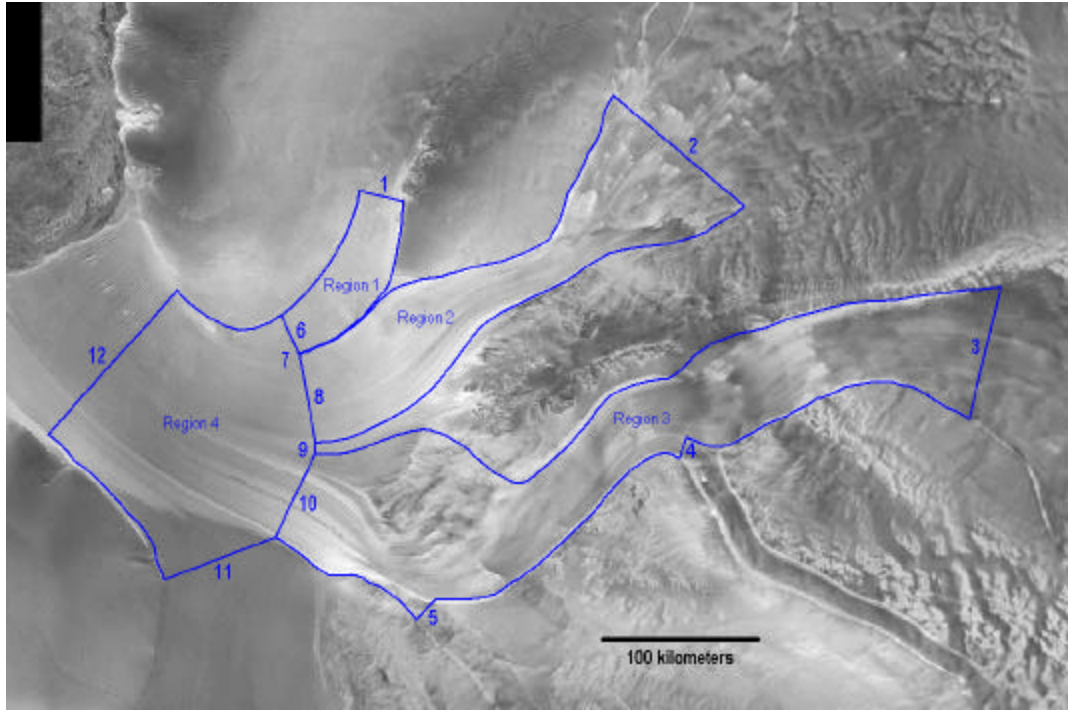


Figure 7.14: Locations of regions and gates for mass balance calculation of the East Antarctic Ice Stream (top) and thickening rate for the regions (bottom)

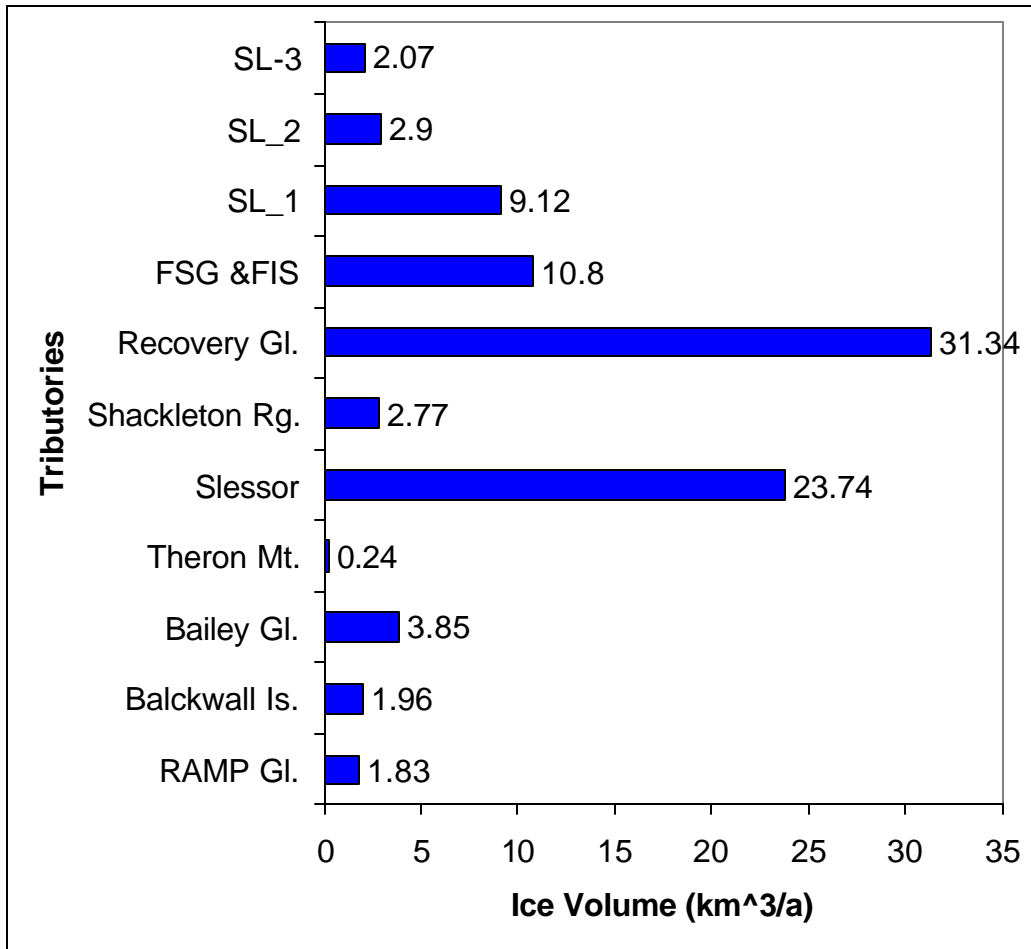


Figure 7.15: Mass distribution of the East Antarctic Ice Streams

CHAPTER 8

CONCLUSIONS

This research has addressed three issues related to the study of the Antarctic Ice Streams. First, we explored technical methods and algorithms suitable for two-dimensional surface velocity estimation from RADARSAT-1 interferometry data over the East Antarctic Ice Streams. Second, we produced the most complete two-dimensional surface velocity map and coherence map for the East Antarctic Ice Streams. Third, we studied the East Antarctic Ice Stream ice dynamics and mass balance.

The first two issues were discussed in Chapters 4, 5, and 6 in which newly developed or extended methods are used to overcome the limitations of interferometry and speckle matching associated with RADARSAT-1 imaging of the ice sheet to generate two-dimensional surface velocity from one direction InSAR pairs. To improve interferometric coherence over areas with large motion variations, such as fast moving glaciers, Delaunay triangulation based co-registration is used to reduce co-registration errors. The improvement of the coherence increases the accuracy of phase and the coverage of usable phase for areas such as fast moving glaciers. For disconnected phase islands in the same frame, phase reconciliation incorporates individual islands into a single coverage with the same reference. This makes the phase for the entire frame

computable from only one constant to be solved in the velocity calibration. Velocity calibration converts the relative phase from interferometry and azimuth offset from speckle matching into absolute velocity. Several models, such as calibration using flow directions and velocity strip adjustment, are developed. Tools are also implemented for data processing. After processing five swaths of RADARSAT-1 InSAR data, a two-dimensional surface velocity map with 200 m resolution is produced.

The third issue is carefully studied in Chapter 7. Based on the surface velocity map, coherence map, as well as other data, we have investigated ice flow dynamics in several ways. Shear margins for the East Antarctic Ice Streams are identified. Grounding lines are updated. A new ice rise is discovered. Mass balance and mass distribution are also calculated.

From this research, we conclude that RADARSAT-1 interferometric data over the East Antarctic area are sufficient to derive two-dimensional surface velocity without the requirement of multiple look directions. Integrated techniques of interferometry and speckle matching are an effective means for calculating two-dimensional surface velocity from one InSAR pair. Limitations and drawbacks of the interferometry technique and speckle matching technique are reduced or eliminated with the use of the newly developed or extended methods. Taking advantage of the strengths of both techniques, we are able to produce high resolution and accurate two-dimensional surface velocities over the East Antarctic Ice streams wherever InSAR data are available.

The initial contribution of this research to the methodological literature includes Delaunay triangulation based co-registration, phase reconciliation, two-dimensional surface velocity calibration using flow directions as well as velocity points, and strip

adjustment of velocity. The newly developed and extended methods and techniques collectively constitute a comprehensive means for handling technical issues in derivation of two-dimensional velocity information of the East Antarctic Ice Streams from RADARSAT-1 interferometric data.

The major substantive contributions of this research are the high resolution, accurate two-dimensional surface velocity and coherence maps of the East Antarctic Ice Streams, and the first comprehensive analysis of flow dynamics and mass balance of the East Antarctic Ice Streams. The surface velocity map covers most parts of Bailey Glacier, Slessor Glacier, Recover Glacier, Filchner Ice Shelf, and some parts of the RAMP Glacier and Blackwall Ice Stream. The velocity uncertainty is better than 15 m/year. The velocity vector directions are consistent with flow stripes observed from the SAR imagery. The angle difference is within 5° on the glaciers and the Filchner Ice Shelf. This alone confirms that there have been no significant dynamic changes in the East Antarctic Ice Streams during the past several hundred years. The velocities are also consistent with the velocities derived from other sources such as DISP of 1963 and SAR of 1997 using feature tracking over a 34-year period (Kim, 1999). The coherence map reveals rich information about geophysical properties of ice streams. Based on the coherence map, we updated the grounding lines around the Slessor Glacier and Bailey Glacier. We also discover a new small ice rise on the East Side of the Filchner Ice Shelf. The ice rise is “damming” Bailey Glacier. This is probably a reason why Bailey Glacier is thickening. From the coherence map, as well as other data, we also identify the shear margins of the East Antarctic Ice Streams. The upstream flow of the Slessor Glacier is complex due to convergence and divergence of ice flow around several islands of slow ice. The

comparison of the margin map with the BEDMAP subglacial topography strongly suggests that the bottom topography control the position of these ice streams. Mass balance calculations indicate that the ice stream and Filchner Ice Shelf system is not significantly thinning or thickening. There is evidence to suggest that at least one of the individual ice streams (Bailey glacier) is 0.25 ± 0.06 m per year. Ice stream surfaces are generally convex and Slessor Glacier and Bailey Ice Stream driving stresses are large compared to the concave shaped West Antarctic Ice Streams. The surface topography of Recovery Glacier varies the most from an equilibrium profile and stretches of the Recovery Glacier have low driving stress, suggestive of flow on a lubricated bed. The convexity of the surface profiles, high driving stress, evidence of streaming flow and the shape of the glacier bed suggest that a change in ice stream dynamics could potentially result in an imbalanced discharge of large amounts of ice into the sea.

REFERENCES

- Bamler, R., and D. Just. 1993. "Phase Statistics and Decorrelation in SAR Interferograms," Proceedings of IGARSS'93, Tokyo, Japan, pp. 980-984.
- Bamler, R., 1999. "Interferometric Stereo Radargrammetry: Absolute Height Determination from ERS-ENVISAT Interferograms", Proc. IGARSS '99, Hamburg.
- Barber, C.B., Dobkin, D.P., and Huhdanpaa, H.T., 1996, "The Quickhull algorithm for convex hulls," ACM Trans. on Mathematical Software, Dec 1996
- Bentley, Charles R., 1987, Antarctic Ice Streams: A Review, Journal of Geophysical Research, Vol. 92, No. B9, pp8843-8858
- Bindschadler, R.A. ed. 1991. West Antarctic Ice Sheet Initiative, Volume II (NASA Conference Publication 3115).
- Casassa, G., K.C. Jezek, J. Turner and I. Whillans, 1991. Relict flow stripes on the Ross Ice Shelf. *Annals of Glaciology*, 15, 132-138.
- Casassa, G., H.H. Brecher, 1993 Relief and Decay of Flow Strips on Byrd Glacier, Antarctica, *Annals of Glaciology*, 17m
- Curlander, J. C., R. N. McDonough, 1991 Synthetic Aperture Radar System and Signal Processing, New York, Wiley,
- Drewry, D.J., S.R. Jordan, E. Jankowski, 1982, Measured properties of the Antarctic Ice Sheet: surface configuration, ice thickness, volume and bedrock characteristics, *Annals of Glaciology*, 3: 83-91
- Echelmeyer, K. A., W. D. Harrison, C. Larsen and J.E. Mitchell, 1994. The Role of the Margins in the Dynamics of an Active Ice Stream, *Journal of Glaciology*, Vol. 40, No. 136, 1994
- Fahnestock, M., Bindschadler, R. Kwok, and K. Jezek, 1993. Greenland Ice Sheet Surface Properties and Ice Dynamics from ERS-1 SAR Imagery. *Science*, vol. 262, p. 1530-1534.

- Fatland, Dennis R., Craig S. Lingle, 1998. Analysis of the 1993-95 bering Glacier (Alaska) Surge using Differential SAR Interferometry”, Journal of Glaciology, Vol. 44, No. 148,
- Forster, R.R. K.C. Jezek, H.G. Sohn, L. Gray and K. Matter, 1998. Analysis of Glacier Flow Dynamics from Preliminary Radarsat INSAR Data of the Antarctic Mapping Mission. Proceedings of IGARSS '98. p. 2225-2227.
- Gabriel, A.K., and R.M. Goldstein. 1988. "Crossed Orbit Interferometry : Theory and Experimental Results from SIR-B," International Journal of Remote Sensing, Vol. 9 (5), pp. 857-872.
- Gatelli, Fabio, 1994. Andrea Monti Guarnieri, Francesco Parizzi, Paolo Pasquali, Claudio Prati, Fabio Rocca, “The wavenumber shift in SAR interferometry”, IEEE trans on Geoscience and Remote Sensing, Vol 32, No 4,
- Ghiglia, Dennis C., Mark D. Pritt, 1998. Two-dimensional phase unwrapping: theory, algorithms, and software, Wiley,
- Goldstein, R.M., H.A. Zebker, and C.L. Werner. 1988. "Satellite Radar Interferometry: Two-Dimensional Phase Unwrapping," Radio Science, Vol. 23(4), pp. 713-720.
- Goldstein, H Engelhardt, B. Kamb, and R. Frolich, 1993. Satellite radar interferometry for monitoring ice sheet motion: application to an Antarctic ice stream. Science, vol 262, p. 1525-1530.
- Gray, L.A., and P.J. Farris-Manning. 1993. "Repeat-Pass Interferometry with Airborne Synthetic Aperture Radar,(cbs.)," IEEE Transactions on Geoscience and Remote Sensing, Vol. 31(1), pp. 180-191.
- Gray. L., K. Mattar, P. Vachon, R. Bindschadler, K Jezek, R. Forster, and J. Crawford, 1998. INSAR Results from the Radarsat Antarctic Mapping Mission data: estimation of glacier motion using a simple registration procedure. Proceedings of IGARSS '98.
- Gray, A.L., N. Short, K.E. Mattar and K.C.Jezek, 2001. Velocities and Ice Flux of the Filchner Ice Shelf and its Tributaries determined from Speckle Tracking Interferometry, accepted for publication by the Can. J of Remote Sensing.
- Hagberg Jan O., Lars M. H. Ulander, Jan Askne, 1995. “Repeat-pass SAR Interferometry Over Forested Terrain”, IEEE trans on Geoscience and Remote Sensing, Vol 33, No 2,
- Herzfeld, Ute, Craig S. Lingle and Li-Her Lee, 1994, Recent advance of the grounding line of the Lambert Glacier, Antarctic, deduced from satellite-radar altimetry, Annals of Glaciology 20,

Hoen, E. Weber, Howard A. Zebker, 2001. "Penetration Depths Inferred from Interferometric Volume Decorrelation Observed on the Greenland Ice Sheet", IEEE transaction on Geoscience and Remote Sensing,

Hughes, T., 1975. The west Antarctic ice sheet: instability, disintegration, and initiation of ice ages, *Rev. Geophys. Space Phys.*, 13(4), 502-526.

IPCC, 1996. *Climate Change 1995, The Science of Climate Change*. J.T. Houghton, L.Filho, B. Callander, N. Harris, A. Kattenberg and K. Maskell eds. Cambridge Univ. Press, 572p.

Jezeq, K. C., H. G. Sohn, K. F. Noltmeyer, 1998. "The RADARSAT Antarctic Mapping Project", *Proceeding of IGRSS*, Seattle,

Jezeq, Kenneth C., 1999a, *Glaciological Properties of the Antarctic Ice Sheet from RADARSAT-1 Synthetic Aperture RADAR Imagery*, *Annals of Glaciology* 29, pp286-290

Jezeq, Kenneth, 1999b, *RADARSAT Antarctic Mapping Project: Antarctic Imaging Campaign 2*, NASA proposal

Jezeq, K., Liu, H., Z. Zhao, B. Li, 1999c "Improving Antarctic digital elevation model by radar remote sensing data and GIS techniques," *Polar Geography*, 1999, 23, No. 3, pp. 185-200

Joughin, Ian, 1995. "Estimation of Ice-Sheet Topography and Motion Using Interferometric Synthetic Aperture Radar", PhD. Thesis, University of Washington,

Joughin, I., R. Kwok, and M. Fahnestock, 1996a. Estimation of ice-sheet motion using satellite radar interferometry: method and error analysis with application to Humboldt Glacier, Greenland. *J. of Glac.* Vol 42. No. 142, p. 564-575.

Joughin, I., D. Winebrenner, M. Fahnestock, R. Kwok, and, W. Krabill, 1996b, "Measurement of ice-sheet topography using satellite radar interferometry," *J. Glaciology*, vol. 42, no. 140,

Joughin, I., R. Kwok, and M.A. Fahnestock, 1998. Interferometric estimation of three-dimensional ice-flow using ascending and descending passes. *IEEE Trans. Geosci and Rem. Sens.*, vol 36, no. 1, p. 25-37.

Joughin, I., L. Gray, R. Bindschadler, S. Price, D. Morse, C. Hulba, K. Mattar, and C. Werner, 1999, *Tributaries of West Antarctic Ice Streams Revealed by Radarsat Interferometer*. *Science*, Vol, 286, p. 283-286.

Kao, Thomas, David M. Mount, Alan Saalfeld, 1991. "Dynamic Maintenance of Delaunay Triangulations", Technical report UMIAC-TR-91-5, University of Maryland,

- Kim, K., 1999. Application of time series satellite data to earth science problems, Master's Thesis, The Ohio State University, 69pp,
- Kwok, R., and M. Fahnestock, 1996. Ice sheet motion and topography from radar interferometry. *IEEE. Trans. Geosci. Rem Sens.*, vol 34, no. 1, 189-200.
- Lee, Hoonyol, Jian Guo Liu, 2000. "Topographic Phase Corrected Coherence estimation Using Multi-pass Differential SAR Interferometry: Differential Coherence", IGRSS 2000, Hawaii, July
- Li, F.K., and R.M. Goldstein. 1990. "Studies of Multibaseline Spaceborne Interferometric Synthetic Aperture Radars," *IEEE Transactions on Geoscience and Remote Sensing*, Vol. 28(1), pp. 88-97.
- Li, B., K. Jezek, L. Gray, and K. Mattar, 1998. Mass balance of Filchner Ice Shelf. *EOS, Transactions AGU*, vol. 79, no. 45, p. F327
- Liu, H., K. Jezek and B. Li (1999). "Development of Antarctic digital elevation model by integrating cartographic and remotely sensed data: a GIS-based approach," *Journal of Geophysical Research*, Vol. 104, No. B10, p23,199-23,213.
- Lythe, Matthew B., David G. Vaughan and BEDMAP Consortium, 2000, BEDMAP: a new ice thickness and subglacier topographic model of Antarctica, in press
- Mercer, J. 1978. West Antarctic ice sheet and CO₂ greenhouse effect: a threat to disaster, *Nature*, 271(5643), 321-325.
- Michel, Remi, Eric Rignot, 1999. "Flow of Glacier Moreno, Argentina, from repeat-pass Shuttle Imaging Radar images", *Journal of Glaciology*, Vol. 45, No. 149,
- Mikhail, Edward M, Friedrich E. Ackermann, 1976. *Observations and least squares*, New York ,
- Olmsted, C., 1993, *Alaska SAR Facility Scientific SAR User's Guide*, University of Alaska, Fairbanks, technical report ASF-SD-003, July
- Paterson, W.S.B., 1994. *The Physics of Glaciers*. Third Edition, Pergamon Press, Tarry Town, N.Y., 480 p.
- Padman, L., D. MacAyeal, and Eric Rignot, 1999: Analysis of Sub-Ice-Shelf Tides in the Weddell Sea Using SAR Interferometry, Filchner-Ronne Ice Shelf Program (FRISP) Report No.13, pp. 60-65, Alfred-Wegener Institute, Bremerhaven, Germany.

- Reeh, N., S.N. Madsen, and J.J. Mohr, 1999. "Combining SAR Interferometry and the Equation of Continuity to Estimate the Three-dimensional Glacier Surface-velocity Vector", *Journal of Glaciology*, Vol. 45, No.151, pp.533-538.
- Rignot, Eric, Jakob J. van Zyl, 1993. Change Detection Techniques for ERS-1 SAR Data, *IEEE trans on Geoscience and Remote Sensing*, Vol 31, No 4,
- Rignot, E., K. C. Jezek, and H. G. Sohn, 1995, "Ice flow dynamics of the Greenland ice sheet from SAR interferometry," *Geophys. Res. Lett.*, vol. 22, no. 5, pp. 575-578,
- Rignot, E., 1996. Tidal Motion, ice velocity, and melt rate of Petermann Gletscher, Greenland, measured from radar interferometry. *J. Glac.* Vol 42, no. 142, p. 476-485.
- Rignot, E., L. Padman, D. R. MacAyeal, and M. Schmeltz, 2000: Observation of ocean tides below the Filchner and Ronne Ice Shelves, Antarctica, using synthetic aperture radar: comparison with tide model predictions, *J. Geophys. Res.*, 105, 19,615-19,630.
- Robertson, R., L. Padman and G.D. Egbert. 1998. "Tides in the Weddell Sea", in *Ocean, Ice, and Atmosphere: Interactions at the Antarctic Continental Margin*, Antarctic Research Series, Vol.75, pp.341-369.
- Rodriguez, E., and J.M. Martin. 1992. "Theory and Design of Interferometric Synthetic Aperture Radars,"(abe.), *IEE Proceedings-F Vol. 139(2)*, pp. 147-159.
- Roth, A., T. Hugel, M. Matschke and G. Schreier, 1993. Experiences with ERS-1 SAR compositional accuracy. *IEEE Trans. Geosci. Rem. Sens.*, International Geoscience and Remote Sensing Symposium, August 1993. Tokyo Japan, Proc. 3, 1450-1452.
- Rott, H., P. Skvarca, and T. Nagler, 1996. Rapid collapse of the Northern Larsen Ice Shelf, Antarctica, *Science*, 271, 788-792.
- Saalfeld, Alan, 1985. A Fast Rubber-Sheeting Transformation Using Simplicial Coordinates, *The American Cartographer*, Vol. 12, No. 2, pp. 169-173
- Scambos, T.A., and R. Bindschadler, 1993. Complex ice stream flow revealed by sequential satellite imagery. *Annals of Glac.*, 17. P. 177-182.
- Scambos, T.A., M. J. Dutkiewicz, J. C. Wilson, and R. Bindschadler, 1992. Application of image cross-correlation to the measurement of glacier velocity using satellite image data. *Remote Sens. Environ.* 42, 177-186.
- Schmidt J., K-H. Thiel and H. Sandhäger. 1999. "Large Scale Interferometry over Filchner-Ronne Ice Shelf", *FRINGE Meeting 1999*, Liège.
- Sievers, J., A. Grindel and W. Meier, 1989. Digital satellite image mapping of Antarctica. *Polarforschung*, 59, 23-33.

- Small, David L., Charles L. Werner, Daniel R. Nuesch, 1993. "Registration of ERS-1 SLC products for SAR Interferometry", Proceeding of Fourth GEOSAR Workshop, Loipersdorf, Austria, May 26-28, pp.63-66
- Thomas, R.H., and C. Bentley, 1978. The equilibrium state of the eastern half of the Ross Ice Shelf. *Journal of Glaciology*, vol 20, no 84, p. 509-518.
- Van Der Veen, C. J., Whillans, I. M., 1990. Flow Laws for Glacier Ice: Comparison of Numerical Predictions and Field measurements, *Journal of Glaciology*, Vol. 36, No. 124,
- Vaughan, D.G., and M. Jonas, 1996. Measurements of velocity of Filchner-Ronne Ice Shelf. *Filchner-Ronne Ice Shelf Programme (FRISP)*, 10, 111-116.
- Vaughan, Davis G., J. L. Bamber, M. Giovinetto, J. Russell, A. P. Cooper, 1999, Reassessment of net surface mass balance in Antarctica, *Journal of climate*, Vol. 12, April 1999.
- Vexcel Corporation, 1999, *Vexcel 3D SAR Processing System User's Manual*
- Vornberger, P. L., I. M. Whillans, 1990. Crevasse Deformation and Examples from Ice Stream B, Antarctica, *Journal of Glaciology*, Vol. 36, No. 122,
- Wivell, Charles E., Daniel R. Steinwand, Glenn G. Kelly, and David J. Meyer, 1992. Evaluation of Terrain Models for the Geocoding and Terrain Correction of Synthetic Aperture Radar (SAR) Images, *IEEE Transaction on Geoscience and Remote Sensing*, Vol. 30, No. 6, November
- Xu, W. and I. G. Cumming. 1996. "A Region-Growing Algorithm for InSAR Phase Unwrapping," *Proceedings of the International Geoscience and Remote Sensing Symposium, IGARSS'96, Lincoln, Nebraska*, pp. 2044-2046.
- Zebker, H.A., and R.M. Goldstein. 1986. "Topographic Mapping from Interferometric Synthetic Aperture Radar Observations,"(abs.), *Journal of Geophysical Research*, Vol. 91(B5), pp. 4993-4999.
- Zebker, H.A., and J. Villasenor. 1992. "Decorrelation in Interferometric Radar Echoes," *IEEE Transactions on Geoscience and Remote Sensing*, Vol. 30, pp. 950-959.
- Zebker, H.A., C.L. Werner, P.A. Rosen, and S. Hensley. 1994. "Accuracy of Topographic Maps Derived from ERS-1 Interferometric Radar," *IEEE Transactions on Geoscience and Remote Sensing*, Vol. 32, pp. 823-836.

李行远